10. Site 1229[1]

Shipboard Scientific Party[2]

BACKGROUND AND OBJECTIVES

Site 1229 was one of three Leg 201 sites selected for drilling on the continental shelf of Peru. These shelf sites were collectively selected to provide records of microbial activities, communities, and geochemical consequences in organic-rich ocean-margin sediments.

The principal objectives at this site were

1. To test by comparison with other sites drilled during this expedition whether microbial communities, microbial activities, and the nature of microbe-environment interactions are different in organic-rich ocean-margin sediments than in open-ocean sediments with less organic matter;
2. To test how the occurrence of sulfate-bearing subsurface brine affects microbial communities, microbial activities, and microbial influence on sediment chemistry in organic-rich, sulfate-depleted, methane-rich sediments; and
3. To provide multiple opportunities for recovering and identifying the sulfate-reducing methanotrophic communities of deeply buried marine sediments.

Site 1229 is located on the Peru shelf in 150.5 m water depth. It is in the immediate vicinity of Leg 112 Site 681. As described in "Principal Results," p. 2, in the "Site 1227" chapter, geochemical studies of Leg 112 sites show that brine is present below the seafloor in the Trujillo and Salaverry Basins (Suess, von Huene, et al., 1988). Site 1229 provides an opportunity to study how the presence of sulfate-bearing brine affects subseafloor life in organic-rich, sulfate-depleted, methane-rich sediments. Consequently, it provides an excellent standard of comparison for Sites 1227 and 1228, which are, respectively, affected by the intrusion of sulfate-free brine into organic-rich, sulfate-depleted sediments

and the intrusion of sulfate-rich brine into sediments with sulfate-bearing interstitial waters.

Shipboard chemical analyses from Leg 112 indicate that the concentrations of methane at Site 681 increase from 10^2 to 10^5 µL/L in the first 40 m of the sediment column and decline from 10^5 to 10^2 µL/L between 73 and 100 meters below seafloor (mbsf) (Shipboard Scientific Party, 1988). In contrast, the concentrations of dissolved sulfate decline to 0 mM over the first ~30 mbsf, remain at or near 0 mM until 75 mbsf, and then increase steadily with greater depths (Shipboard Scientific Party, 1988). This downhole pattern of sulfate concentrations indicates active sulfate reduction at depths above 30 mbsf and below ~75–100 mbsf. The downhole pattern of methane concentrations indicates that methane is created at depths of 60–70 mbsf and diffuses to the overlying and underlying zones of active sulfate reduction, where both sulfate and methane are destroyed.

Chloride concentrations increase steadily to the base of the hole. Ammonium concentrations decline slightly from the sediment/water interface to 12 mbsf, increase from 12 to 80 mbsf, and then begin to decline again. Alkalinity also declines from the sediment/water interface to 12 mbsf, increases to a subsurface maximum at 32 mbsf, and then declines again with depth. Calcium and magnesium concentrations exhibit minimum values at ~30 mbsf and then increase steadily to the base of the hole. The magnesium/calcium ratio exhibits a broad peak from ~0 to 40 mbsf and then steadily declines to the base of the hole (Shipboard Scientific Party, 1988).

These downhole profiles of dissolved chemical concentrations are collectively inferred to result from high levels of biological activity and biologically driven solid-phase alteration throughout the sediment column, coupled with diffusive exchange with the overlying ocean and with a sulfate-bearing brine introduced at depth. Acridine orange direct counts show that prokaryotic cells are present in samples taken from as deep as 80 mbsf at Site 681 (Cragg et al., 1990). Viable prokaryotes were found and potential activity rates were identified in the same samples (Cragg et al., 1990). The subsurface extent of key electron donors (hydrogen, acetate, and formate) and electron acceptors with standard free-energy yields greater than that of sulfate (oxygen, nitrate, manganese oxide, and iron oxides) was not determined for Site 681.

PRINCIPAL RESULTS

An important objective for Site 1229 is to identify and quantify zones of microbial activity based on reactive interstitial water species. Toward this end, we established a highly resolved chemical record throughout the drilled sediment column. Profiles of conservative ions provide evidence of diffusive mixing between seawater diffusing downward from the sediment/water interface and a brine diffusing upward from older sediments. For example, concentrations of dissolved chloride increase linearly from 559 mM at the sediment/water interface to 1208 mM at the base of the drilled sediment column (186 mbsf). Peak concentrations of biologically affected chemical species, such as ammonium (5800 µM) and dissolved inorganic carbon (DIC) (22 mM), indicate that rates of subseafloor microbial activity are much higher at this ocean-margin site than at open-ocean Sites 1225 and 1226. These peak concentrations also suggest that the subseafloor microbial activity at Site 1229 is slightly greater than that at Site 1228 (which lies just sea-

ward of Site 1229) and perhaps is slightly less than that at Site 1227 (which is situated 310 km to the north on the Peru shelf).

As at Site 1228, the concentration profiles of several biologically affected chemical species exhibit a pronounced anomaly just below the seafloor (at 2–3 mbsf). This anomaly at Site 1229 consists of a brief positive excursion in alkalinity, DIC, ammonium, and sulfide, with a co-occurring negative excursion in dissolved sulfate. The same anomaly is also apparent in the ammonium and alkalinity profiles of Site 681 (Shipboard Scientific Party, 1988). As described in **"Principal Results,"** p. 2, in the "Site 1228" chapter, this near-surface interstitial water anomaly indicates that the steady-state diffusion of biologically active chemicals past the upper sediment column was disrupted by late Pleistocene environmental change and has not yet fully recovered. There are least three possible general explanations of this anomaly. It may result from ongoing activity in a microbial "hotspot" at this shallow sediment depth, it may be a chemical relic of past microbial activity (now relaxing back to a diffusional steady state), or it may be a result of the recent establishment of an oxygen minimum at this water depth, causing the extinction of a bioirrigating benthos and a stimulation of sulfate reduction in the uppermost 2 m of sediment.

The most striking biogeochemical feature of this site is the reversal of the biogeochemical zonation at depth. This reversal is immediately apparent in the dissolved sulfate profile. The sulfate concentrations decline from a seawater value of 29 mM at the sediment surface to 0 mM at ~35 mbsf. They remain at 0 mM from 35 to 88 mbsf and then steadily rise from 0 to 38 mM at 186 mbsf. The sulfate that sustains microbial reduction over the uppermost 35 mbsf of the sediment column ultimately diffuses downward from the overlying ocean. The sulfate that sustains microbial reduction below 88 mbsf is inferred to diffuse upward from the underlying brine. Both intervals of sulfate reduction are marked by local maxima in the concentrations of dissolved sulfide, with a broad peak from ~20 to 40 mbsf and a sharper peak at ~90 mbsf.

The sulfate profile is mirrored by the dissolved methane profile. Dissolved methane concentrations are <100 µM from 0 to 20 mbsf, hold steady at a few hundred micromolar from 20 to 35 mbsf, and then rise to values of ~2000 µM (exceeding 1 bar partial pressure) between 65 and 75 mbsf. Methane then steadily declines to <100 µM at 93 mbsf and remains in the range of 100 µM or less to the base of the sampled sediment column. As at Site 1227, the disappearance of almost all methane at the depths of sulfate depletion indicates that most of the methane in this sediment column is ultimately destroyed by anaerobic methanotrophy. As observed at all previously drilled Leg 201 sites, the Site 1229 methane and sulfate profiles indicate that methane can be maintained in subseafloor sediments at background concentrations that are inversely related to the co-occurring dissolved sulfate concentrations.

The dissolved iron and manganese concentration profiles demonstrate that net reduction of iron and manganese oxides occurs in the methanogenic zone. The principal foci of net manganese and iron reduction are at slightly different depths, with iron reduction peaking at 75–90 mbsf and manganese reduction just above and below that interval. The presence of methanogenesis in iron- and manganese-reducing environments may result from a limited availability of mineral-supplied electron acceptors relative to electron donors. In these organic-rich sediments, electron donors may be supplied to the microbial community

faster than mineral dissolution can supply dissolved reducible manganese and iron.

The dissolved barium profile is broadly similar to the methane profile. Dissolved barium concentrations are <2 µM from 0 to 24 mbsf. Concentrations of barium in interstitial water then rapidly rise to 18 µM at 40 mbsf and remain near 19 µM until almost 80 mbsf. They then decline steeply to 2 µM at ~100 mbsf and are <2 µM for the remainder of the drilled sediment column. As at Site 1227, the inverse relationship between sulfate and barium is inferred to be controlled by the solubility product of $BaSO_4$ (barite). Upward diffusion of barium past 35 mbsf and downward diffusion of barium past 90 mbsf is suspected to sustain modern barite formation at, respectively, ~24 and 100 mbsf. Similarly, the shoulders of the barium peak at ~40 and 80 mbsf are inferred to mark the principal depths of current barite dissolution at this site.

Prokaryotic cell counts were done at 10-m intervals throughout the upper sediment column and across both sulfate/methane interfaces. These data show that mean sedimentary cell concentrations are several-fold higher at this ocean-margin site than at the Leg 201 open-ocean sites and may be slightly higher than mean concentrations at nearby Site 1227. The most striking features of the shipboard cell counts are the thousandfold increase in cell concentrations in the lower zone of overlapping sulfate and methane concentrations and the tenfold increase in cell concentrations in the upper zone of overlapping concentrations. The maximum cell concentrations observed in the lower sulfate/methane zone are actually an order of magnitude higher than the concentrations observed at the sediment/water interface. Given the coarse spacing of these samples and their positions relative to the chemically defined sulfate/methane overlap zones, the peak cell concentrations observed in the upper sulfate/methane zone may greatly underestimate the peak concentrations in that zone.

Acetate and formate concentrations exhibit strong local maxima of ~6 µM in both of the sulfate/methane interface zones. These maxima are centered at 37 and 90 mbsf. As with the cell counts, these local maxima are higher than the local maxima exhibited by both acetate (~2 µM) and formate (3 µM) at the sediment/water interface. Throughout most of the remaining record at this site, concentrations of both species were between 1 and 2 µM. As at Site 1227, the concentrations of both species reach their highest values near the base of the drilled sediment column (~15 µM). These results are intriguing because these volatile acids are important substrates for both sulfate reducers and methanogens. Hydrogen is another important electron donor in anaerobic communities. Almost all hydrogen concentrations measured at this site were <0.5 nM, and most were <0.2 nM. These concentrations resemble those observed at open-ocean Site 1225 and ocean-margin Site 1227. As noted in **"Principal Results,"** p. 2, in the "Site 1225" chapter and **"Principal Results,"** p. 2, in the "Site 1227" chapter, these concentrations are much lower than expected from experiments with sulfate-reducing and methanogenic communities of surface sediments. The accurate interpretation of these acetate, formate, and hydrogen concentrations must await postcruise analyses of prokaryotic energetics in subseafloor environments.

The cell concentration data and sulfate and methane gradients demonstrate that the subseafloor prokaryotic population and activity are locally strongly focused at the sulfate/methane overlap zone defined by the upward-diffusing sulfate-bearing brine and the downward-diffusing methane. The dissolved barium profile indicates that microbial activity

in this zone directly influences sediment chemistry by mediating the precipitation and dissolution of barite. In these effects on subsurface biological activities and biogeochemical cycles, this brine-caused sulfate/methane interface mirrors the effects of the overlying "normal" sulfate/methane interface. Postcruise microbiological studies will be required to demonstrate whether or not the microbial community supported by the brine-induced interface is locally unique or the same as that supported by the overlying interface.

The upper sulfate-rich zone at Site 1229 lies entirely within lithostratigraphic Subunit IA, a stratigraphic interval of primarily hemipelagic sediments (0–40 mbsf). The underlying methane-rich zone is largely limited to lithostratigraphic Subunit IB, which is the upper portion of a longer interval (40–138 mbsf) of mixed terrigenous and hemipelagic sediments. The anaerobic oxidation of methane (AOM) zones that separate the upper and lower sulfate-rich zones from the intervening methane-rich zone are associated with brief sedimentary intervals characterized by high grain density, high natural gamma radiation (NGR), high resistivity, and low porosity. These brief low-porosity intervals are unusually rich in terrigenous sediment and are interpreted to have been deposited during the two most recent lowstands of four onlap/offlap cycles that define the 40- to 138-mbsf interval.

In short, as at Site 1228, the upper sulfate-reducing interval at Site 1229 is composed of predominantly hemipelagic sediments, the strongly methanogenic zone is rich in terrigenous sediment relative to the overlying sulfate-reducing zone, and the intervening AOM zone is present just above an interval of low-porosity, high-density lowstand sediments. The lower AOM zone at Site 1229 is present within a similar interval of high-density, low-porosity lowstand sediments. The lithologic association of AOM zones with high-density, low-porosity lowstand sediments at Sites 1229, 1228, and 1227 provides intriguing evidence that, on the Peru shelf, the position of AOM zones is currently pinned within the sediment column by lithologic properties and, by extension, depositional history.

As at Site 1227, stratigraphic patterns of magnetic susceptibility and dissolved manganese, iron, and sulfide concentrations indicate similar control of other microbial processes by depositional history at Site 1229. Magnetic susceptibility is generally much higher in the methanogenic zone and in the lower sulfate-reducing zone than in the overlying sulfate-reducing zone. This circumstance suggests that mineral sources of reducible iron and manganese are more abundant in the terrigenous-dominated sediments of the lower sulfate-reducing zone and the mixed terrigenous and hemipelagic sediments of the methanogenic zone than in the mostly hemipelagic sediments of the upper sulfate-reducing zone. The relatively high magnetic susceptibility of the intervals with more strongly terrigenous sediments is consistent with our finding that dissolved manganese and iron concentrations are generally higher in the lower methanogenic zone and the underlying sulfate-reducing zone than in the upper sulfate-reducing zone. The presence of higher manganese and iron concentrations and lower sulfide concentrations in these relatively high susceptibility intervals in turn provides strong evidence that the current rates and stratigraphic foci of iron reduction, manganese reduction, and sulfide precipitation depend strongly on depositional history.

Experiments on major microbial processes and on enumeration of viable prokaryotes were initiated at selected depths ranging from near the mudline to the bottom of the drilled sediment column. The studied

processes include methane and acetate formation and consumption, sulfate reduction, hydrogen oxidation, and rates of cell growth. The cultivation experiments include selective growth conditions for a wide range of autotrophic and heterotrophic microorganisms ranging from psychrophilic to thermophilic. Detailed microbiological sampling targeted the top of the sediment column and both the upper and lower sulfate/methane overlap zones.

The results from one Davis-Villinger Temperature Probe (DVTP) deployment were combined with temperature data from Site 681 to define a linear gradient of 35.5°C/km for this site. The mean sediment/water interface temperature defined by this gradient is 13.4°C. The temperature defined for the base of the drilled sediment column (193 mbsf) is 20.2°C. Throughout this interval (0–193 mbsf), temperatures are in the low mesophilic range.

Trials were undertaken of four experimental tools at this hole: the pressure coring sampler (PCS), the Davis-Villinger Temperature-Pressure Probe (DVTP-P), the Advanced Hydraulic Piston Corer-Methane (APC-M) tool, and the Fugro percussion corer (FPC).

OPERATIONS

Transit to Site 1229

Sites 1228 and 1229 are 9 nmi apart, so the transit between them only required an hour, and a positioning beacon was deployed at 1330 hr on 6 March 2002 at the coordinates recorded in the Leg 112 *Initial Reports* volume (Shipboard Scientific Party, 1988) and verified by the Ocean Drilling Program (ODP) Drilling Services Department operations report for Leg 112. Coring operations at Site 1229 are detailed in Table **T1**.

Hole 1229A

Our first operation at Site 1229 was deployment of the water sampling temperature probe (WSTP) to collect a bottom-water sample. A short in the electronics prevented the tool from functioning properly, and an in-line capacitor was installed in the tool to prevent similar failures in future deployments. Continuous advanced hydraulic piston coring (APC) through Core 4H (0.0–33.4 mbsf) returned 98% recovery. The signal from a DVTP temperature measurement at this depth appears noisy, but a severe current was rattling the drill pipe and the formation may have been unsuitable to sufficiently seal the tool in the sediment. APC coring continued to 58.9 mbsf (Cores 5H through 7H), where we intended to make another DVTP measurement, but poor recovery in the last two cored intervals above this depth prompted us to delay this effort. Recovery improved on the next two cores (Cores 9H and 10H) (58.9–77.9 mbsf; recovery = 98%), so the DVTP and the DVTP-P were deployed after Cores 9H and 10H, respectively.

As we experienced significant overpull while extracting Cores 9H and 10H, mud pills were pumped after each subsequent core to clean the hole and we began operating in a drill-over mode. High recovery continued through Core 12H (77.9–107.9 mbsf; recovery = 96%), followed by a third DVTP temperature measurement. Cores 13H and 14H (107.9–126.9 mbsf) had somewhat poorer results (average recovery = 75%). The APC-M tool was run continuously from Core 201-1229-2H through

T1. Coring summary, Site 1229, p. 64.

13H. The next three cores (Cores 15H through 17H; 126.9–155.4 mbsf) returned only severely disturbed cores composed of gravel and mud. Based on this result, we aborted a planned deployment of the FPC tool. Because our goal was improved recovery in the lower part of the section compared to Leg 112, we drilled through this interval and attempted two APC barrels (Cores 18H and 19H; 155.4–174.4 mbsf), which returned an interval satisfactory for geochemical and microbiological sampling. The DVTP was deployed after Core 18H at 164.9 mbsf. Core 20M was a deployment of the FPC tool. Cores 21H and 22H took us near our depth objective (194.4 mbsf), but we again experienced poor and disturbed recovery in muddy gravel, so we opted not to perform planned pressure and temperature measurements at this interval and aborted an additional run of the FPC tool as well. Operations at Hole 1229A concluded with logging the entire cored interval using the triple combination (triple combo) tool string.

Perfluorocarbon tracer (PFT) was pumped continuously in all holes at Site 1229 as part of our contamination monitoring protocol. In addition, fluorescent microspheres were deployed on Cores 2H, 3H, 4H, 6H, 9H, 11H, 16H, 17H, 19H, and 22H. Elevated hydrogen sulfide (as high as 50 ppm) was measured with handheld detectors at the rig floor and on the catwalk for the upper part of the cored interval, although hydrogen sulfide was undetectable below 30 mbsf. Nevertheless, alert precautions were maintained throughout coring at this site.

Hole 1229B

Using the dynamic positioning system, we offset 5 m north from Hole 1229A to initiate Hole 1229B. We were restricted in offset distance and direction in order to maintain a reasonably clean signal from the positioning beacon in shallow water. The upper three cores from this hole (Cores 1H through 3H) (0.0–24.4 mbsf; recovery = 102%) were dedicated to shore-based paleoceanography studies, so the cores were not split and the end caps were sealed with tape rather than acetone. Operations at Hole 1229B concluded with a deployment of the FPC tool at 24.4 mbsf. During this deployment the tool was damaged beyond our capacity to repair at sea, so no more deployments were planned.

Holes 1229C and 1229D

After an offset of 20 m west from Hole 1229B, operations began in Hole 1229C with a WSTP deployment, which returned a bottom-water sample. High-resolution sampling of the upper few meters of the sediment column was one of our objectives for this hole, so when Core 201-1229C-1H returned with the upper end of the core liner collapsed and the mudline disturbed, we terminated the hole. A second mudline attempt, offset 5 m west-northwest (Core 201-1229D-1H) (0.0–6.8 mbsf; recovery = 100%), was suitable for our sampling plan and initiated Hole 1229D.

Continuous APC coring continued through Core 201-1229D-9H (to 77.8 mbsf), averaging 81% recovery. The core liner on Core 201-1229D-8H was shattered, resulting in a severely disturbed core. A PCS deployment on Core 201-1229D-10P returned under hydrostatic pressure and contained a mixture of air and methane. An interval between 85 and 90 mbsf that fell at the junction between cored intervals in Hole 1229A was determined by geochemical analysis to be of particular interest, so we asked the drilling crew to optimize our chances of complete recov-

ery of this interval in Hole 1229D. Core 201-1229D-11H was shot from 5 m above the bottom of the hole, thus advancing only 4.5 m to 84.3 mbsf. The subsequent Core 201-1229D-12H bridged the interval of interest, and although the core was partially disturbed, sufficient intact material was recovered to sample for geochemistry and microbiology. Cores 201-1229D-13H through 15H (0.0–115.8 mbsf; recovery = 72%) completed operations in Hole 1229D.

Hole 1229E

For our final penetration at Site 1229, we offset 20 m west of Hole 1229D. Continuous APC coring from Core 1H through 13H (0.0–121.5 mbsf; recovery = 82%) was interrupted only by a short deployment of the DVTP at 83.5 mbsf to augment our thermal profile at this site. Operations at Site 1229 concluded when the bit passed through the rig floor at 0700 hr on 10 March, and we began our transit to Site 1230.

LITHOSTRATIGRAPHY

At Site 1229 we recovered a 194.4-m-thick sequence of mixed diatomaceous and siliciclastic sediments. According to the biostratigraphic and magnetostratigraphic chronostratigraphy established for Site 681, which is located in close proximity of Site 1229 (Shipboard Scientific Party, 1988), updated according to Berggren et al. (1995), the entire sedimentary sequence is late Pliocene to Pleistocene age. In order to establish unit and subunit boundaries, information from Holes 1229A and 1229D is combined to fill gaps caused by poor recovery. Based on lithologic changes detected by means of visual core description, smear slide analysis, color reflectance, X-ray diffraction (XRD), and laboratory measurements of magnetic susceptibility, bulk density, and NGR (see "Physical Properties," p. 20), two lithostratigraphic units were established. Unit I was further subdivided into Subunits IA–IC (Figs. F1, F2).

Description of Lithostratigraphic Units

Unit I

Interval: 201-1229A-1H-1 through 16H-2 and 201-1229D-1H-1
    through 15H-CC
Depth: 0–138.6 mbsf (Hole 1229A) and 0–138.6 mbsf (Hole 1229D)
Age: Pleistocene to Holocene

The lithology of Unit I is characterized by alternations of olive-green well-laminated diatom- and clay-rich silt and clay-and silt-rich diatom ooze. Gray, partly green, more homogeneous silty clay is more abundant in the central part of the unit (Fig. F1). The lower boundary is defined by a transition from green diatom-rich sediments above and clayey silt and sand below. The lithostratigraphic boundary is present below the lowermost layers of diatom-rich sediment in Section 201-1229A-16H-2.

Subunit IA

Interval: 201-1229A-1H-1 through 6H-1 and 201-1229D-1H-1
    through 6H-2
Depth: 0–40.7 mbsf (Hole 1229A) and 0–42.8 mbsf (Hole 1229D)

F1. Lithostratigraphic summary, p. 33.
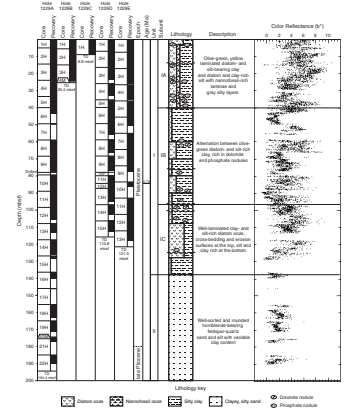
F2. Lithostratigraphy vs. NGR, p. 34.
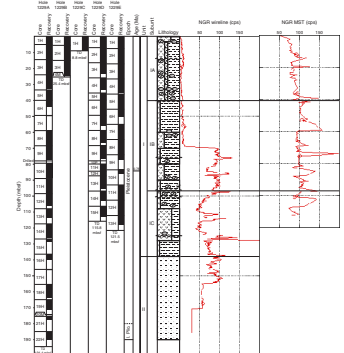
The major lithology of Subunit IA consists of olive-green diatom-and clay-rich silt. Millimeter-scale laminated zones alternate with slightly grayer, almost homogeneous zones with higher clay and silt content. The yellow laminae are enriched in diatoms, some of them showing an almost pure pinnate diatom assemblage. A few calcite-rich nannofossil ooze laminae are present (e.g., XRD Sample 201-1229A-2H-1, 105–106 cm). The uppermost 3 m of Cores 201-1229A-1H and 201-1229D-1H consist of brown, bioturbated, and poorly laminated clay-rich diatom ooze. Bioturbation is poorly developed throughout the rest of the unit. Gray silty clay layers are common sedimentary features. Cross-lamination is present in Sections 201-1229A-5H-4 and 5H-6 and also in interval 201-1229D-1H-2, 90–120 cm (Fig. **F3A**). Two erosional surfaces covered with coarser silty and fine sandy layers are present in Sections 201-1229A-2H-6 and 6H-2. The first authigenic dolomite nodule is present at 3.8 mbsf (XRD Sample 201-1229A-1H-3, 84–85 cm). X-ray diffractions of the uppermost dolostone nodules revealed the presence of a small calcitic component together with dolomite (Sample 201-1229A-2H-1, 56–57 cm) (see **"Mineralogy,"** p. 11), which might be due to nannofossils. Authigenic dolomite becomes more common below 30 mbsf. Disseminated rhombs of dolomite are concentrated around dolomite nodules or in yellow laminae (Fig. **F3B**). The uppermost occurrence of phosphate is at 1.2 mbsf (XRD Sample 201-1229E-1H-1, 122–124 cm). Sections 201-1229E-1H-3 and 1H-4 contain several centimeter-sized phosphate nodules. They are commonly present together with dolomites, but a clear relationship between these two diagenetic minerals could not be established.

The lower boundary of Subunit IA is marked by an erosional surface overlain by phosphatic sand. A gravel zone at the top of Core 201-1229A-6H, which also contains phosphatic nodules, is probably an artifact of the drilling process.

Changes in color reflectance were most obvious in the yellow-blue color reflectance spectrum (chromaticity variable b*; Fig. **F1**). Decreasing b* values coincide with changes in some of the physical properties, such as magnetic susceptibility and bulk density (see **"Physical Properties,"** p. 20). A sharp spike of natural gamma radiation at 40.7 mbsf coincides exactly with the erosional surface at the lower boundary of Subunit IB.

Subunit IB

Interval: 201-1229A-6H-1 through 11H-6
Depth: 40.7–96.9 mbsf

An alternation of gray homogeneous quartz- and feldspar-rich clay layers and olive-green laminated diatom-rich silty clay characterizes the lithology of Subunit IB. Three ~10-m-thick gray siliciclastic layers present in the subunit are spread roughly 25 m apart. Slumping, cross-lamination, sandy graded beds, and lenses of shell debris are common (Fig. **F3D**). Quartz and plagioclase are present in variable amounts throughout the subunit. Dolomite forms pale yellow and gray nodules and semilithified yellow laminae, which are especially abundant in the lower part of the subunit (Fig. **F1**). Dolomite can also be found as white precipitates along millimeter-scale quartz sand–filled dikes that represent fluid escape structures (Section 201-1229A-10H-1; XRD results for Sample 201-1229A-10H-1, 111–114 cm) (Fig. **F3C**).

The upper boundary of Subunit IB is sharp and is present below phosphatic sediments overlying an erosional surface (see Subunit IA).

F3. Site 1229 features, p. 35.

The lithologic change that marks the lower boundary of the subunit was observed only in Section 201-1229A-11H-6 because the recovery in Hole 1229D at this depth was poor. This boundary is defined by a change from gray homogeneous quartz and feldspar-rich clay above to olive-green diatom-rich silty clay below, and it is characterized by a silty layer and bivalve shell debris overlying an erosional surface (Fig. F3D). A similar boundary between "dark gray sandy mud" above and "olive-gray diatomaceous mud" below an erosional surface with black phosphate clasts was observed at Site 681 (Section 112-681A-11H-4; 99.2 mbsf) (Shipboard Scientific Party, 1988). Both the upper and lower boundaries of Subunit IB match sharp peaks in natural gamma radiation (Fig. F2). The color reflectance data for Subunit IB show low average values for the chromaticity variable b*, except for two diatom-rich layers at ~60 to ~70 and ~80 to ~90 mbsf (Fig. F1). These shifts are directly coupled with gray and olive-green observed during visual core description.

Subunit IC

Interval: 201-1229A-11H-6 through 16H-2
Depth: 96.9–138.6 mbsf

The dominant component of Subunit IC is diatom ooze, which is present mixed with variable amounts of sand, silt, and clay. Based on the relative amount of diatom ooze in the sediment, the subunit can be further subdivided into three parts (Fig. F1).

The uppermost part of Subunit IC (between 96.9 and 108.0 mbsf) is characterized by diatom-rich silty clay with cross-bedding, and a few shell debris lenses (Fig. F3D), erosional surfaces overlain by phosphatic hardgrounds (Fig. F3E), and dolomite and phosphate nodules. Fine-grained disseminated dolomite rhombohedra are present in dolomite-cemented semilithified yellow laminae and in the sediments that surround hard dolomite nodules.

The middle part of Subunit IC (between 108.0 and 128.0 mbsf) is a well-laminated clay- and silt-rich diatom ooze. High chromaticity correlates well with the olive-green diatom ooze layers (Fig. F1).

The lowermost part of Subunit IC (between 128.0 and 138.6 mbsf) consists of gray pyrite- and diatom-rich clay. It represents a transitional facies from the sandy siliciclastic sediments of Unit II below to laminated diatom ooze above. The color reflectance variable b* is low in this interval and has similar values as in Unit II. Variable concentrations of scattered dolomite rhombohedra were observed.

The boundary between Units I and II is assumed to exist somewhere between 138.6 and 155.4 mbsf in the poorly recovered interval (Fig. F1). A major lithologic change occurs from diatom-rich silt and clay of Unit I to silty and sandy sediments of Unit II in this interval. Downhole logging NGR and electric resistivity data show increased values in two steps at 128.0 and 138.6 mbsf, where this change occurs (Fig. F2) (see also "Downhole Logging," p. 28). Each step is additionally marked by a sharp spike in electric resistivity. On the basis of these observations, the bottom boundary of Subunit IC was located below the lowermost occurrence of gray diatom-rich sediment, which lies within drilling rubble at 138.6 mbsf (bottom of Section 201-1229A-16H-2).

Unit II

Interval: 201-1229A-16H-2 through 22H-CC

Depth: 138.6–194.4 mbsf
Age: late Pliocene–Pleistocene

Unit II consists of an almost pure siliciclastic packet of Pleistocene sediments. The main lithology is dark gray hornblende-bearing feldspar-quartz sand with variable amounts of clay. Feldspar and quartz grains are well rounded, and their relative amounts vary strongly. The sediments are slightly laminated and show few burrows. In Core 201-1229A-18H, sedimentary structures, such as flat and subangular gray mud clasts, possibly related to synsedimentary slumping, were observed. Authigenic minerals, such as phosphate and dolomite, are present in Unit II but are less abundant compared to Unit I. They are present as disseminated grains in sand layers (see "Mineralogy," p. 11), and nodules were no longer observed.

The upper boundary of Unit II is marked by the onset of diatomaceous ooze layers, which indicates the end of a time period with major siliciclastic input. This transition is poorly documented in Core 201-1229A-16H (see above). However, the transition is well defined in wireline logging data (NGR and electrical resistivity) (see "Downhole Logging," p. 28). Because of both the gray color and the low diatom content, Unit II usually shows low and less variable chromaticity values.

Mineralogy

A total of 21 samples were collected at Site 1229 for XRD analysis. In general, XRD data confirm lithologic observations made during visual core description.

For instance, calcite was found in Sample 201-1229A-2H-1, 105–106 cm, which had been collected from a nannofossil-rich layer in Subunit IA. The presence of quartz and feldspar in all measured samples from Site 1229 suggests a continual supply of terrigenous input, even during the deposition of the biogenic subunits (e.g., Subunit IC). Quartz is especially common in some of the gray layers observed in Subunit IA (Sample 201-1229A-1H-2, 70–71 cm). In all XRD samples from Unit I, feldspar is only a minor mineralogic component, whereas in Unit II it can be more abundant than quartz (Samples 201-1229A-19H-2, 40–41 cm, and 19H-3, 60–61 cm). Pure quartz sand was observed as filling of a fluid escape structure (Sample 201-1229A-10H-1, 111–114 cm). Hornblende was mainly found in the silts and sands of Unit II (Samples 201-1229A-19H-2, 40–41 cm, and 19H-3, 60–61 cm).

The main diagenetic minerals at Site 1229 are dolomite and phosphate. Dolomite is mostly present as pale yellow and gray (3–5 cm thick) hard nodules (Samples 201-1229A-1H-3, 84–85 cm, and 8H-1, 62–64 cm). Only dolomite nodules from Subunit IA contained trace amounts of calcite, possibly due to calcareous nannofossils (Sample 201-1229A-2H-1, 105–106 cm). Disseminated dolomite was detected both by smear slide and XRD analyses (Sample 201-1229A-3H-1, 56–57 cm). It was observed in pale yellow altered zones, which are preferentially present around hard lithified dolomite nodules and within diatom-rich laminae. These scattered dolomite rhombohedra might represent an early stage of the formation and growth of a hard nodule. Dolomite peaks are commonly offset by ~0.2°2θ relative to the standard peak for ordered dolomite, indicating calcium-rich dolomite (Fig. F4) (Samples 201-1229A-1H-3, 84–85 cm; 3H-1, 56–57 cm; 2H-1, 105–106 cm; and 8H-1, 62–64 cm). Phosphate grains found in black sands (Unit II) were identified by XRD as fluorapatite (Sample 201-1229A-21H-1,

F4. Diffractogram of dolomite, p. 38.
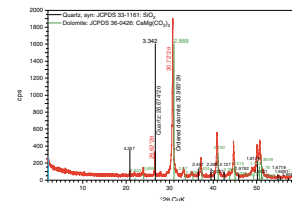
30–31 cm); however, dark D-phosphate nodules and several orange spots of F-phosphate were found (Samples 201-1229A-13H-2, 103–104 cm, and 21H-1, 30–31 cm).

Summary

The 194.4-m-thick late Pliocene to Pleistocene sequence drilled at Site 1229 was divided into two units. Unit I consists of 138 m of mixed diatom-rich hemipelagic and siliciclastic sediment. Unit II is mostly composed of siliciclastic sands. Based on the relative amount of clay and silt in the diatom ooze–dominated sediments of Unit I, three subunits were recognized: Subunit IA consists of olive-green laminated clay-rich diatom and nannofossil ooze and diatom-rich silt and clay. The uppermost 3 m of the subunit consists of poorly laminated brown clay-rich diatom ooze. The lower boundary is marked by an erosional surface overlain by phosphatic sand. In Subunit IB, both diatom ooze and terrigenous silt and clay are present. Cross-lamination, erosional surfaces, and burrowing characterize the diatom-poor layers. Subunit IC consists of a 42-m-thick interval of diatom-rich silty clay and diatom ooze. Planar lamination is present throughout the unit. Cross-lamination and erosional surfaces are present at the top of the subunit.

Unit II consists of homogeneous slightly burrowed hornblende-bearing quartz- and feldspar-rich sand. The most prominent diagenetic feature of this site is the presence of dolomitic and phosphatic minerals, which were observed also at very shallow burial depth. Nodules of dolomite and phosphate are abundant throughout Unit I, and disseminated dolomite is present in Unit II. Disseminated dolomite rhombohedra are abundant in pale yellow zones around hard lithified dolomite nodules and in yellow diatom-rich laminae. Dolomite nodules are often present together with phosphatic nodules.

Variations between diatom-rich and predominantly siliciclastic lithologies observed in the different units and subunits are also identifiable by several physical properties, including color reflectance, magnetic susceptibility, and bulk density. Erosional surfaces observed during visual core description appear to match some of the spikes in natural gamma radiation.

BIOGEOCHEMISTRY

Interstitial Water

Site 1229 is characterized by the presence of a deep brine that introduces sulfate at depth. The interstitial water (IW) sampling scheme for Site 1229 was designed to recover dissolved components at high spatial resolution along the transition from seawater to subsurface brine. Additional sampling was targeted at key biogeochemical intervals including the uppermost sediment column and two sulfate–methane transitions.

A total of 106 IW samples were obtained from Site 1229. From Hole 1229A, 52 samples were collected at an average resolution of two to three per core, except in Cores 201-1229A-9H, 10H, 11H, and 12H, where resolution was increased to five to seven samples per core (about one per section), and in Cores 6H and 7H, where no samples were recovered between 42.9 and 60.2 mbsf. Sampling in Hole 1229D included a bottom-water sample (WSTP) and high-resolution coverage (five to seven samples per core) of the first five cores between 0 and 40.7 mbsf.

Two samples per core were collected between 40.7 mbsf and the bottom of the hole at 107.6 mbsf, except in the case of the intervals between 77.8 and 84.3 mbsf and 96.8 and 106.3 mbsf, where samples were not available.

As at previous Leg 201 sites, we determined concentrations of important electron donor/acceptor species and microbial metabolites including volatile fatty acids (acetate and formate), methane, ethane, propane, hydrogen, ammonium, phosphate, DIC, sulfate, iron, and manganese.

Alkalinity and DIC have similar profiles. As at Site 1228, alkalinity and DIC have two maxima, one between 1 and 2 mbsf and a second maximum at ~30 mbsf. Recognition of the maximum between 1 and 2 mbsf was achieved through high-resolution interstitial water sampling, which included eight samples in Section 201-1229D-1H-1 (Fig. F5A, F5B).

Alkalinity in the upper 2 mbsf ranges from 12.6 mM between 0.12 and 0.25 mbsf to 21.6–22.0 mM between 1 and 2 mbsf (Table T2; Fig. F5A). Alkalinity decreases to 14.4 mM at 16 mbsf before increasing again to a second maximum of 19.1 mM at 31 mbsf. Alkalinity then decreases gradually to <6 mM at the bottom of Hole 1229A.

The DIC profile is very similar to the alkalinity profile, with two maxima at ~2 and 30–40 mbsf (Fig. F5B). In the upper 2 m of the sediment column, DIC ranges from a low value of 11.6 mM in the upper few centimeters to 21 mM at 1.35 mbsf. DIC concentrations then decrease to 13.3 mM at 15.7 mbsf before increasing again to a second maximum of 20–21 mM over a depth range from 28 to 54 mbsf. They then decrease gradually to 6.8 mM at the bottom of Hole 1229A.

Sulfate concentrations were determined for 102 interstitial water samples from Holes 1229A and 1229D. Sulfate declines rapidly in the upper 3 m of Hole 1229D and reaches a local minimum of 14.1 mM at 3.25 mbsf. This local minimum is followed by a rise to 15.3 mM at 6 mbsf and is then followed by a more gradual steady decline to 0 mM by ~38 mbsf (Fig. F5C). Sulfate then reappears at 90.2 mbsf and increases steadily toward a final measured value of 38.0 mM at the bottom of Hole 1229A.

Dissolved sulfide ($\Sigma H_2S = H_2S + HS^-$) exhibits a sinuous profile at Site 1229, consistent with the profiles of other interstitial water reactants and products, including sulfate and DIC (Fig. F5E). Sulfide concentrations are present at 2.34 mM in the uppermost 12 cm and increase steeply to a peak concentration of 6.37 mM at 2.34 mbsf. The sulfide profile exhibits a minimum of 4.5–5 mM centered at 14 mbsf, followed by a broad maximum of 5.8–6 mM between 22 and 38 mbsf. The sulfide profile broadly correlates with the DIC profile n the uppermost 50 mbsf. These profiles collectively indicate distinct zones of maximal sulfate reduction at 2 mbsf and 25–35 mbsf. The deeper zone is coincident with the shallow sulfate–methane transition zone. Sulfide concentrations decrease to 2 mM over the sulfate-free methane-rich zone between 66 and 80 mbsf, which suggests removal of sulfide in this zone. Low scattered values of sulfide in the interval from 77 to 82 mbsf are considered to be a sampling artifact. Slightly elevated concentrations are present between 86 and 97 mbsf, where values reach 3.0 mM. Below this, sulfide concentrations decrease linearly with increasing depth, approaching a concentration of <0.07 mM by 166 mbsf and <0.001 mM at 186 mbsf.

As at other sites drilled during Leg 201, IW barium concentrations at Site 1229 (Fig. F5F) vary antithetically with sulfate concentrations. Bar-

ium is close to the detection limit (~0.1 µM) at the sediment/water interface, where sulfate is high, but sharply rises to 19 µM at 42 mbsf, where sulfate is below detection limit. Across the sulfate-depleted zone at Site 1229 from 42 to 86 mbsf, barium concentrations range between 16.5 and 19 µM. Below this interval, sulfate concentrations steadily rise and dissolved barium concentrations decrease to 0.5 µM at 156.75 mbsf. The overall barium profile at Site 1229 most likely is controlled by barite solubility. Interestingly, however, barium concentrations at the bottom of the hole exceed those at the top, despite higher sulfate concentrations at the bottom.
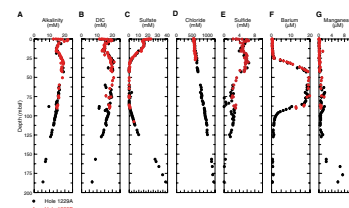
With the exception of one sample at 76.85 mbsf, the dissolved manganese concentrations at Site 1229 (Fig. F5G) are low (<2 µM) over the upper 115 mbsf. Below this depth, dissolved manganese concentrations rise to >6 µM at 166.25 mbsf. Site 1229 is located at the upper boundary of a strong oxygen minimum zone.

The low dissolved manganese concentrations may reflect a lack of solid manganese inputs because they are reduced in the water column or in the upper few centimeters of the seafloor. Interestingly, however, lightly elevated concentrations of dissolved manganese (~2 µM), centered at ~69 and 92 mbsf, suggest reduction of some manganese-bearing phase in the middle of the sediment sequence. The sample with anomalously high manganese (and iron) concentrations (Sample 201-1229A-9H-6, 95–110 cm) may be affected by an unknown artifact or contamination.

The dissolved iron profile (Fig. F5H) shows a high degree of scatter but generally low values (<2 µM) down to ~125 mbsf, with one exception. Between 78 and 92 mbsf, the iron concentrations of several samples are >10 µM. Iron concentrations are also relatively high (>5 µM) below 125 mbsf. Most labile iron in the sediment column at Site 1229 has probably been precipitated as sulfides.

Dissolved strontium concentrations (Fig. F5I) rise significantly from 90 µM at the seafloor to 360 µM at 186 mbsf. As at Sites 1227 and 1228, the strontium gradient of Site 1229 decreases with depth, changing from 2.1 µM/m over the upper 100 m to 0.6 µM/m over the lower 90 m. Interestingly, of the three sites, the curvature to a smaller gradient occurs deepest and is most pronounced at Site 1229. The steep strontium gradients and curvature imply both a diagenetic release of strontium in the cored section and a flux of strontium from deep brines to shallow sediment and seawater. The similarity in the strontium concentration gradients at Sites 1228 and 1229 suggests that brines beneath these two holes are similar in chemical composition.

Dissolved lithium concentrations (Fig. F5J) rise from 27 µM at the seafloor to 184 µM at the bottom of the hole. However, unlike at Sites 1227 and 1228, this ~1.0-µM/m increase in lithium is less than the increase in strontium. The cause of the range in lithium gradients is unknown but, in contrast to the strontium gradients, may suggest differences in diagenetic exchange and in the composition of the source brine. Nonetheless, as at the other sites, a substantial flux of lithium occurs from deep brine to the shallow sediment and seawater.

The ammonium profile in the upper 43 m at Site 1229 is very similar to that observed at Site 1228. It has two distinct maxima, one between 1.3 and 4.3 mbsf (as at Site 1228) and a second broader maximum (~5000 µM) centered between ~50 and 75 mbsf (Fig. F5K). Below 75 mbsf there is a linear decrease to ~4000 µM at 159.75 mbsf.

As at Sites 1227 and 1228, the dissolved phosphate concentration was determined on splits of 55 IW samples (46 from Hole 1229A and 9

from Hole 1229D) that were previously analyzed for alkalinity in order to overcome chemical interferences from hydrogen sulfide (see "Biogeochemistry," p. 14, in the "Site 1227" chapter).

The upper 10 m of the phosphate concentration profile in Hole 1229D (Fig. F5M) is very similar to the Site 1228 profile, with maximum concentrations of ~42 µM in the upper 2 mbsf and a decline to a local minimum of 6.6 µM at 12.2 mbsf. Below 12.2 mbsf, phosphate concentrations increase toward a second local maximum of 12.7 µM at 31.25 mbsf. Between ~40 and 71 mbsf, phosphate concentrations decline gradually to 4–5 µM at a depth of 160 mbsf and then increase to 7.8 µM at 186.2 mbsf. The sharp decrease above 12 mbsf and relatively small range below is consistent with control of phosphate by apatite solubility below this depth.

Dissolved silica concentrations in Holes 1229A and 1229D are fairly constant by 18 mbsf and range between ~950 and 1050 µM over most of the site (Fig. F5M). These values likely reflect control by biogenic silica solubility in these diatomaceous sediments.

Chloride exhibits a regular and steady increase with depth, as at Sites 1227 and 1228 (Fig. F5D). Chloride concentrations range from 555.7 mM near the sediment/water interface to a maximum of 1208.2 mM at 186.2 mbsf at the bottom of Hole 1229A.

The concentrations of acetate and formate were analyzed in 57 IW samples from Holes 1229A and 1229D (Table T2; Fig. F5N, F5O). Overall, the concentrations of both compounds are similar to those at Site 1227 and higher than those at Site 1228. Acetate concentrations range from 0.7 to 11.9 µM, and formate concentrations range from 0.6 to 12.1 µM. Maximum concentrations of both acids are present in the two sulfate–methane transition zones (~40 and ~90 mbsf) and close to the bottom of Hole 1229A. Concentrations in other depth intervals of Site 1229 are commonly low, with the majority of values <2 µM.

Methane was detected in all samples at Site 1229 (Table T3; Fig. F5P). In addition, ethane and propane were found in the majority of samples (Table T3; Fig. F5Q, F5R). As noted in the chapters for previous sites, increasing extraction times led to increased yields (Table T3). In the following discussion of methane concentrations in a stratigraphic context, we will discuss in detail the data series from the 8-day extraction of samples from Hole 1229A, which yielded consistently higher values than shorter extraction.

Concentrations of methane are 1.5 µM near the sediment/water interface and increase to ~80 µM at 21.70 mbsf. There is an almost threefold increase in methane concentrations over the next 2 m. Between 23.35 and 37.9 mbsf, methane concentrations are fairly uniform at levels slightly >200 µM. The depth interval around 37.9 mbsf (upper shaded bar in Fig. F5P) coincides with the transition zone, where sulfate concentrations decrease to undetectable levels. From 37.9 to 41 mbsf, methane concentrations increase sharply to ~800 µM but then drop again to <400 µM at 43.65 mbsf. This somewhat unusual decrease in the upper portion of the "methanogenic" sediment is associated with an erosional layer that marks the boundary between lithostratigraphic Subunits 1A and 1B. Poor recovery in this interval precluded methane analyses until a depth of 60.2 mbsf, where its concentration reaches 1260 µM. Concentrations of methane remain high to a depth of 76.80 mbsf, with the majority of values in excess of 1000 µM. Below 85.20 mbsf, concentrations decrease sharply from slightly above 500 µM to 17 µM at 93.40 mbsf within the second sulfate–methane transition zone created by the sulfate-rich brine (lower shaded bar in Fig. F5P). Be-

T3. Methane in headspace, p. 69.

low the second sulfate–methane transition zone, methane concentrations are relatively low (between 13 and 102 µM).

The concentrations of ethane and propane are <1 µM in the top 100 mbsf at Hole 1229A. In more deeply buried sediments, concentrations of both compounds peak at ~120 and 160 mbsf, with ethane values being 2 and 2.5 µM, respectively (Fig. F5Q). Propane concentrations in those intervals are slightly higher (Fig. F5R). Concentrations of both gases drop noticeably at the more deeply buried transition zone at ~90 mbsf, whereas the relative decrease at the upper transition zone appears less pronounced.

Hydrogen incubations were conducted on 20 samples from Hole 1229A and 10 samples from Hole 1229D (Table T4; Fig. F5S). Concentrations range between ~0.1 and ~4 nM, with most samples between ~0.1 and ~0.5. It is interesting to note that the highest-concentration samples were in the sulfate–methane transition zone.

MICROBIOLOGY

Microbiological sampling of Site 1229 covered the sulfate-reducing zone near the sediment/water interface, the sulfate-depleted methanogenic zone between ~35 and 90 mbsf, and the sulfate-rich deep layer at depths between 90 and 186 mbsf, which was influenced by the presence of a deep subsurface brine. Whenever possible, two sections of each core from the upper 100 m of the sediment column were routinely sampled for deoxyribonucleic acid (DNA) analysis, measurements of sulfate reduction rates, hydrogen concentration and turnover, methanogenesis rates, acetate turnover, thymidine incorporation, bacterial lipid biomarkers, adenosine triphosphate, fluorescent in situ hybridization (FISH), and iron/manganese/sulfur solid-phase geochemistry (Fig. F6) (Cores 201-1229A-2H through 11H). Poor recovery of Core 201-1229A-7H (49.5–59 mbsf) led to this depth interval being substituted with two core sections from the same depth interval of Hole 1229D (Sections 201-1229D-7H-1 and 7H-4) (Fig. F7). Every core that could be obtained from the deeper layers of the sediment column was sampled to analyze the prokaryotic communities and activities in the deep sulfate-rich layer (Sections 201-1229A-12H-3 through 22H-2) (Fig. F6).

Sampling in Hole 1229D focused on fine-scale resolution of intervals that had been missed or inadequately sampled in Hole 1229A. Sampling in five sections of the mudline core in Hole 1229D (Sections 201-1229D-1H-1,1H- 2, 1H-3, 1H-4, and 1H-5) aimed at fine resolution of the highly compressed chemical gradients at the top of the sediment column in order to provide good end-member data for the microbiological and geochemical analyses in deep sediment layers (Fig. F7). Sampling in Sections 201-1229D-4H-3, 4H-4, and 4H-5 aimed at resolving the low-sulfate interval between 30 and 33 mbsf, where sulfate declines to <1 mM (Figs. F6, F7). The two bottom sections of the short Core 201-1229D-12H (Sections 12H-2 and 12H-3) and the consecutive two top sections of Core 13H (Sections 13H-1 and 13H-2) were sampled to obtain a fine resolution in the lower sulfate–methane transition zone between 85 and 90 mbsf (Fig. F5) that had not been sampled sufficiently in Cores 201-1229A-10H and 11H (Fig. F7). In addition, specific samples were recovered in Hole 1229D from defined depths that had not been sampled in sufficient detail at similar depths in Hole 1229A (Sections 201-1229D-2H-5, 6H-1, 9H-4, and 15H-3).

Total Prokaryotic Cell Enumeration

During core processing in the 10°C reefer, sample plugs (1 cm³) for total prokaryotic cell enumeration were taken from a total of 24 depths between 8.88 and 185.7 mbsf in Hole 1229A (18 samples) and between 0.01 and 53.86 mbsf in Hole 1229D (6 samples). Prokaryotes were present in all samples to 185.7 mbsf (Fig. F8). The highest number was found at 90.45 mbsf (Sample 201-1229A-11H-2, 5–11 cm), which contained 9.5×10^9 cells/cm³. The lowest number was at the base of the hole, with 2.7×10^6 cells/cm³, 3500-fold lower than at 90.45 mbsf.

The overall depth profile of cell numbers per cubic centimeter follows a trend observed at other ODP sites (Parkes et al., 1994), with many of the data lying very close to, or on, the mean regression line (Fig. F9). Two zones of major interest, just above the 35-mbsf upper sulfate–methane transition and the lower sulfate–methane transition at ~90 mbsf (see "Biogeochemistry," p. 12) were intensively sampled. Prokaryotic cell numbers were very high at these depths and in both cases exceeded the upper 2-σ envelope of the existing database. The upper sulfate–methane transition zone showed elevated counts between 20.98 mbsf (Sample 201-1229A-3H-5, 58–60 cm) and 40.35 mbsf (Sample 5H-5, 95–100 cm), with a maximum of 1.18×10^8 cells/cm³ at 29.81 mbsf (Sample 201-1229D-4H-3, 101–107 cm). This represented a tenfold increase over predicted cell counts at that depth. The increase in cell numbers at the lower sulfate–methane transition zone was broader, lying between 84.48 mbsf (Sample 201-1229A-10H-4, 58–64 cm) and 157.98 mbsf (Sample 18H-2, 108–114 cm). The lower boundary may represent a sampling artifact, since data points between 125 and 158 mbsf were not available. Within this broad band of increased cell numbers, a peak was present at 90.45 mbsf (Sample 201-1229A-11H-2, 5–11 cm) with 9.48×10^9 cells/cm³, which represented a 1730-fold increase over predicted cell counts at that depth. This value was exceptionally high for a deep marine sediment. To our knowledge, this is the highest prokaryotic cell count ever found well below the seafloor. To exclude potential sources of error and bias, the counts were repeated. Solutions were refiltered, new sterile equipment was used, blanks were checked, and a different person redid the count. The original enumeration was confirmed.

The peak in prokaryotic numbers at 90.45 mbsf was present within a prominent gray homogeneous quartz- and feldspar-rich clay (see "Subunit IB," p. 9, in "Description of Lithostratigraphic Units" in "Lithostratigraphy"). To confirm the high prokaryotic cell counts, additional subsamples were taken from two other independently sampled sources within the same clay zone for enumeration. These were a 0.2-mL slurry sample from 91.14 mbsf (Sample 201-1229A-11H-2, 88–93 cm) and a 1-cm³ whole-round core (WRC) sample from 91.28 mbsf (Sample 11H-2, 103–109 cm). These gave prokaryotic cell counts of 5.81×10^8 and 2.06×10^9 cells/cm³, respectively (Figs. F8, F9). The mean prokaryotic cell count density in this narrow 83-cm band amounts to 2.25×10^9 cells/cm³, a 410-fold increase over the mean cell number from all previously published sites at this depth.

Numbers of dividing cells (suggested as an index of growth activity) are typically <10% of the total count. As expected, dividing cells, as a percentage of the total count, are high near the surface (Fig. F8). They decrease to a minimum at 20.98 mbsf (Sample 201-1229A-3H-5, 58–60 cm), before increasing again. Interestingly, the maximum percentage of dividing cells around the upper sulfate–methane transition zone is

F8. Prokaryotic cells enumerated by AODC, p. 44.
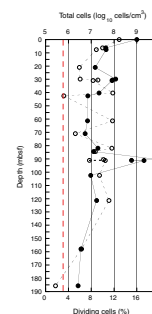
F9. Total prokaryote profile, p. 45.
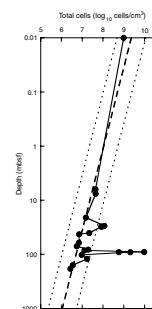
present at 40.35 mbsf (Sample 201-1229A-5H-5, 95–100 cm), well below the maximum direct count. In all cases where a reliable quantification was possible, the proportion of dividing cells amounted to ~10% of the total counts below the upper sulfate–methane transition zone and also at the prokaryotic cell abundance peak at the deeper sulfate–methane transition zone.

The high amount of organic matter and the silty clay with very small particle size made direct counting at this site more problematic than usual. Generally, subsamples of 15–40 µL can be processed, but in this case subsample size was restricted to a maximum of 10–12 µL. Consequently, the detection limit increased to 5.8×10^5 cells/cm^3. The percentage of dividing cells should be viewed with caution where the direct count is $<1 \times 10^7$ cells/cm^3.

Contamination Tests

While drilling cores for microbiology, the potential for contamination with bacteria from the surface is highly critical. Contamination tests were continuously conducted using solutes (PFT) or bacterial-sized particles (fluorescent microspheres) to check for the potential intrusion of drill water from the periphery toward the center of cores and thus to confirm the suitability of the core material for microbiological research. We used the chemical and particle tracer techniques described in ODP *Technical Note* 28 (Smith et al., 2000). Furthermore, the freshly collected cores were visually examined for possible cracks and other signs of disturbance by observation through the transparent core liner. Core sections observed to be disturbed before or after subsampling were not analyzed further. Such disturbance phenomena are critical to the integrity of the core material and therefore also to its usefulness for microbiological studies.

Perfluorocarbon Tracer

PFT was injected continuously into the drilling fluid during drilling of Holes 1229A and 1229D (see **"Perfluorocarbon Tracer Contamination Tests,"** p. 26, in "Microbiological Procedures and Protocols" in "Microbiology" in the "Explanatory Notes" chapter). PFT concentration analyses focused on microbiology cores and especially on sections that were used for slurry preparation and cultivations. To compare the PFT concentrations in the center of a core to the PFT concentrations at the periphery of the same core, a 5-cm^3 subcore sample was also taken at the core periphery, adjacent to the core liner. Whenever possible, the samples were taken directly on the catwalk because the PFT content of catwalk air was usually not detectable.

Low levels of potential seawater contamination (Table **T5**) were found for the center portions of all tested cores of Holes 1229A and 1229D. With one exception (Section 201-1229A-6H-2), the values were not higher than 0.07 µL seawater/g sediment (average = 0.039 µL seawater/g sediment). The outer portions of all tested cores had a significantly higher level of PFT tracer and potential seawater contamination. In all cases, the PFT content and the estimated potential seawater contamination levels were higher in the periphery of the core than in the center (see **House et al.,** this volume).

Of the eight master slurry samples taken from Site 1229 (Table **T6**), only the slurries from Cores 201-1229A-9H and 11H showed small con-

T5. Seawater contamination based on PFT, p. 73.

T6. Potential contamination of slurries based on PFT, p. 74.

centrations of PFT (~0.06 µL potential seawater contamination/mL slurry).

Assuming 5×10^8 prokaryotic cells/L surface seawater, each 0.1 µL seawater contamination may represent as many as 50 contaminating cells if the sediment is porous enough to allow cells to travel with the PFT.

Particulate Tracer

Fluorescent microspheres (beads) were deployed on all eight cores from which slurries were made at this site. For each slurry, two subsamples were processed: (1) a sample of the slurry to check contamination and (2) a scraping from the outer surface of the core to confirm deployment of microspheres.

Microsphere deployment was confirmed from the outer core scrapings in all six cores that were sampled for slurry preparation (Table T7). Microspheres were detected in two slurry samples. In Sample 201-1229A-3H-2, 40–54 cm, a single bead was observed; further microscopic searching of the membrane failed to detect any additional beads. It is believed that a single microsphere represents filter handling and processing effects rather than contamination (see **"Fluorescent Microparticle Tracer,"** p. 27, in "Procedures and Protocols" in "Microbiology" in the "Explanatory Notes" chapter). In Sample 201-1229A-11H-2, 74–88 cm, however, three microspheres were observed within the counting grid and many more microspheres were present outside of the counting area. It therefore seems likely that this sample was contaminated.

Cultivations

Since the complex geochemical profiles of Site 1229 (Fig. F5) indicate distinct zones of contrasting microbial activities, slurry samples from nine different depths were used for cultivation experiments (Table T8). These slurries included the eight master slurries checked for contamination (Table T7) and an additional slurry from Core 201-1229D-15H for enrichments of predominantly thermophiles. Slurries for cultivation were prepared by subcoring with two 60-mL syringes from the center of two freshly broken surfaces after precutting the core liner with the ODP cutter. This technique provided untouched (although not always smooth) surfaces that were immediately sampled. The inoculated media were selective for fermentative prokaryotes, sulfate reducers, methanogens, and various anaerobic chemolithoautotrophic and heterotrophic prokaryotes that use iron(III) or manganese(IV) as an electron acceptor. Quantitative cultivations (most probable number [MPN] experiments) and enrichment cultures were started at temperatures between 15° and 80°C. For this site, additional microbiological work was undertaken considering the following aspects:

1. To quantify culturable methanogens at different depths in the sediment column, dilution series were prepared using substrates that are characteristic for major physiological and phylogenetic groups of methanogens. Two of these substrates, methyl amines (typically found in nearshore environments) and hydrogen/carbon dioxide can also be used by acetogens. Potentially, acetogens could provide acetate for the sulfate reducers at the sulfate/methane interface.

2. In order to study the role of sulfate as a limiting electron accep-
    tor, both sulfate-free and sulfate-containing media were used for
    inoculation of samples from the sulfate-containing sediment
    layers, the sulfate–methane transition zone, and sulfate-free
    sediment layers. Whereas the normal sulfate-containing media
    were reduced with FeS, the sulfate-free media were reduced with
    titanium citrate and were kept sulfide-free to exclude sulfide ox-
    idation to sulfate.

3. A considerable proportion of subsurface prokaryotes could be
    spore-forming bacteria. Spores are bacterial resting stages that
    are resistant to environmental stress factors, such as nutrient de-
    pletion, desiccation, heat, and irradiation. To quantify the con-
    tribution of spore-forming bacteria to the total cultivable
    prokaryotic community, pasteurized (heated to 80°C for 10 min)
    and untreated slurries were used in parallel for MPN experi-
    ments. All shipboard cultivation experiments and the media and
    incubation temperatures are shown in Table **T8.** For details of
    the various media compositions and incubation conditions see
    Tables **T4,** p. 84, **T5,** p. 85, and **T7,** p. 88, and **"Procedures and
    Protocols,"** p. 25, in "Microbiology," all in the "Explanatory
    Notes" chapter.

FISH-SIMS

^{13}C substrate incubations were initiated for postcruise analysis by flu-
orescence in situ hybridization–secondary ion mass spectrometry (FISH-
SIMS) using material from Cores 201-1229A-2H, 3H, 4H, 6H, and 11H.
In each case, 10 mL of the master slurry was injected into each bottle.
The ^{13}C substrates used were methane, acetate, and glucose. For Cores
201-1229A-4H and 11H, an additional acetate bottle was inoculated,
and for Core 11H, no glucose bottle was used.

PHYSICAL PROPERTIES

At Site 1229, we collected a full range of physical property data from
Hole 1229A, which extended from the seafloor to a depth of 194.4
mbsf. All cores in Hole 1229A except Core 201-1229A-20M were taken
by APC. Samples were taken from four additional holes drilled at Site
1229 to address high-resolution objectives and spot-coring needs. All
cores from each hole were run through the multisensor track (MST),
with Hole 1229E at higher resolution and Holes 1229B, 1229C, and
1229D at standard resolution. No discrete moisture and density (MAD)
samples or split-core measurements were collected from these subse-
quent holes.

The physical property data from these cores are described below and
compared with those from Site 681 (Shipboard Scientific Party, 1988).
The local stratigraphic record was extended from 187.0 mbsf in Hole
681A to 194.4 mbsf in Hole 1229A, though core recovery at Hole 1229A
was very poor below 130 mbsf where sediments consisted of semicon-
solidated clayey silts and unconsolidated feldspar- and magnetite-bear-
ing quartz sands. Above 130 mbsf, Holes 1229A and 1229D provide
>90% recovery for MST and split-core physical property profiles. We
have incorporated wireline logs from the triple combo tool string,
which provide a continuous record between ~70 and 170 mbsf, with

the shipboard physical property logs to provide an almost complete physical description of the sediments at Site 1229.

Each section of WRC that was analyzed for physical properties was first degassed for up to 2 hr on the catwalk, if necessary, for safety (because of high hydrogen sulfide levels), was equilibrated to laboratory temperature (2-4 hr), and then was run on the MST. The standard-resolution measurements were magnetic susceptibility (spacing = 5 cm, data acquisition scheme [DAQ] = 2×1 s), gamma ray attenuation (GRA) density (spacing = 10 cm, count time = 5 s), *P*-wave velocity (spacing = 10 cm, DAQ = 10), and NGR (spacing = 30 cm, count time = 15 s). Thermal conductivity measurements were made on the third section of each whole-round core in Hole 1229A, where possible. Some sections were removed from the catwalk for microbiology and interstitial water sampling. Physical properties were measured on these sections only if intact parts remained following the sampling. This limited the continuity and, hence, spatial resolution of the physical property record.

MAD, *P*-wave velocity from the digital velocimeter, and resistance data (translated to formation factors as detailed in **"Formation Factor,"** p. 47, in "Physical Properties" in the "Explanatory Notes" chapter) were collected regularly only from Hole 1229A. MAD samples were taken at a frequency of one per section and at higher resolution in sections with many voids or lithologic transitions. MAD samples were co-located with the methane headspace extractions where possible to facilitate the volumetric analysis of methane concentrations.

Instrumentation, measurement principles, and data transformations are discussed further in **"Physical Properties,"** p. 41, in the "Explanatory Notes" chapter.

In general, the wireline logs and physical data that record burial history (bulk density, resistivity, and *P*-wave velocity) show expected downhole trends controlled by interstitial dewatering with increasing overburden. The measurements most responsive to lithologic variations (magnetic susceptibility, grain density, and NGR) have preserved a record of cyclic sedimentation, and these higher-frequency variations are clearly superimposed on the burial signatures.

We recognize three broad zones in the characteristics of the physical property data: 0–40, 40–138, and 138–194.4 mbsf. The first boundary (40 mbsf) is a distinct lithologic change, whereas the second boundary (138 mbsf) has been chosen at the base of a transitional sequence extending from 125 to 138 mbsf. Within the 40- to 138-mbsf zone, four sedimentary sequences of biogenic siliciclastic deposition are identified, between 40 and 62 mbsf, 62 and 88 mbsf, 88 and 125 mbsf, and 125 and 138 mbsf. In the following sections, we describe the main characteristics of each physical property in terms of these intervals, relating them (where possible) to the lithostratigraphic divisions given in **"Description of Lithostratigraphic Units,"** p. 8, in "Lithostratigraphy."

Infrared Scanner

The infrared scanner was not employed at this site.

Magnetic Susceptibility

Low-field volume magnetic susceptibility was measured on the MST using the Bartington loop sensor as described in **"Magnetic Susceptibility,"** p. 44, in "MST Measurements" in "Physical Properties" in the "Explanatory Notes" chapter. Data were collected on WRC sections

from deep Holes 1229A and 1229D at standard resolution (spacing = 5 cm, DAQ = 2 × 1 s). The interval of low recovery in Hole 1229A from 40 to 60 mbsf was subsequently covered by sediments from Hole 1229D (Fig. F10A). Hole 1229D terminated at 112.8 mbsf, and data are missing from Hole 1229A over the intervals 113–118, 128–138, and 140–155 mbsf. Both data sets match well, especially above 70 mbsf, but both are increasingly noisy from 80 to 112 mbsf. Despite this interference, we were still able to discern the underlying trends.

The magnetic susceptibility record can be divided into the three zones described above. The uppermost, from 0 to 40 mbsf in Hole 1229A, corresponds to Subunit IA (see "Description of Lithostratigraphic Units," p. 8, in "Lithostratigraphy"). It is characterized by a low response of 2×10^{-5} to 5×10^{-5} SI units but with three narrow peaks (at 2.5, 15, and 20 mbsf) that reach between 10×10^{-5} and 45×10^{-5} SI units. The 15- and 20-mbsf peaks appear in the records of both Holes 1229A and 1229D and coincide with silt interlayers. At 40 mbsf, there is a sharp increase in average magnetic susceptibility to ~23×10^{-5} SI units; from 40 to 42 mbsf, the signal fluctuates widely. We consider the horizon delineated by this increase to be a significant physical property boundary.

We define a second physical property zone between 40 and 138 mbsf. This zone incorporates Subunits IB and IC. Across this interval all physical property records are characterized by a cyclic pattern that is repeated every 10 to 30 m. The pattern is not as clear in the susceptibility record as it is in the other property profiles. Data from Hole 1229D indicate that the high-susceptibility interval at the top of this zone is 8–9 m thick. Susceptibility generally decreases from ~23×10^{-5} SI units at 45 mbsf to ~0×10^{-5} SI units at 85 mbsf. There is increasing variation in the signal, averaging ~15×10^{-5} SI units to 108 mbsf. From 108 to 120 mbsf, susceptibility remains ~$0–10 \times 10^{-5}$ SI units. From 120 to 138 mbsf, the average susceptibility increases but exhibits large fluctuations, probably as a result of closely spaced interbeds of diatomaceous ooze and clastic silt or sand.

The lowermost zone extends from 138 mbsf to the base of the hole. Over this interval, magnetic susceptibility averages 35×10^{-5} to 45×10^{-5} SI units. Missing data from 140 to 155 mbsf and from most of the section below 170 mbsf make it impossible to determine a trend across this interval.

Magnetic susceptibility data from Site 681 were collected postcruise by Merrill et al. (1990). They are reproduced here for comparison in Figure F10B. Their record is complete only across the uppermost 50 mbsf, where they show good agreement with Site 1229 data. Below 50 mbsf, Site 681 records are too incomplete to enable detailed comparisons.

Paleomagnetism

At Site 1229, we collected 16 discrete samples for paleomagnetic measurements. The sampling frequency was two samples from each core in Cores 201-1229A-2H through 8H (2.9–61.0 mbsf) and one sample from each core below this interval to the bottom of the hole (Cores 201-1229A-9H through 22H; 61.0–194.4 mbsf). Alternating-field (AF) demagnetization of the natural remanent magnetization (NRM) was conducted up to 40 mT in 10- or 5-mT steps. Anhysteretic remanent magnetization (ARM) was measured to 40 mT in 10-mT steps with a 29-

F10. Comparison of magnetic susceptibility, p. 46.
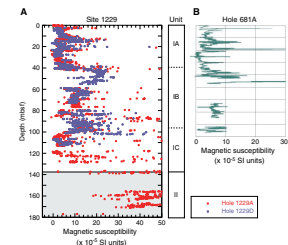
µT direct current–biasing field. AF demagnetization of the ARM was
conducted to 40 mT in 10-mT steps.

Samples from lithostratigraphic Subunits IA and IC through Unit II
(see **"Description of Lithostratigraphic Units,"** p. 8, in "Lithostratig-
raphy") indicate higher magnetic intensity after 20-mT AF demagneti-
zation (Fig. **F11**). The intensity peak in lithostratigraphic Subunit IA at
23 mbsf correlates with the intensity peak at the lower Brunhes/Matu-
yama boundary (18 mbsf) identified from Hole 681A (Shipboard Scien-
tific Party, 1988). Although stepwise AF demagnetization shows a
downward drilling-induced overprint, we were able to isolate the origi-
nal magnetic direction in lithostratigraphic Subunit IA in Cores 201-
1229A-3H through 4H and in Subunit IC in Core 201-1229A-14H. Sub-
unit IA is characterized by dark brown diatom- and clay-rich silt with
pale yellow nannofossil-rich laminae and layers of gray silt. Demagneti-
zation of a sample from the pale yellow laminae (Sample 201-1229A-
4H-6, 70–72 cm) reveals an original magnetic direction (Fig. **F12**). De-
magnetization of the dark brown diatom- and clay-rich silt (Sample
201-1229A-3H-3, 65–67cm) in lithostratigraphic Subunit IA and lami-
nated clay- and silt-rich diatom ooze (Sample 201-1229A-14H-3, 110–
112 cm) in the middle part of lithostratigraphic Subunit IC reveals shal-
low inclinations (Figs. **F13, F14**) near that expected for a geocentric ax-
ial dipole at this latitude (21°) after removal of the drilling-induced
overprint.

Gray siliciclastic layers in lithostratigraphic Subunit IB and Unit II
consist of feldspar- and quartz-rich sand with variable proportions of
clay. This interval is coarser grained than the rest of lithostratigraphic
Unit I. The sediments in this interval have a relatively high NRM inten-
sity (Fig. **F11**) and magnetic susceptibility; however, we cannot resolve
the original magnetic component because of the strong drilling-
induced overprint.

Density and Porosity

Density data were measured on the MST by the GRA densitometer
(spacing = 10 cm, count time = 5 s) and calculated from split-core mass/
volume measurements. Porosity was calculated from the split-core sam-
ples. The density and porosity data sets show expected changes with
lithostatic loading. Both MST GRA and discrete-sample bulk density in-
crease from ~1.2–1.3 g/cm³ at the top of the hole to ~1.8 g/cm³ at the
base (Fig. **F15A**). Porosity decreases from 80% to 40% over the same in-
terval (Fig. **F15C**). The three physical property zones are clearly identi-
fied, with good resolution of the sedimentary sequences between 40
and138 mbsf (Subunits IB and IC). The most complete records in the
lowermost two-thirds of Hole 1229A are the wireline records of bulk
density, porosity, and resistivity (Figs. **F15, F16**), but the same patterns
are evident in the less continuous shipboard GRA and MAD bulk den-
sity, grain density, and porosity data.

In combination, these data show that the interval from 40 to 138
mbsf is composed of four cycles of variation in the physical properties.
The cycles shown in Figures **F16** and **F17** range from 13 m (125–138
mbsf) up to 37 m (88–125 mbsf) in thickness. Each cycle consists of two
parts (see Fig. **F17**). In the upper part, bulk densities range from 1.6 to
1.8 g/cm³, with porosities averaging ~60%. The lower part is character-
ized by lower bulk densities (between 1.2 and 1.4 g/cm³) with porosities
ranging up to 80%. Grain densities show a similar pattern, with the up-
per part of a cycle consistently >2.6 g/cm³ and the lower parts between

F11. Magnetic intensity, p. 47.
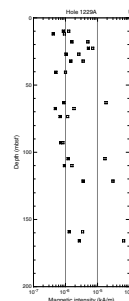
F12. Principal component analy-
sis, 201-1229A-4H-6, 70–72 cm,
p. 48.
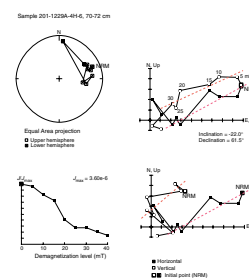
F13. Principal component analy-
sis, 201-1229A-3H-3, 65–67 cm,
p. 49.
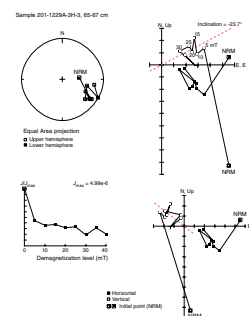
F14. Principal component analy-
sis, 201-1229A-14H-3, 110–112
cm, p. 50.
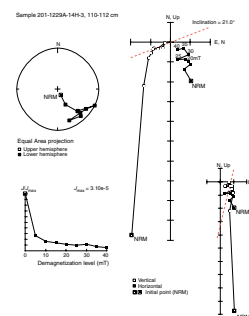
2.3 and 2.4 g/cm³. Each cycle has a sharp base and gradual change in physical properties upward to the base of the next cycle. Wireline resistivity values exhibit a similar pattern (Fig. **F16**).

Examination of the lithostratigraphy (see **"Lithostratigraphy,"** p. 8) shows that the overall interval from 40 to 138 mbsf consists of two main interbedded lithologies: (1) diatomaceous ooze, which forms the principal component of the lower part of the cycle described above, and (2) quartz- and feldspar-rich clay and silt, defined by the higher bulk and grain densities and the lower porosity, making up the upper part of each cycle.

The interval from 138 to 194.4 mbsf is the third and lowermost zone consistently delineated by changes in physical properties, and it corresponds to Unit II (Fig. **F15**). This interval is characterized by high grain and bulk densities (>2.6 and 1.7–1.9 g/cm³, respectively) and low porosity (<50%). These density and porosity variations are consistent with the dominant sand and silt lithologies.

MAD data for Site 681 were collected at very low resolution but generally fall within the range of our data. GRA data from Site 681 (Shipboard Scientific Party, 1988) show mean values and variance similar to those from Site 1229 over the common intervals. The Site 681 data only extend to a depth of 138 mbsf and were too sparse to allow for a full description of the downhole variation.

Compressional Wave Velocity

P-wave data from the MST *P*-wave logger (PWL) were recorded at a 10-cm spacing for all available APC cores from Holes 1229A, 1229B, 1229C, and 1229D and at 2-cm spacing for Hole 1229E. The PWS3 velocimeter was used to measure *P*-wave velocities on split cores from Hole 1229A, with measurements taken at least once per section. Closer-spaced measurements were made at lithologic boundaries and in sedimentary intervals marked by evidence of diagenetic or other petrophysical changes.

P-wave data show a consistent increase in velocity across lithostratigraphic Unit I (physical property zone 1), from 1510 m/s at the seafloor to ~1580 m/s at 138 mbsf (Fig. **F18**). Several diagenetic anomalies are superimposed on the background velocity increase at 13–15, 42–44, 82–84, and ~94 mbsf (see also **"Lithostratigraphy,"** p. 8). The base of Subunit IA at 40 mbsf is particularly evident, with sharply increasing velocities ranging between 1500 and 1750 m/s over the short interval to 43 mbsf. This horizon is marked by interlayered dolomitic and phosphate cements and nodules.

The bases of the two best-defined cycles within the lower part of Unit I (physical property zone 2) at ~83 and 125 mbsf are marked by thin intervals of higher *P*-wave velocities. The tops of these cycles are indicated by slightly higher velocities relative to the immediately adjacent strata, but the cyclic patterns are not as clearly discerned as in the other data (e.g., bulk density and natural gamma ray measurements).

There is a large gap in our MST and discrete sample data over the interval 128–155 mbsf, but the wireline logs all support a boundary at ~138 mbsf. Below this level, *P*-wave velocity is on average much faster than would be predicted from the downhole trend extrapolated from Unit I. Most of the PWS3 velocimeter measurements yielded velocities in the range of 1720–1780 m/s. The lower end of this range was the highest value recorded over the same interval on the MST PWL, where most of the values ranged from 1620 to 1720 m/s. We attribute the ≥50-

F15. GRA bulk and MAD density data, p. 51.
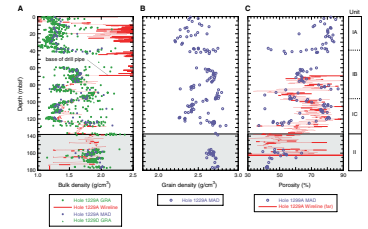
F16. Wireline resistivity, p. 52.
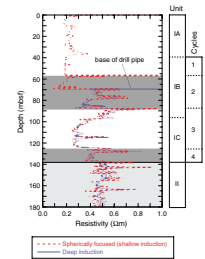
F17. MAD measurements, p. 53.
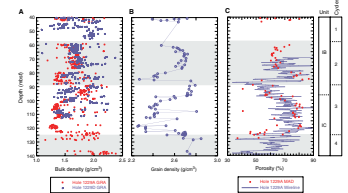
F18. *P*-wave velocity profiles, p. 54.
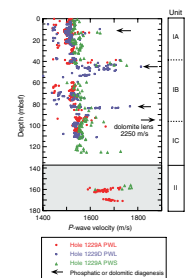
m/s velocity increase in Unit II to the distinct lithology change at ~138 mbsf, below which the sequence is dominated by coarse-grained hornblende-bearing feldspathic sand.

Natural Gamma Ray Emission

NGR was measured on the MST for all Site 1229 holes (spacing = 30 cm, count time = 15 s) except for Hole 1229E, which was run at a higher spatial resolution (spacing = 15 cm, count time = 30 s) for the first five cores and then at 20-cm spacing and 30-s count times (from Section 201-1229E-5H-7). In addition, NGR was recorded with the NGR sonde during the wireline logging run. Both data sets are shown in Figure **F19.** The wireline response is suppressed above ~68 mbsf because of attenuation by the drill pipe. Within Subunit IA, the MST gamma ray response is relatively low at ~20 counts per second (cps), but two spikes at 13 and 20 mbsf appear on both Holes 1229A and 1229D NGR records and in the wireline data. These correspond to quartz- and feldspar-rich silty interbeds. The base of Subunit IA is clearly delineated on all NGR records. It is a narrow interval characterized by large-amplitude fluctuations between ~40 and 42 mbsf. MST and wireline profiles indicate a break at ~56 mbsf, where the trend changes from an upward-decreasing background response (0–56 mbsf) to an upward-increasing background gamma response (56–125 mbsf) seen in both the GRA and wireline data (Fig. **F19B**).

Between 40 and 138 mbsf, the MST NGR data are overall somewhat noisy and do not track the wireline log closely, although common peaks and troughs are apparent. The wireline log, on the other hand, clearly shows the second and third cycles defined by the other physical property measurements (Fig. **F19B**). The lowermost cycle (from 125 to 138 mbsf) is different in NGR character from those above; we suggest this interval is a transition between the underlying sand- and silt-dominated clastic unit (Unit II) and the sequences within Subunit IB and the upper part of Subunit IC.

The gamma ray wireline log suggests that the downward-increasing trend seen at the base of Unit I continues in Unit II to a depth of at least 153 mbsf, at which point the wireline logging terminates. This is coincidently the depth at which we were again able to collect MST and MAD data. The MST NGR record indicates that below 155 mbsf the emissions are again low, which is consistent with the quartz-rich sand and silt lithologies recovered.

Thermal Conductivity

Thermal conductivity measurements were made on Hole 1229A sediments at a rate of one per core (usually the third section, at 75 cm, if this was available). Values range between 0.71 and 1.29 W/(m·K) (average = 0.86 W/[m·K]) (Fig. **F20A**). Average normalized thermal conductivity and bulk density show a high correlation (Fig. **F20B**), indicating that the thermal conductivity is a direct function of water content of the sediments. The combination of high clastic content (i.e., increased grain-scale thermal conductivity) and low porosity in Unit II results in the thermal conductivity anomaly at ~160 mbsf.

F19. MST NGR and wireline profiles, p. 55.
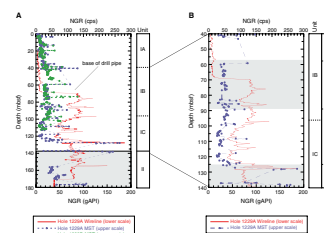
F20. Thermal conductivity measurements, p. 56.
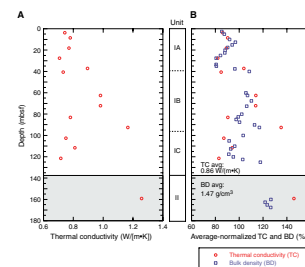
Formation Factor

Formation factor (longitudinal and transverse) was determined for Hole 1229A as described in "Formation Factor," p. 47, in "Physical Properties" in the "Explanatory Notes" chapter, with a minimum sample interval of one per section, increasing if distinct lithologic changes were observed.

The trend of decreasing formation factor with depth for a given lithology represents increasing interstitial water salinity, which causes the sediments to appear more conductive relative to the seawater standard used in the resistivity-formation factor transform. This effect will be corrected in postcruise analysis once the interstitial water chemistry has been completely determined.

Longitudinal (parallel to core axis) formation factors range from 1.1 to 2.5 in the mainly biogenic sediments and 2.5 to 4.9 in the interbedded siliciclastic sediments of Unit I (Fig. F21). The steplike changes in apparent conductivity are consistent with changes seen in other physical properties. Below 138 mbsf (Unit II), the dominant lithology of feldspathic silt and sand produces formation factors of 2.9–3.3. Low formation factors (<2.7) reflect recovery artifacts. Electrical conductivity anisotropy typically ranges from 0% to 12% (average = 6%). Overall, the formation factor measurements track the changing lithostratigraphy, clearly delineating the sedimentary sequences in Unit I.

Summary and Discussion

At Site 1229 there are three physical property zones over the 194.4-m interval drilled. The lowermost of these is dominated by terrigenous quartz- and feldspar-rich sand and silt. Overlying this basal epiclastic unit is an interval of mixed terrigenous and hemipelagic sediments arranged into cycles ranging from 13 to 37 m thick. The uppermost unit is dominated by a hemipelagic facies. The three zones are visible in all physical property data sets. The characteristics of each are summarized below (with the depths taken from Hole 1229A):

1. 0–40 mbsf. This zone is characterized by low magnetic susceptibility, with three peaks at 2.5, 15, and 20 mbsf. Low bulk and grain density correspond to higher porosity in this interval and also exhibit peaks at 15 and 20 mbsf. Natural gamma radiation is low overall, with peaks at 13 and 20 mbsf.
2. 40–138 mbsf. The diagnostic features in this zone are four cycles of upward-increasing density, NGR, and resistivity and upward-decreasing porosity. It also has more variable magnetic susceptibility than the other two zones.
3. 138–194.4 mbsf. This zone has high magnetic susceptibility, high bulk and grain densities, high NGR, and low porosity.

Overall, the physical property data sets correlate well between the different measurements. The sedimentary environmental record is overprinted by a simple burial pattern showing increasing density and *P*-wave velocity with depth and a progressive decrease in porosity. Superimposed on this general pattern, on 10-m scales, is a record of the environmental fluctuation between marine and terrigenous sediment input within an overall transition from marginal to open-marine conditions. The wireline log and less continuous MST and discrete sample physical

F21. Formation factor profile, p. 57.
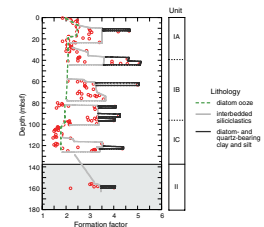
property data provide a template within which a composite lithostratigraphic sequence stratigraphy can be constructed.

DOWNHOLE TOOLS

At Site 1229, the downhole tools employed were the Adara temperature shoe, DVTP, DVTP-P, WSTP, APC-M tool, FPC, and PCS. The results of the temperature and pressure measurements at Site 1229 are described in the two sections below. A short summary of the other tool deployments is provided in the third section.

In Situ Temperature Measurements

One good downhole temperature determination was made in Hole 1229A using the DVTP. An Adara temperature shoe deployment before Core 201-1229A-1H yielded a value for the bottom-water temperature of 14.9°C. The WSTP deployment successfully recorded a value of 15.1°C for water temperature 10 m above the seafloor. Figure F22 shows the data from the successful DVTP deployment at 164.9 mbsf. Four other deployments at 33.4, 68.4, 83.5, and 107.9 mbsf resulted in records that could not be used. Table T9 summarizes Site 1229 temperature measurements together with the Site 681 data.

The results of the DVTP and Adara temperature measurements are displayed in Figure F23. Because we obtained only one good downhole temperature value at Site 1229, the results from Site 681 were included in the thermal gradient estimate. Because of a variety of problems documented by the Leg 112 Shipboard Scientific Party (1988), each of the estimates for Site 681 is denoted as either an upper or lower bound on the true formation temperature. In the combined plot in Figure F23, four of the data points are nearly collinear. These four points yield a linear gradient of 0.0346°C/m in the upper 187 m of the sediment column (Fig. F23). Extrapolating this gradient upward to the seafloor yields a bottom-water temperature of 13.5°C, which is 1.4°C lower than the measured value at Site 681. Although 4°C seasonal temperature variations are possible at 100- to 200-m depths in upwelling systems (e.g., Smith et al., 1991), specific data were not available on board the ship to verify whether 13.5°C is a reasonable mean bottom-water temperature for Site 1229. The extrapolated temperature at the bottom of Hole 1229A, at 192.9 mbsf, is 20.2°C. Multiplying the gradient by an average thermal conductivity of 0.87 W/(m·K) (Fig. F20A) gives a conductive heat flow estimate of 30 mW/m² at Site 1229. This result is equal to the 30 mW/m² value estimated as a lower bound for Site 681 by the Leg 112 Shipboard Scientific Party (1988). It is also close to our estimates of 32 mW/m² for Site 1228 and 37 mW/m² for Site 1227. Figure F23B shows a theoretical steady-state conductive temperature profile calculated using a constant heat flow of 35.5 mW/m², a seafloor temperature of 13°C, and the measured thermal conductivities from the Hole 1229A cores. The theoretical profile is noticeably curved because of the factor of 1.7 downhole increase in thermal conductivity (see Fig. F20A).

The failure rate for DVTP measurements attributed to formation and sea conditions increased at Site 1229 to a high of 80% compared to 50% at Sites 1227 and 1228 and 0% at Sites 1225 and 1226. The one successful measurement at Site 1229 was the deepest deployment attempted at 164.9 mbsf. It was located in lithostratigraphic Unit II, composed of alternating sand and silt (Fig. F1), and the subsequent core had the lowest

F22. DVTP temperature record, p. 58.
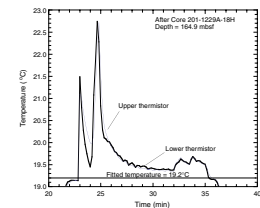
T9. Downhole temperatures, p. 77.

F23. Temperatures vs. depth, p. 59.
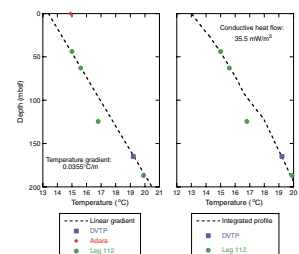
recovery compared to the other four deployments (recovery = 43%). The four unsuccessful deployments were located at shallower depths in silt, clay, or diatom ooze. These results indicate that deployments of the DVTP in shallow water (<200 m) may be more likely to succeed at depths below 150 mbsf.

Davis-Villinger Temperature-Pressure Probe

The DVTP-P was deployed once at Site 1229 at a depth of 79.4 mbsf (after Core 201-1229A-9H). The lithology for this depth was composed of diatom-rich ooze with an average porosity of 75%. The record displayed in Figure F24 exhibits 5-min stops at the seafloor and the base of the hole both before and after the tool was pushed into the sediments. A stepped pressure increase occurred when the tool entered the formation, followed by a sharp drop within 1 min to ~2.42 MPa, which equals the predicted hydrostatic value for the hole depth and measured salinity gradient. For the remainder of the 30-min deployment, the pressure oscillated at 2.42 ± 0.02 MPa. The amplitude of the oscillation corresponds to ~4 m of head, which was comparable to the oscillations at Site 1228. An investigation into the cause of the oscillations is needed.

F24. DVTP-P pressure, p. 60.
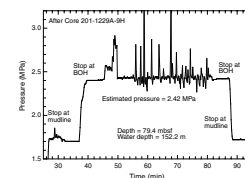
Other Tools

After a failed deployment of the WSTP above Hole 1229A, a sample of bottom water was successfully collected from 10 m above the seafloor at Hole 1229C. Chlorinity data showed that this sample deviated <2% from International Association of Physical Sciences of the Ocean standard seawater (see "Interstitial Water," p. 12, in "Biogeochemistry"). The APC-M tool was run continuously from Cores 201-1229A-2H through 13H. The tool appeared to function correctly, and the data will be analyzed postcruise. The FPC was tested twice at Site 1229 at 24.4 and 174.4 mbsf (Cores 201-1229B-4M and 201-1229A-20M, respectively). Because of a number of mechanical problems, the FPC failed to retrieve pressurized cores on either deployment. The single deployment of the PCS (Core 201-1229D-10P) successfully recovered 0.86 m of sediment from the 2-m cored interval.

DOWNHOLE LOGGING

Operations

One logging run was made in Hole 1229A with the triple combo tool string (see "Downhole Logging," p. 53, in the "Explanatory Notes" chapter). After recovery of Core 201-1229A-22H at 0500 hr on 8 March, the hole was conditioned for logging. The wiper trip only reached 187 mbsf, indicating that there was ~7 m of fill at the bottom. The hole was then displaced with 100 bbl of sepiolite, and the bottom of the drill string was positioned at 80 mbsf. Logging rig-up started at 0830 hr. Despite a limited velocity of only 1.2 kt, the current generated strong vibrations in the short drill string and particular care was taken in tightening the connections while assembling the logging string. The 35-m-long tool string started downhole at 1030 hr, and two passes were made without difficulty. Both passes reached the bottom of the hole at the wireline depth 187 mbsf (351 meters below rig floor), and the bottom

of the drill string was raised by 10 m during logging, allowing data recording in the open hole to 70 mbsf. Logging operations and rig-down were completed by 1430 hr (see Table T10 for a detailed summary of the operations).

Data Quality

The caliper log (Fig. F25A) shows that the borehole wall was generally smooth and that the caliper arm maintained good contact with the formation over the entire logged interval, a requirement for high-quality data recording measurements made on core samples. Logging data are also consistent with physical property measurements from discrete samples. Except for a 30-m interval (between 125 and 155 mbsf) where core measurements were not made because of poor recovery, the MAD density and porosity data available generally agree well with the logs.

Because of the short length of the open hole interval (~117 m), a second pass was made over its entire length to control the quality of the data. Figure F26 compares some of the logs of the two passes (pass 1 = dashed green line and pass 2 = solid red line). The gamma ray values from the second pass are slightly higher than those for the first pass, indicating that the formation was still activated because of the minitron source of the Accelerator Porosity Sonde used during the first pass (see "Downhole Logging," p. 53, in the "Explanatory Notes" chapter). Despite this generally uniform offset, both gamma ray logs agree very well. The density and resistivity curves also display a good repeatability over most of the interval, except between 136 and 150 mbsf, where there is a depth offset of almost a meter in some places between the two passes. All identifiable features are apparent and similar in both passes, but the depth offset indicates that the tool was sticking more strongly to the formation during pass 1 over this interval, generating higher depth values.

Logging Stratigraphy

The general trend of the logs is characterized by a succession of deposition phases of various nature, in particular fining-upward sequences and intervals with a strong biogenic component. The fining-upward sequences indicate changing terrigenous sedimentation controlled by sea level rise or sinking of the basin. Whereas overall the sediments recovered are mostly terrigenous, the relative importance of the types of sedimentation can be seen in the ratio of thorium to uranium concentration (Fig. F25D), which can be used as an indicator of the relative strength of marine and terrestrial deposition (Rider, 1996). High values of this ratio indicate a greater relative input of terrestrial material. Low values indicate sediments of marine origin. Based on variations of this indicator and on individual deposition cycles, we have identified three logging units. We divided these units into logging subunits that correspond to distinct sedimentation phases.

Logging Unit 1 (70–87 mbsf) is characterized by high porosity (~65%) and relatively low resistivity and density. The thorium/urianium ratio increases steadily upward, indicating an increase in terrigenous sediments. The two logging Subunits 1A (70–76 mbsf) and 1B (76–87 mbsf) correspond to two distinct sequences. These sequences are separated by peaks in gamma ray, density, and resistivity that could indicate phosphorite layers generated by reworking of phosphate nodules
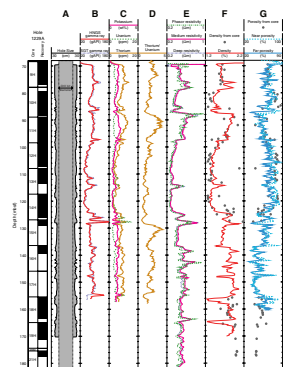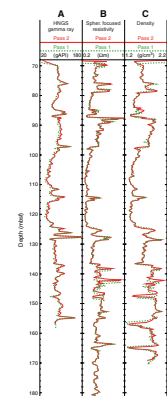
between sedimentation phases. Logging Subunit 1B is a well-defined fining-upward sequence indicating a sea level rise or subsidence of the basin.

The top of logging Unit 2 (87–137 mbsf) is defined by a sharp increase in density and resistivity, which appears to be the top of a very distinct fining-upward sequence corresponding to logging Subunit 2A (87–97 mbsf). This interval is also characterized by high values of thorium and of the thorium/uranium ratio, indicating the almost exclusively terrigenous nature of the sediments. This subunit corresponds to the lower part of lithostratigraphic Subunit IB (see "Description of Lithostratigraphic Units," p. 8, in "Lithostratigraphy"), and its base is defined by a sharp drop in resistivity and density. The base of this subunit corresponds to an erosional surface overlain by shell debris (see "Lithostratigraphy," p. 8). This erosional surface was also recovered at Site 681 during Leg 112 (Shipboard Scientific Party, 1988). Logging Subunit 2B (97–128 mbsf) corresponds to the two upper intervals of lithostratigraphic Subunit IC (see "Description of Lithostratigraphic Units," p. 8, in "Lithostratigraphy"), which display a downhole increase of biogenic sediments, mostly diatom ooze. This downhole increase in biogenic material in the cores corresponds to a steady downhole decrease of the thorium and of the thorium/uranium ratio in this logging subunit. The uphole increase in these properties indicates the progressive shift in time from marine sedimentation in the lower half of logging Subunit 2B to a mostly terrigenous, fining-upward sedimentation. At the base of logging Subunit 2B, peaks in gamma ray, uranium, density, and resistivity and the presence of phosphate nodules in the core (see "Lithostratigraphy," p. 8) indicate reworked phosphorite layers. Logging Subunit 2C (128–137 mbsf) is a fining-upward sequence similar in character to logging Subunit 2A, with high thorium/uranium values and slight upcore increase in density and resistivity. It corresponds to the lower portion of lithostratigraphic Subunit IC (see "Description of Lithostratigraphic Units," p. 8, in "Lithostratigraphy").

Logging Unit 3 (137–185 mbsf) corresponds to lithologic Unit II (see "Description of Lithostratigraphic Units," p. 8, in "Lithostratigraphy"). This lithologic unit is characterized by well-sorted and rounded sand and silt with variable clay content. The top of the logging unit is defined by an increase in density and resistivity and by a drop in porosity. This logging unit is characterized by significant fluctuations in most logs, corresponding to the alternation of sand and silt as noted in the "Site 1229 Core Descriptions." Logging Subunit 3B (155–185 mbsf) was logged fully only by the resistivity sonde, but it is marked by a slight decrease in resistivity, an apparent increase in porosity, and two distinct 2-m-thick intervals with lower density (at 156 and 165 mbsf, respectively).

Temperature Log

Temperatures were recorded with the Lamont-Doherty Earth Observatory (LDEO) Temperature/Acceleration/Pressure (TAP) memory tool attached at the bottom of the triple combo tool string. Because only a few hours had passed since the end of drilling operations and hole conditioning, the borehole temperature is not representative of the actual equilibrium temperature distribution of the formation. In the case of Hole 1229A, the surface seawater and the sepiolite mud pumped during and after drilling generated borehole fluid temperatures higher than the formation temperatures. Discrete measurements made with the DVTP

indicate a maximum formation temperature of 19.2°C at 164.8 mbsf (see "In Situ Temperature Measurements," p. 27, in "Downhole Tools") and a temperature of 19.9°C was recorded at 187 mbsf at Site 681 (Shipboard Scientific Party, 1988), whereas the maximum temperature recorded by the TAP tool at 186 mbsf is 25.6°C (see Fig. F27). The generally lower temperatures during the second pass indicate a progressive return to equilibrium. The variations measured at 70 and 80 mbsf while logging downhole correspond to the tool exiting the drill string. The drops in temperature on the uphole run at 100 and 150 mbsf are likely related to operations, and the smoother second pass indicates some recovery between the two passes. Surprisingly, these features were not recorded on the downhole run and are difficult to explain because the logging speed was uniform during the two passes and no stop was made. The consistently small difference between the two passes in the two directions between 80 and 100 mbsf is also unexpected and will need further explanation.

F27. Hole 1229A temperature log, p. 63.
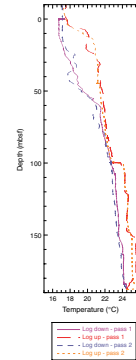
REFERENCES

Berggren, W.A., Kent, D.V., Swisher, C.C., and Aubry, M.P., 1995. A revised Cenozoic geochronology and chronostratigraphy. *In* Berggren, Kent, Aubry, and Hardenbol, J., (Eds.), 1995. *Geochronology, Time Scales and Global Stratigraphic Correlation.* Spec. Pub.—SEPM, 59:129–212.

Cragg, B.A., Parkes, R.J., Fry, J.C., Herbert, R.A., Wimpenny, J.W.T., and Getliff, J.M., 1990. Bacterial biomass and activity profiles within deep sediment layers. *In* Suess, E., von Huene, R., et al., *Proc. ODP, Sci. Results,* 112: College Station, TX (Ocean Drilling Program), 607–619.

Merrill, D.L., Ohnstad, T., and McCabe, R., 1990. Magnetic susceptibility measurements of Leg 112 cores. *In* Suess, E., von Huene, R., et al., *Proc. ODP, Sci. Results,* 112: College Station, TX (Ocean Drilling Program), 677–683.

Parkes, R.J., Cragg, B.A., Bale, S.J., Getliff, J.M., Goodman, K., Rochelle, P.A., Fry, J.C., Weightman, A.J., and Harvey, S.M., 1994. A deep bacterial biosphere in Pacific Ocean sediments. *Nature,* 371:410–413.

Rider, M., 1996. *The Geological Interpretation of Well Logs* (2nd ed.): Houston (Gulf Publishing Co.).

Shipboard Scientific Party, 1988. Site 681. *In* Suess, E., von Huene, R., et al., *Proc. ODP, Init. Repts.,* 112: College Station, TX (Ocean Drilling Program), 305–362.

Smith, R.L., Huyer, A., Godfrey, J.S., and Church, J.A., 1991. The Leeuwin Current off Western Australia, 1986–1987. *J. Phys. Oceanog.,* 21:323–345.

Smith, D.C., Spivack, A.J., Fisk, M.R., Haveman, S.A., Staudigel, H., and ODP Leg 185 Shipboard Scientific Party, 2000. Methods for quantifying potential microbial contamination during deep ocean coring. *ODP Tech. Note,* 28 [Online]. Available from the World Wide Web: <http://www-odp.tamu.edu/publications/tnotes/tn28/INDEX.HTM>. [2002-03-30]

Suess, E., von Huene, R., et al., 1988. *Proc. ODP, Init. Repts.,* 112: College Station, TX (Ocean Drilling Program).

Figure F1. Lithostratigraphic summary for Site 1229. Color reflectance profile is from Hole 1229A. TD = total depth.
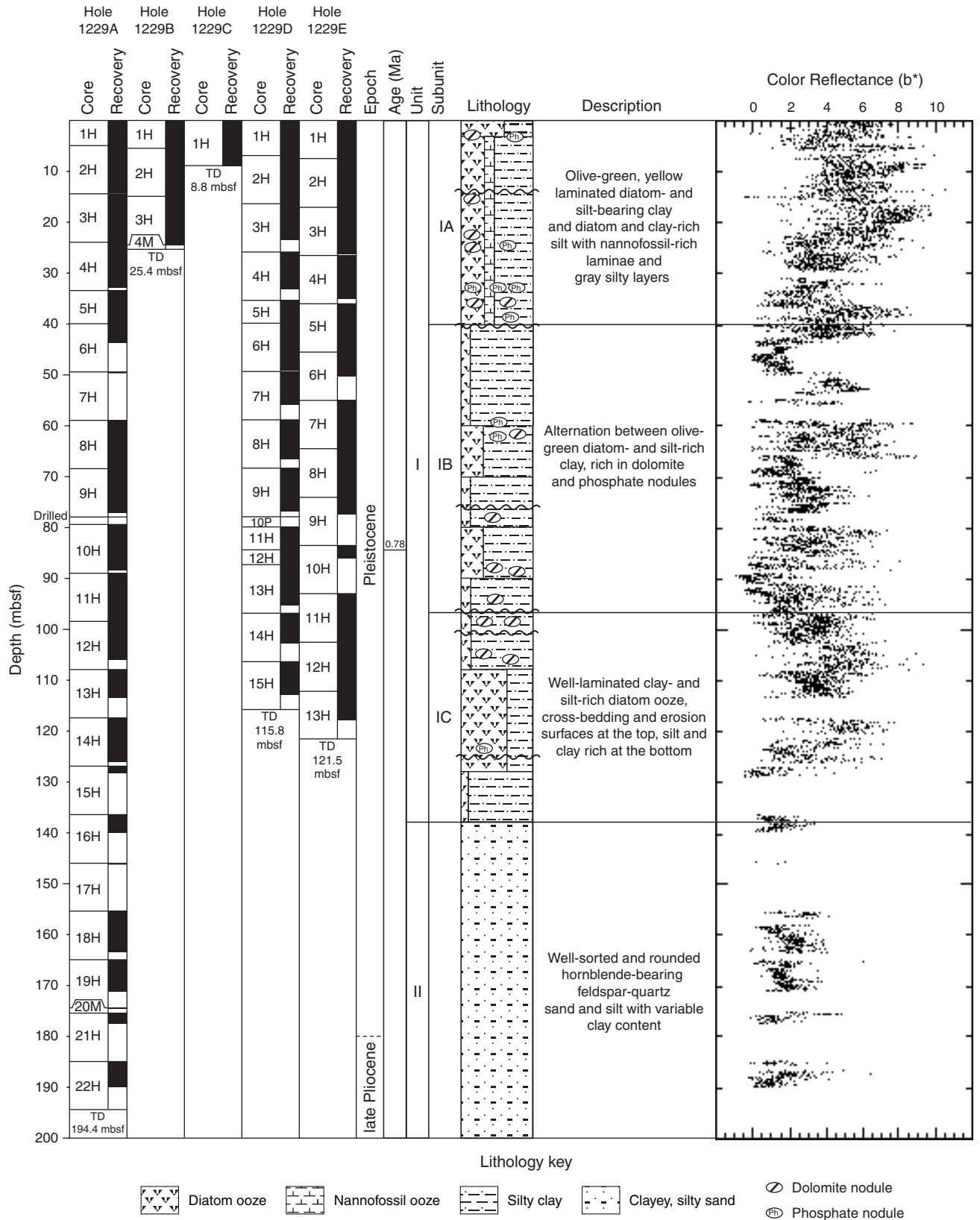
Figure F2. Lithostratigraphic summary for Site 1229 plotted together with natural gamma radiation (NGR) measured by wireline tool and multisensor track (MST) from Hole 1229A. TD = total depth.
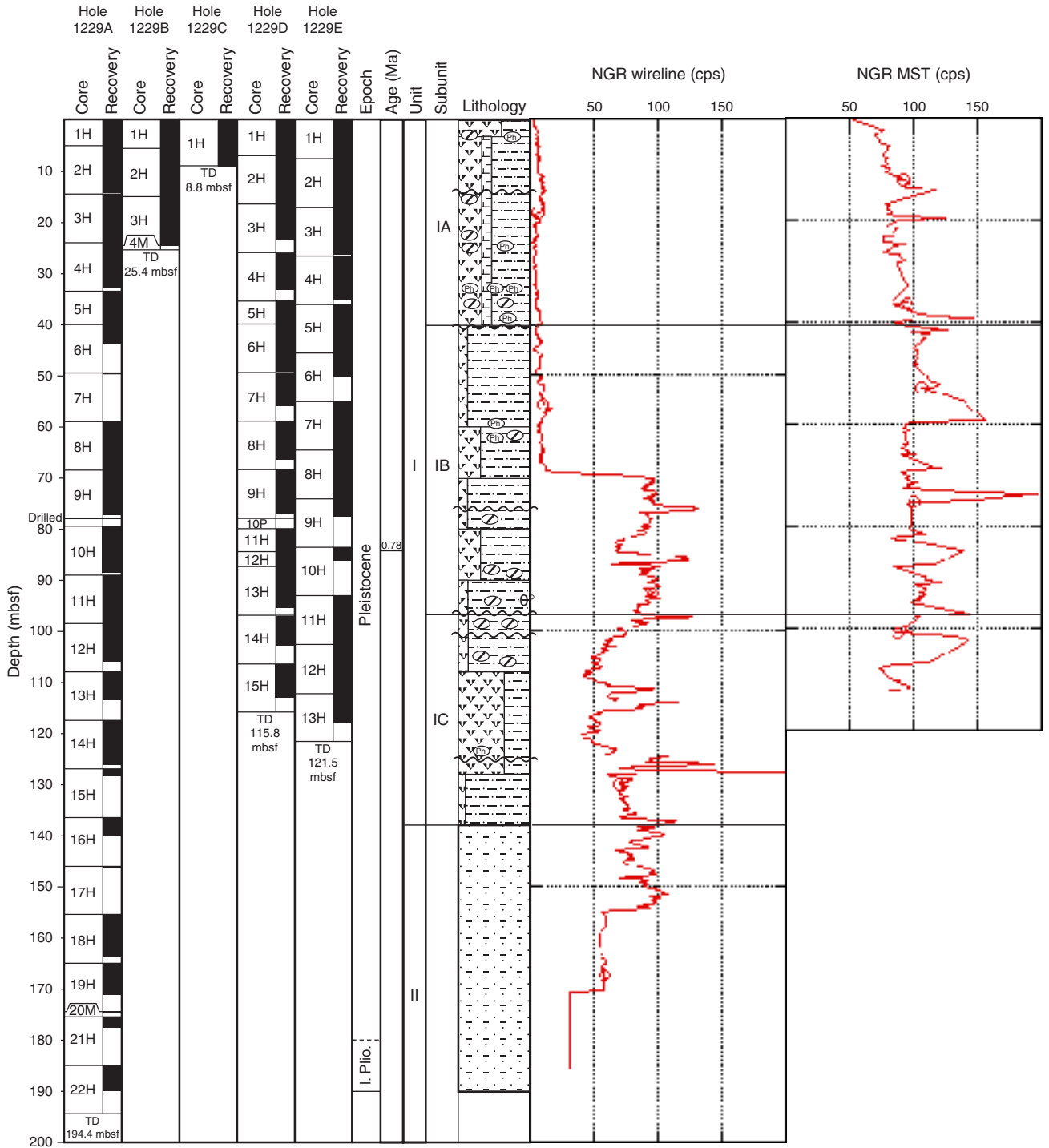
Figure F3. Close-up photographs. **A.** Cross-bedding in diatom-rich silt of Subunit IA. **B.** Dolomite nodule with preserved sedimentary layering surrounded by pale yellow altered sediment. Smear slide analysis and X-ray diffractometry revealed almost pure dolomitic composition for disseminated rhombs in the yellow altered parts (XRD Sample 201-1229A-1H-3, 84–85 cm). These features also seem to be concentrated in yellow semilithified diatom ooze laminae. (Continued on next two pages.)
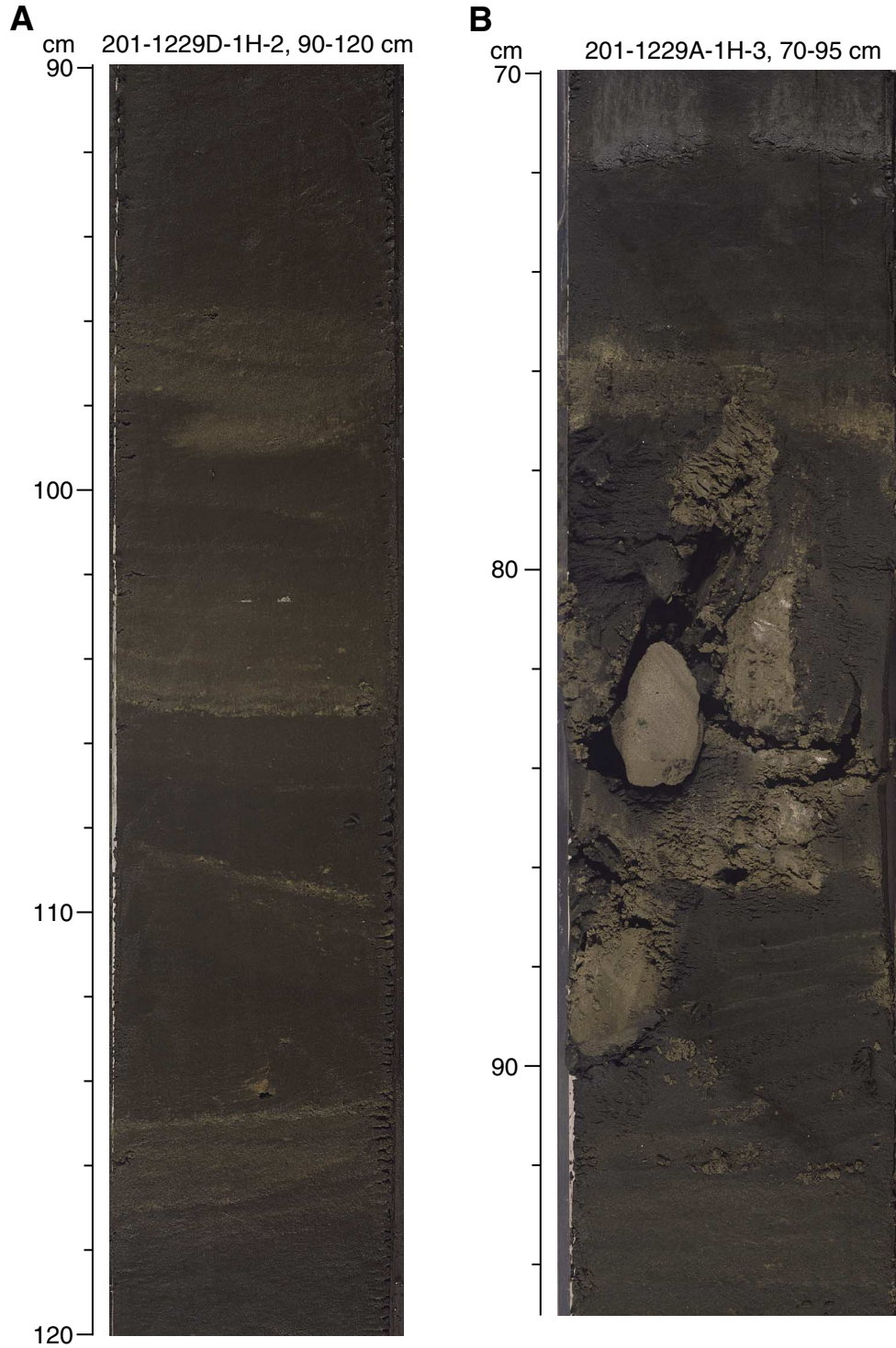
Figure F3 (continued). C. Fluid escape structure filled with quartz sand in Subunit IB. White and pale yellow mineralizations are of dolomitic composition, as shown by X-ray diffractometry. **D.** Boundary between Subunits IB and IC. Onset of gray diatom-poor silt and clay sediments over olive-green diatom-rich silty clay. The transition is marked by several erosional surfaces, each covered by a layer of shell debris. (Continued on next page.)
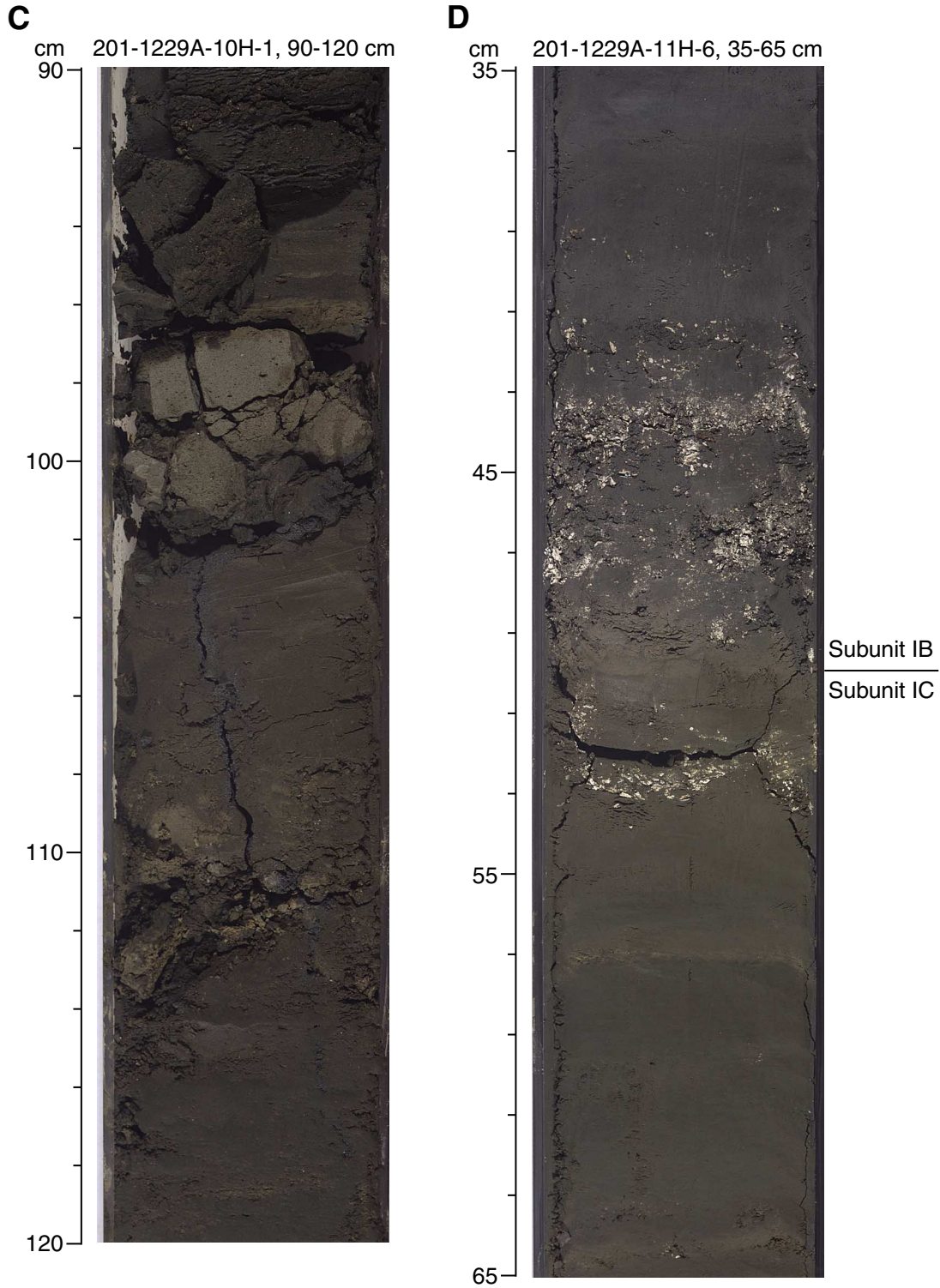
Figure F3 (continued). E. Phosphatic hardground covering a gray clay layer in Subunit IC. The surface of the clay layer is affected by burrowing.

E

cm   201-1229A-14H-4, 125–140 cm

Silt

Phosphate
hardground

Burrow

Clay

Silt
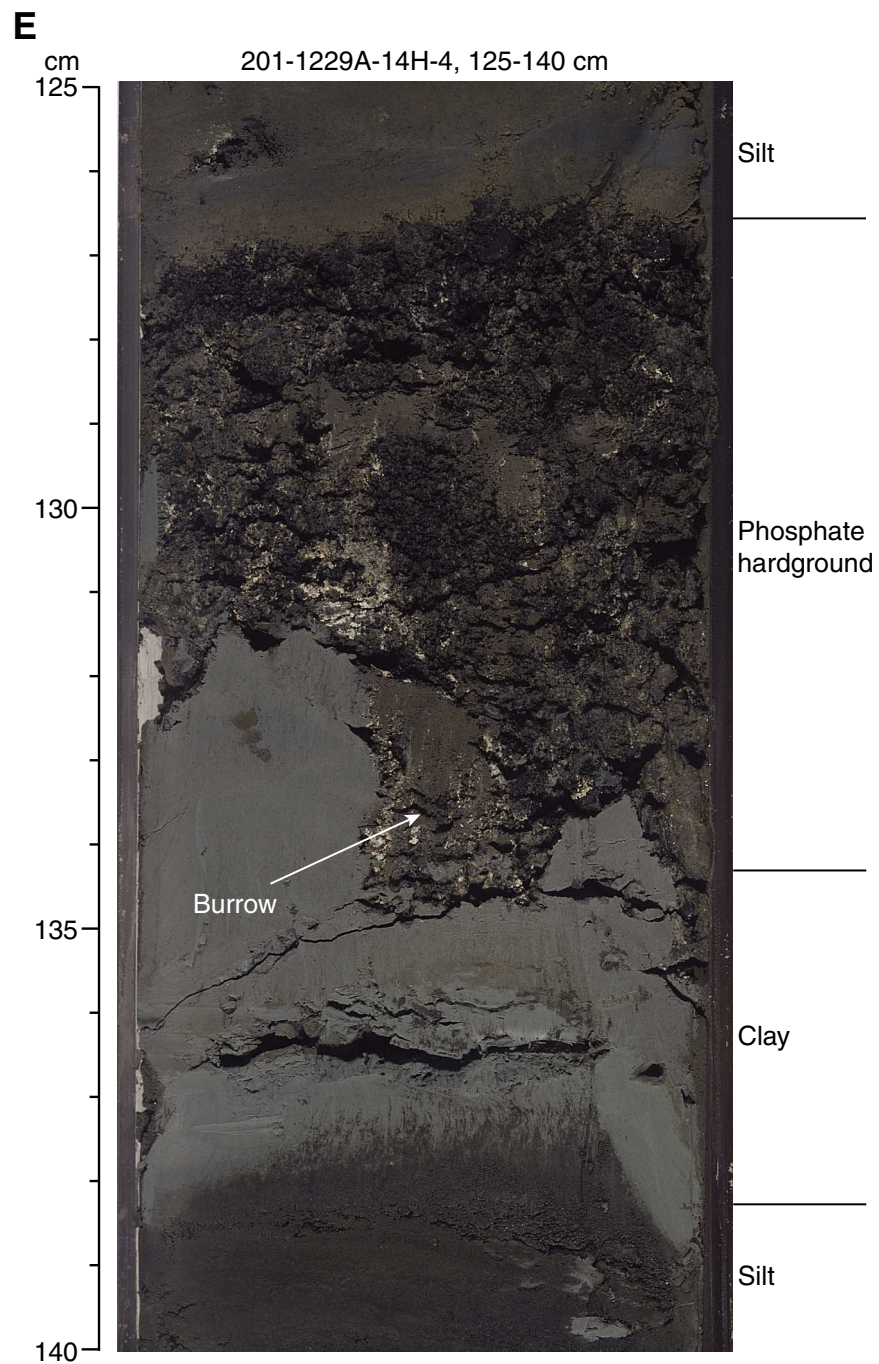
Figure F4. Diffractogram of dolomite precipitated near a fluid escape structure in Subunit IB. The measured peak shows an offset of 0.191°2θ relative to the peak of ordered dolomite indicating that the interval is a calcium-rich dolomite (Section 201-1229A-10H-1).
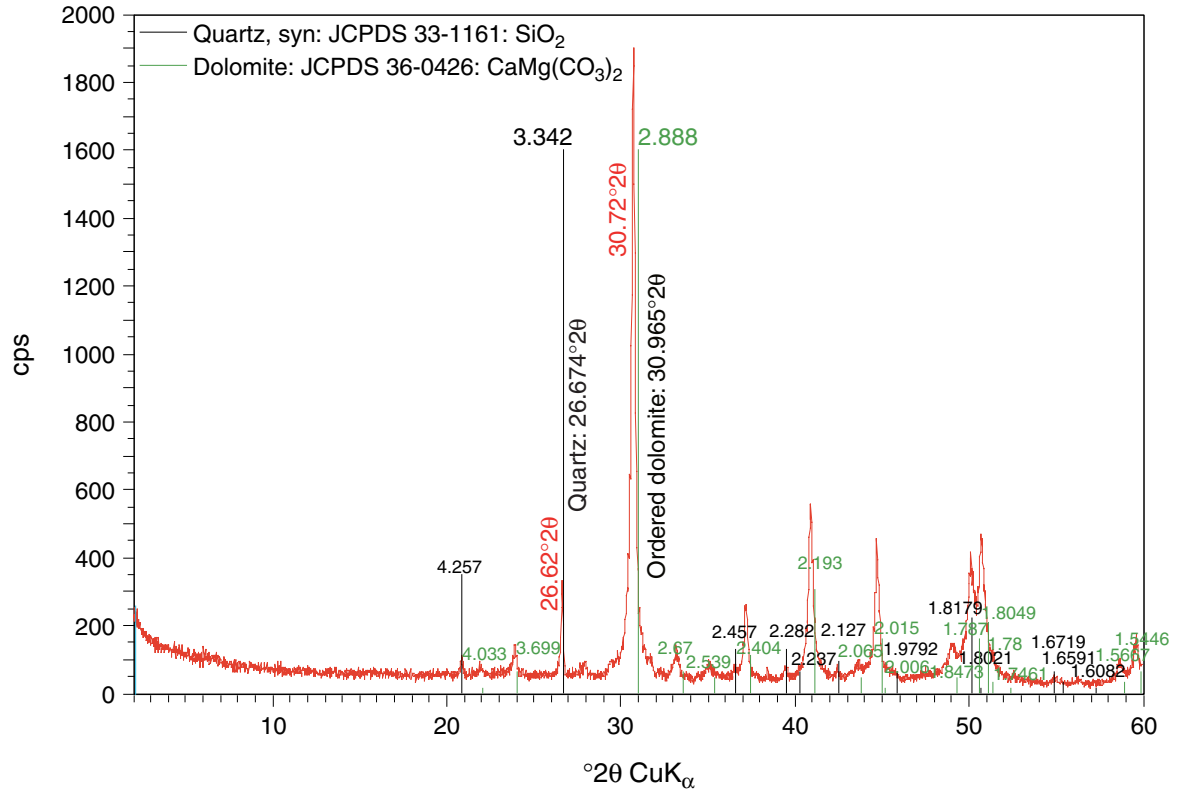
Figure F5. Concentrations of various dissolved species in interstitial waters from Site 1229. (**A**) alkalinity, (**B**) dissolved in organic carbon (DIC), (**C**) sulfate, (**D**) chloride, (**E**) total sulfide, (**F**) barium, and (**G**) manganese. (Continued on next two pages.)
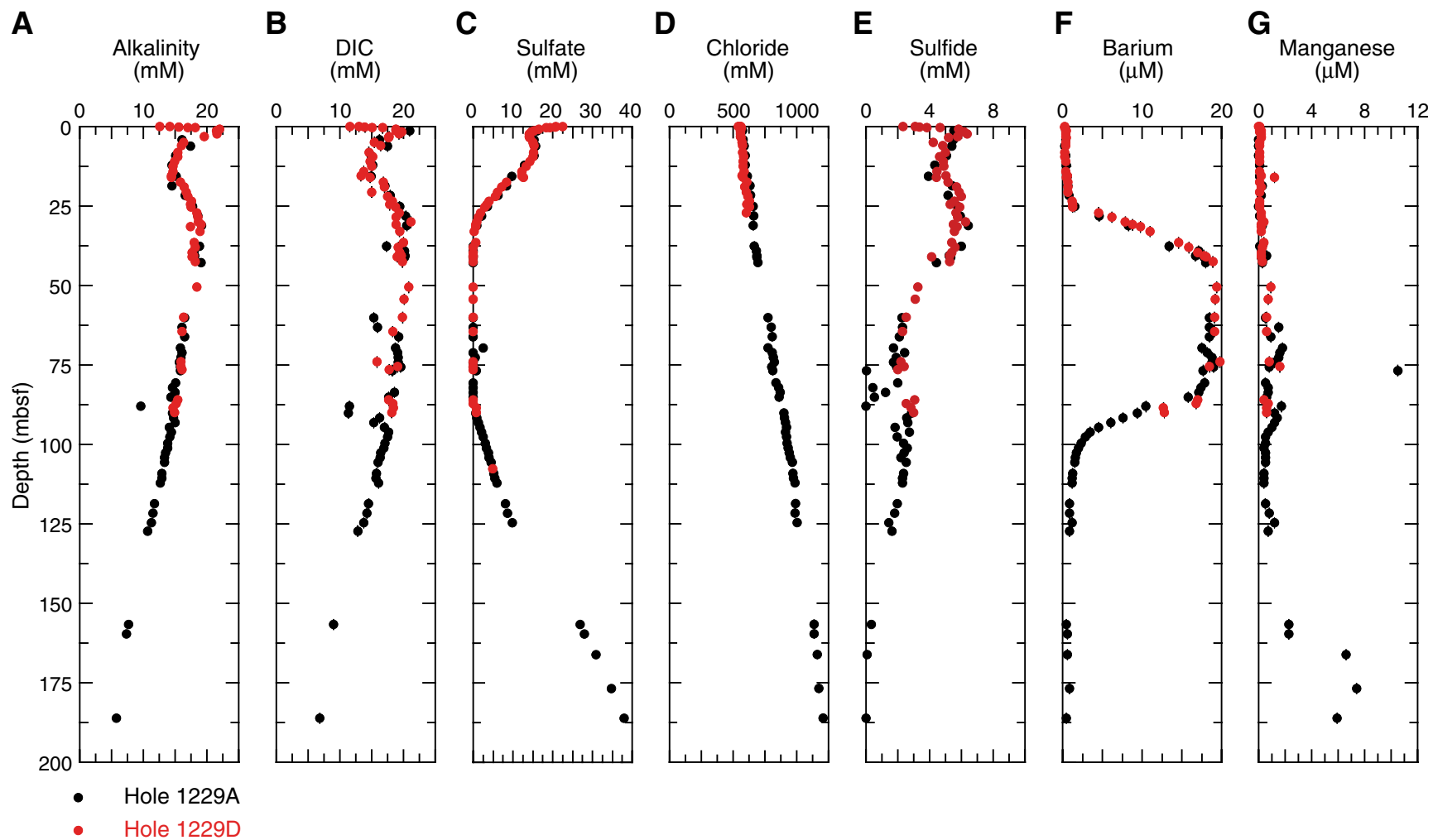
Figure F5 (continued). (**H**) iron, (**I**) strontium, (**J**) lithium, (**K**) ammonium, (**L**) phosphate, and (**M**) silica. (Continued on next page.)

Figure F5 (continued). (**N**) acetate, (**O**) formate, (**P**) methane, (**Q**) ethane, (**R**) propane, and (**S**) hydrogen.

Figure F6. Graphical representation of subsampling and analysis program for the MBIO core sections from Hole 1229A. The sequence of subsections runs from the top of the core (right) towards the bottom (left). DNA = deoxyribonucleic acid, ATP = adenosine triphosphate. WRC = whole-round core. * = big piece of dolomite at 78–84 cm. ** = Dolomite samples from 64 to 79 cm. See Table T2, p. 82, in the "Explanatory Notes" chapter for explanation of sampling codes.

Column groups: **N₂-flushed cutting rig** (FISHTS through CHNSF) and **ODP cutter** (BIOMHIN through ATPS).

Interval (cm): FISHTS/H3S/ABTP/ABTP/PO4B = 6; SRRF/H2S/CNSS/CHNSF = 6; BIOMHIN/BIOMHORS = 10; DIFFF/CELLS/FESF/SRRWF/AMO/PRIEUR = 5; HTEW = 7; SLUR = 7; FISHWR2/FISHWR/DNAM/DNAF/DNAT/DNAN/DNAS/DNAODP = 5; ATPS = 10.

Curators Code	FISHTS	H3S	ABTP	ABTP	PO4B	SRRF	H2S	CNSS	CHNSF	BIOMHIN	BIOMHORS	DIFFF	CELLS	FESF	SRRWF	AMO	PRIEUR	HTEW	HTEW	SLUR	SLUR	FISHWR2	FISHWR	DNAM	DNAF	DNAT	DNAN	DNAS	DNAODP	ATPS	Sediment Depth (mbsf)
Sample Type	2 Syr	4 Syr	4 Syr	8 Syr	1-cm slice	4 Syr	4 Syr	1-cm slice	1-cm slice	WRC	WRC	WRC	WRC	WRC	WRC	WRC	WRC	60-mL + 3 x 5-mL syr	60-mL syr	60-mL + 2 x 5-mL syr	60-mL + 3 x 5-mL syr	WRC	WRC	WRC	WRC	WRC	WRC	WRC	WRC	WRC	
Package Type	Poly-bag	Al-bag	Anaer. Jar	Anaer. Jar	Poly-bag	Al-Bag	Poly-bag	Poly-bag	Al-bag	Poly-bag	Poly-bag	Al-bag	Poly-bag	Al-bag	Al-bag	Al-bag	Al-bag	Anaer. Jar	Anaer. Jar	Al-bag	Al-bag	Al-bag	Poly-bag	Poly-bag	Poly-bag	Poly-bag	Poly-bag	Poly-bag	Poly-bag	Poly-bag	
Package Atmosphere		N₂	N₂	N₂		N₂	N₂		Vac pack					Vac pack		Vac pack	N₂ An.cult	N₂ An.cult	N₂	N₂	N₂	N₂	N₂								
Temperature Destination	+4°C	+4°C Radvan	+4°C Radvan	+4°C Radvan	–20°C	+4°C Radvan	+4°C	+4°C	+4°C	–80°C	–80°C	+4°C	–80°C	–20°C	+4°C	+4°C	+4°C	+4°C	+4°C	on ice	on ice	+4°C	–80°C	–80°C	–80°C	–80°C	–80°C	–80°C	–80°C	–80°C	
Core Section																															top
2H 2	1	1	1	1	1	1	1	1	1	1	1	1	1	1	–	1	1	1	1	1	1	1	1	1	1	1	1	1	1	1	6.4
2H 5	1	1	1	1	1	1	1	1	1	1	–	–	–	1	–	–	1	–	–	–	–	–	1	–	–	1	1	1	1	1	10.9
3H 2	1	1	1	1	1	1	1	1	1	1	–	–	–	1	–	–	1	–	–	–	–	1	1	1	–	1	1	1	1	1	15.9
3H 5	1	1	1	1	1	1	1	1	1	–	–	–	–	1	–	–	–	–	–	–	–	–	1	–	–	1	1	1	1	1	20.4
4H 2*	1	1	1	1	1	1	1	1	1	1	–	–	–	1	–	1	–	–	–	–	–	1	1	–	–	1	1	1	1	1	25.4
4H 5	–	1	1	1	1	1	1	1	1	–	1	–	–	1	–	–	1	–	–	1	1	–	1	1	1	–	1	1	1	1	29.9
5H 5	1	1	1	1	1	1	1	1	1	1	–	–	–	1	–	–	1	–	–	–	–	1	1	–	1	1	1	1	1	1	39.4
6H 2	1	–	1	1	1	1	1	1	1	1	1	1	–	1	–	1	–	1	1	1	1	1	1	1	1	1	1	1	1	1	41.4
8H 2	1	1	1	1	1	1	1	1	1	1	–	–	–	1	–	1	–	–	–	–	–	1	1	–	–	1	1	1	1	1	60.4
8H 5	–	–	1	1	1	1	1	1	1	–	1	–	–	1	–	–	–	–	–	–	–	–	1	–	–	1	1	1	1	1	64.9
9H 2**	1	1	1	1	1	1	1	1	1	1	–	–	–	1	–	1	–	–	–	1	1	1	1	–	–	1	1	1	1	1	69.9
9H 5	–	–	1	1	1	1	1	1	1	–	–	–	–	1	–	–	–	–	–	–	–	–	1	–	–	1	1	1	1	1	74.4
10H 2	1	–	1	1	1	1	1	1	1	1	1	–	–	1	–	–	–	–	–	–	–	1	1	–	1	1	1	1	1	1	80.9
10H 4	–	–	1	1	1	1	1	1	1	–	–	–	–	1	–	–	–	–	–	–	–	1	1	–	–	1	1	1	1	1	83.9
11H 2	1	1	1	1	1	1	1	1	1	1	–	1	–	1	1	1	–	1	1	1	1	1	1	–	1	1	1	1	1	1	90.4
11H 5	–	–	–	–	–	1	1	1	1	–	–	–	–	1	–	–	–	–	–	–	–	–	1	–	–	1	1	1	1	1	94.9
12H 3	1	1	1	1	1	1	1	1	1	1	1	–	–	1	–	1	1	–	–	–	–	1	1	1	1	1	1	1	1	1	101.4
13H 3	1	–	–	–	–	1	1	1	1	–	–	–	–	1	–	–	–	–	–	–	–	–	1	–	–	1	1	1	1	–	110.9
14H 3	1	1	1	1	1	1	1	1	1	1	1	–	–	1	–	1	–	–	–	–	–	1	1	1	1	1	1	1	1	1	120.4
18H 2	1	1	1	1	1	1	1	1	1	1	1	–	–	1	–	1	–	1	–	–	–	1	1	–	1	1	1	1	1	1	156.9
22H 1	1	–	1	1	1	1	1	1	1	1	–	–	–	1	–	–	–	–	–	–	–	–	1	–	–	1	1	1	1	1	184.9
22H 2	–	–	–	–	–	–	–	–	–	–	–	–	–	–	–	–	–	1	1	1	1	–	–	–	–	–	–	–	–	–	186.4
TOTAL	16	14	19	19	19	21	20	21	20	13	9	3	1	21	1	9	6	4	3	6	6	12	21	7	8	21	21	21	21	20	

Column descriptions (top headers):
- FISHTS: Fluorescent in situ hybridization (FISH)/Hydrogen turnover
- H3S: (Activity measurements)
- ABTP / ABTP / PO4B: Activity measurements: methanogenesis, thymidine incorporation, tritiated hydrogen turnover, ³²O phosphate turnover
- SRRF / H2S / CNSS / CHNSF: Sulfate reduction activity; hydrogen concentration; CHNS geochemistry; magnetic bacterial particles
- BIOMHIN / BIOMHORS: Biomarkers
- DIFFF: Diffusion experiments
- CELLS: Cell separations
- FESF: Fe/Mn/S solid-phase concentrations and stable isotopes
- SRRWF: Sulfate Reduction Pressure-Temperature experiments
- AMO: Anaerobic oxidation of methane
- PRIEUR: Enrichments prieur
- HTEW: Enrichments for thermophiles
- SLUR: General enrichment slurry
- FISHWR2 / FISHWR: Fluorescent in situ hybridization (FISH)
- DNAM / DNAF / DNAT / DNAN / DNAS: DNA
- DNAODP: DNA-ODP archive
- ATPS: ATP-DNA

Top of Section / Sediment Depth (mbsf)

Figure F7. Graphical representation of subsampling and analysis program for the MBIO core sections from Hole 1229D. The sequence of subsectioning runs from the top of the core (right) towards the bottom (left). DNA = deoxyribonucleic acid, ATP = adenosine triphosphate. WRC = whole-round core. See Table T2, p. 82, in the "Explanatory Notes" chapter for explanation of sampling codes.

Hole 1229D	N₂-flushed cutting rig									ODP cutter																						Top of Section
Interval (cm)	6	6		6			6			10	10	5	5	5	5	5	5	7	7	7	7	5	5	6	5	5	5	5	5	5	10	
CURATORS CODE	FISHTS	H3S	ABTP	ABTP	PO4B	SRRF	H2S	CNSS	CHNSF	BIOMHIN	BIOMHORS	DIFFF	CELLS	FESF	SRRWF	AMO	PRIEUR	HTEW	HTEW	SLUR	SLUR	FISHWR2	FISHWR	PLFAP	DNAM	DNAF	DNAT	DNAN	DNAS	DNAODP	ATPS	
Sample Type	2 Syr	4 Syr	4 Syr	8 Syr	1-cm slice	4 Syr	4 Syr	1-cm slice	1-cm slice	WRC	WRC	WRC	WRC	WRC	WRC	WRC	WRC	60-mL + 3 x 5-mL syr	60-mL syr	60-mL + 2 x 5-mL syr	60-mL + 3 x 5-mL syr	WRC	WRC	WRC	WRC	WRC	WRC	WRC	WRC	WRC	WRC	
Package Type	Poly-bag	Al-bag	Anaer. Jar	Anaer. Jar	Poly-bag	Al-Bag	Poly-bag	Poly-wog	Al-bag	Poly-bag	Poly-bag	Al-bag	Poly-bag	Al-bag	Al-bag	Al-bag	Al-bag	Anaer. Jar	Anaer. Jar	Al-bag	Al-bag	Al-bag	Poly-bag	Al-bag	Poly-bag	Poly-bag	Poly-bag	Poly-bag	Poly-bag	Poly-bag	Poly-bag	
Package Atmosphere		N₂	N₂	N₂		N₂	N₂		Vac pack			Vac pack		Vac pack	N₂ An.cult	N₂ An.cult	N₂	N₂	N₂	N₂	N₂	N₂		N₂								
Temperature Destination	+4°C	+4°C Radvan	+4°C Radvan	+4°C Radvan	-20°C	+4°C Radvan	+4°C	+4°C	+4°C	-80°C	-80°C	+4°C	-80°C	-20°C	+4°C	+4°C	+4°C	+4°C	+4°C	on ice	on ice	+4°C	-80°C	+4°C	-80°C	-80°C	-80°C	-80°C	-80°C	-80°C	-80°C	
Core / Section																																Sediment Depth (mbsf)
1H 1	1	1	1	1	1	1	1	1	1	1	1	-	1	1	-	-	-	1	1	1	1	1	1	-	-	-	1	1	1	1	1	top / 0.0
1H 2	-	-	-	-	-	1	1	1	1	-	-	1	1	1	-	-	-	-	-	-	-	-	-	-	-	-	1	-	-	-	-	2.0
1H 3	1	1	1	1	1	1	1	1	1	1	-	-	-	1	-	-	-	-	-	--	-	1	1	-	-	-	1	1	1	1	1	3.5
1H 4	-	-	-	-	-	-	-	-	-	-	-	-	-	-	-	-	-	-	-	-	-	1	1	-	-	-	1	1	1	1	1	5.0
1H 5	1	1	1	1	1	1	1	1	1	1	-	-	-	1	-	-	-	-	-	-	-	-	-	-	-	-	-	-	-	-	-	6.0
2H 5	1	-	-	-	-	-	-	-	-	1	-	-	-	-	-	-	-	-	-	-	-	1	-	1	-	-	1	-	-	-	-	12.8
4H 3	1	-	-	-	1	-	1	-	-	1	-	-	-	1	-	1	-	-	-	-	-	1	1	-	-	-	1	1	1	1	1	28.8
4H 4	1	-	-	-	-	-	1	1	1	1	1	-	-	1	-	-	1	-	-	-	-	1	1	-	1	1	1	1	1	1	1	30.3
4H 5	1	-	-	-	-	-	1	1	1	1	-	-	-	1	-	1	-	-	-	-	-	1	1	-	-	-	1	1	1	1	1	31.8
6H 1	-	-	-	-	-	-	-	-	-	-	-	-	-	-	-	-	-	-	-	-	-	-	-	1	-	-	1	1	1	1	-	39.8
7H 1	-	-	1	1	1	1	1	1	1	1	1	1	-	1	-	-	-	-	-	-	-	1	1	1	-	-	1	1	1	1	1	49.3
7H 4	-	-	1	1	1	1	1	1	1	1	1	-	-	1	-	-	-	-	-	-	-	1	1	-	1	-	1	1	1	1	1	53.8
9H 4	-	-	-	-	-	-	-	-	-	-	-	-	-	-	-	1	-	-	-	-	-	-	-	1	-	-	-	-	-	-	1	72.8
12H 2	1	1	1	1	1	1	1	1	1	1	1	-	-	1	-	-	1	-	-	-	-	1	1	1	1	1	1	1	1	1	1	84.8
12H 3	1	-	-	-	-	1	1	-	-	1	1	-	-	-	-	-	1	-	-	-	-	1	1	1	1	1	1	1	1	1	1	86.3
13H 1	-	-	-	-	-	-	1	-	-	-	-	-	-	-	-	-	-	-	-	-	-	-	-	1	1	1	1	1	1	-	1	87.3
13H 2	-	-	-	-	-	1	1	-	-	1	1	-	-	-	-	-	-	-	-	-	-	1	1	-	-	-	1	-	-	-	-	88.8
15H 3	-	-	-	-	-	-	-	-	-	-	-	-	-	-	-	-	-	1	-	-	-	-	-	-	-	-	1	1	1	1	-	109.3
TOTAL	11	4	6	6	6	7	12	9	9	11	7	2	2	10	0	6	2	2	1	1	1	12	11	7	5	4	15	13	13	13	11	

Figure F8. Total prokaryotic cells (solid circles) and the percentage of dividing cells (open circles) with depth at Site 1229. Dividing cell percentages become increasingly unreliable as total cell counts decrease below 1×10^7 cm^{-3} as within-sample variability rises due to the low number of cells counted. Vertical dashed line on the left represents the detection limit at 5.8×10^5 cells/cm^3.
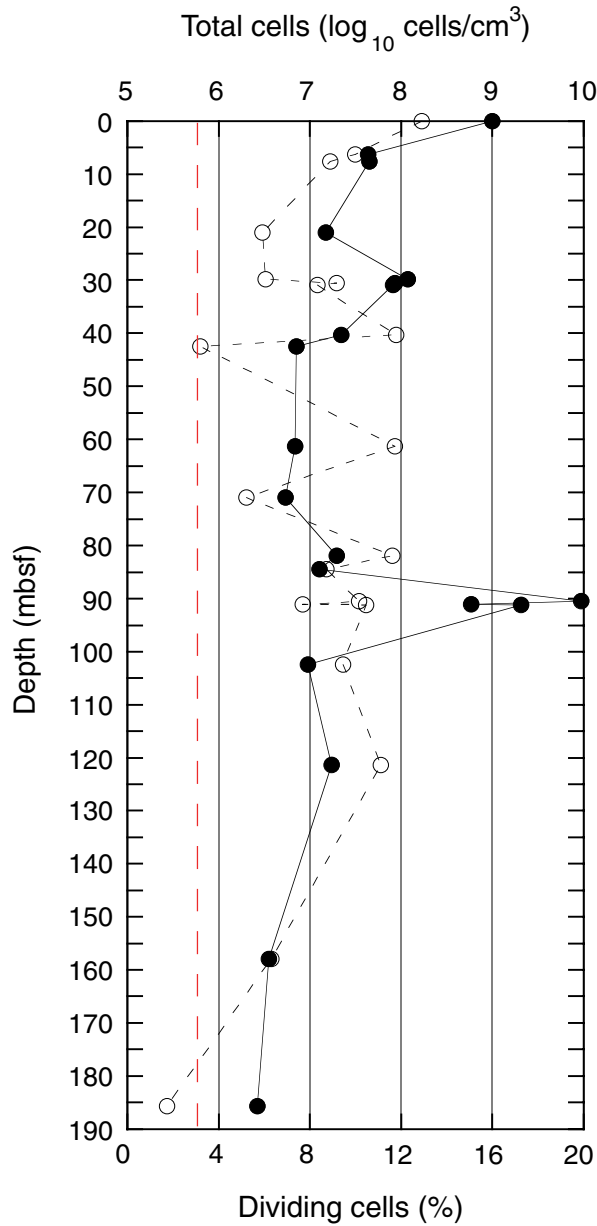
Figure F9. Profile of total prokaryotic cells at Site 1229. The heavy dashed line is a regression line derived from previous ODP legs, and updated from Parkes et al., 1994 ($\log_{10}$ cells = 8.03 − 0.66 $\log_{10}$ depth). Lighter dashed lines represent the ±2-σ envelopes of data based on censused data from previous ODP legs.
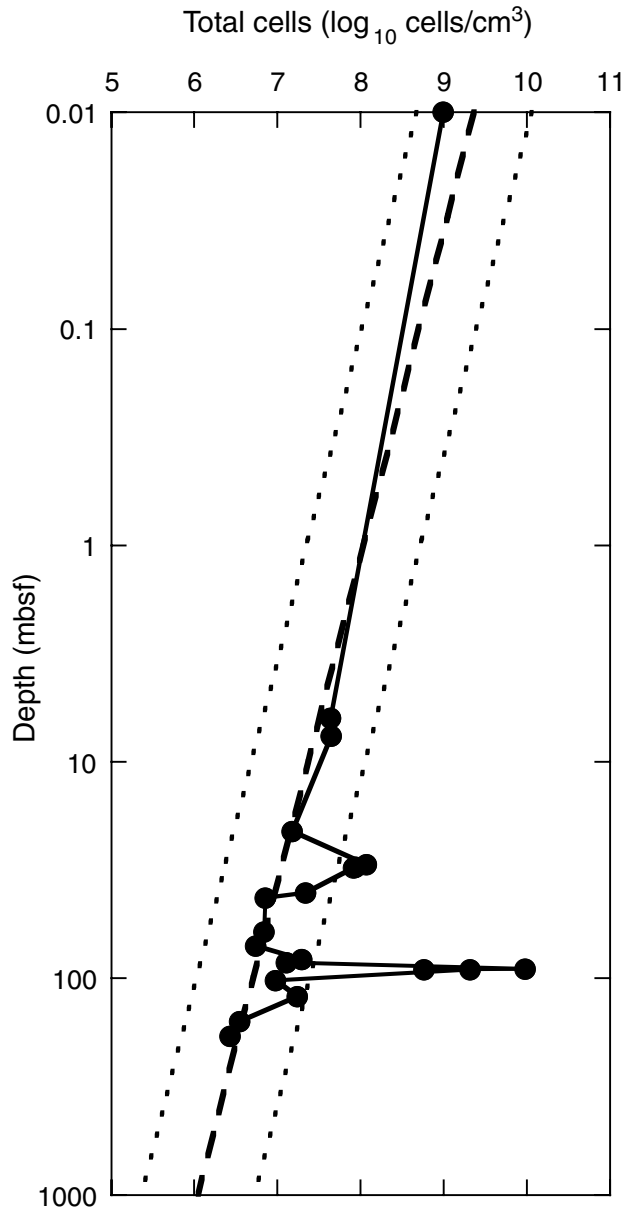
Figure F10. Comparison of magnetic susceptibility data. **A.** MST for Site 1229. **B.** Postcruise data from Hole 681A (Merrill et al., 1990).
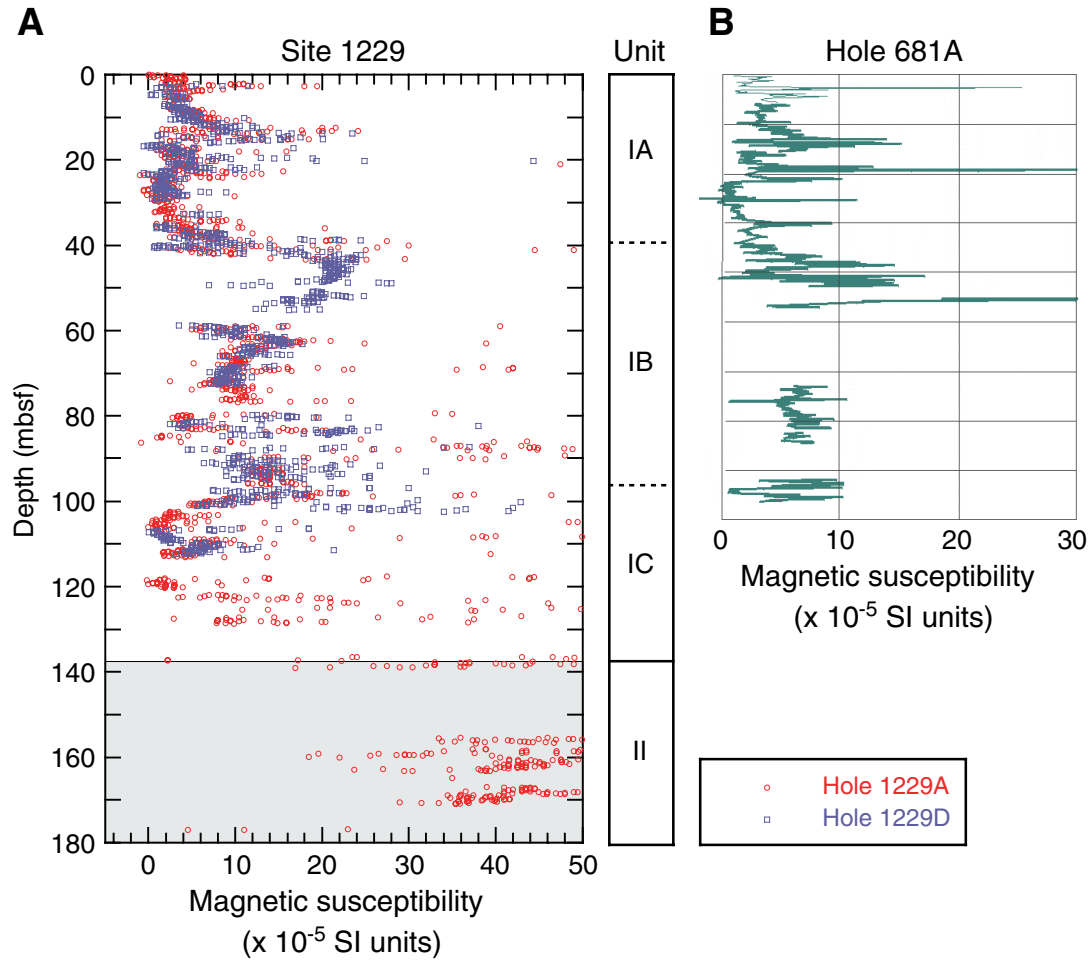
Figure F11. Magnetic intensity in Hole 1229A. Open squares = NRM intensity, solid squares = intensity after 20-mT AF demagnetization.
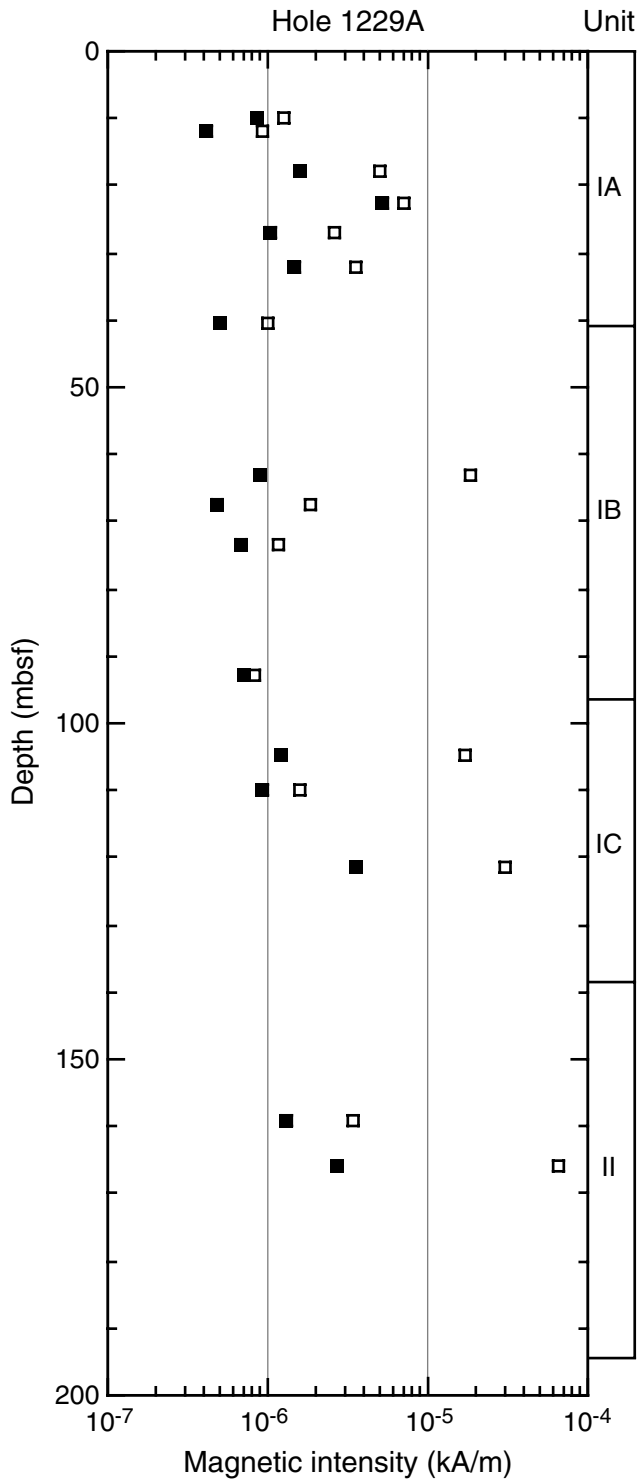
Figure F12. Principal component analysis of natural remanent magnetization (NRM) of Sample 201-1229A-4H-6, 70–72 cm, including equal area projection of directions of magnetization during demagnetization, intensity of magnetization plotted vs. demagnetization, and vector component diagrams showing projection of magnetic vector's endpoints on horizontal and vertical planes. Number reflect demagnetization steps. Dashed line shows a 5- to 30-mT fitting direction.

Sample 201-1229A-4H-6, 70-72 cm

Equal Area projection
□ Upper hemisphere
■ Lower hemisphere

Inclination = -22.0°
Declination = 61.5°

J_{max} = 3.60e-6

■ Horizontal
□ Vertical
◉ ◉ Initial point (NRM)
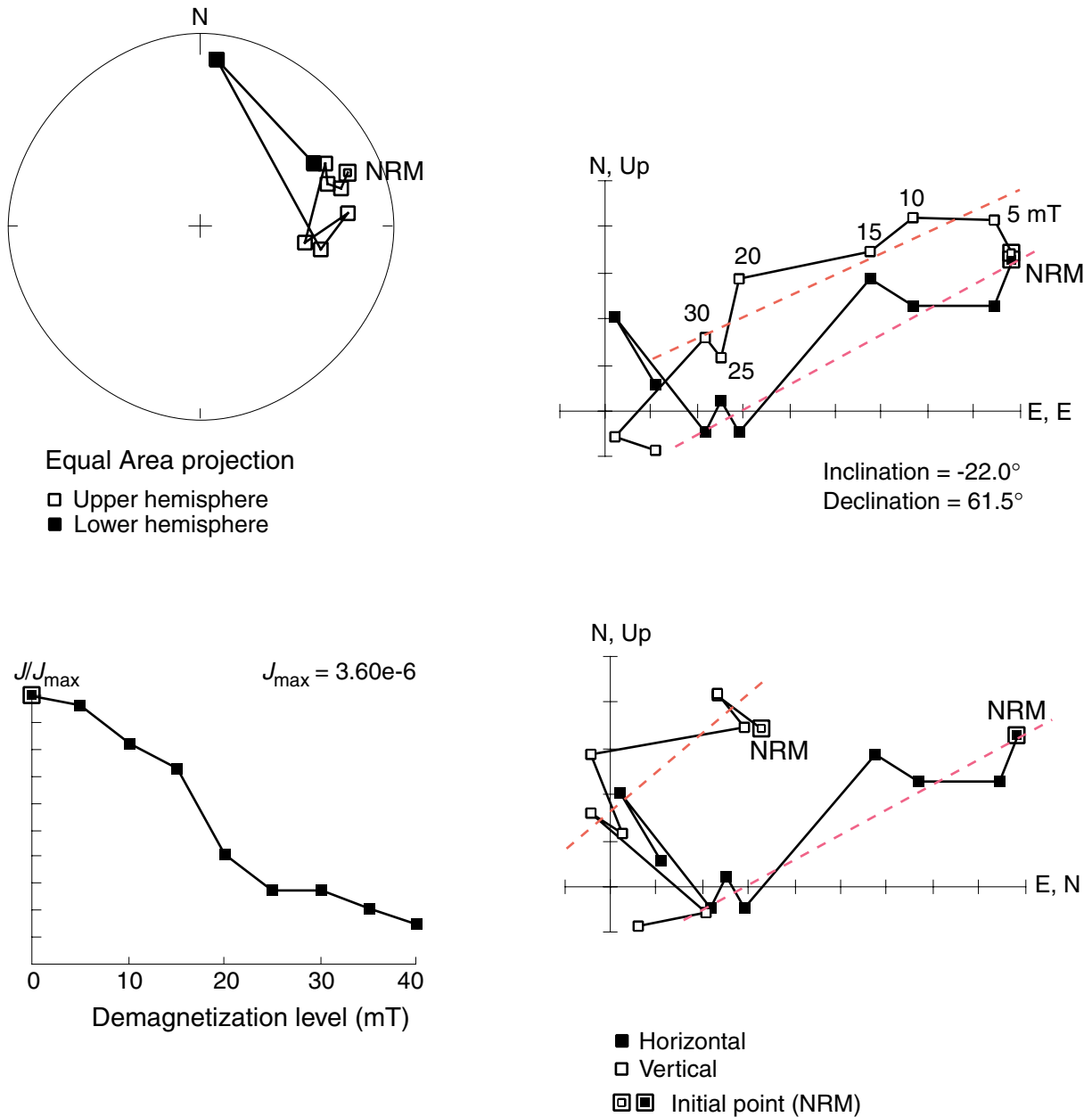
Figure F13. Principal component analysis of natural remanent magnetization (NRM) of Sample 201-1229A-3H-3, 65–67 cm including equal area projection of directions of magnetization during demagnetization, intensity of magnetization plotted vs. demagnetization, and vector component diagrams showing projection of magnetic vector's endpoints on horizontal and vertical planes. Numbers reflect demagnetization steps. Dashed line shows a 5- to 30-mT fitting inclination.

Sample 201-1229A-3H-3, 65-67 cm
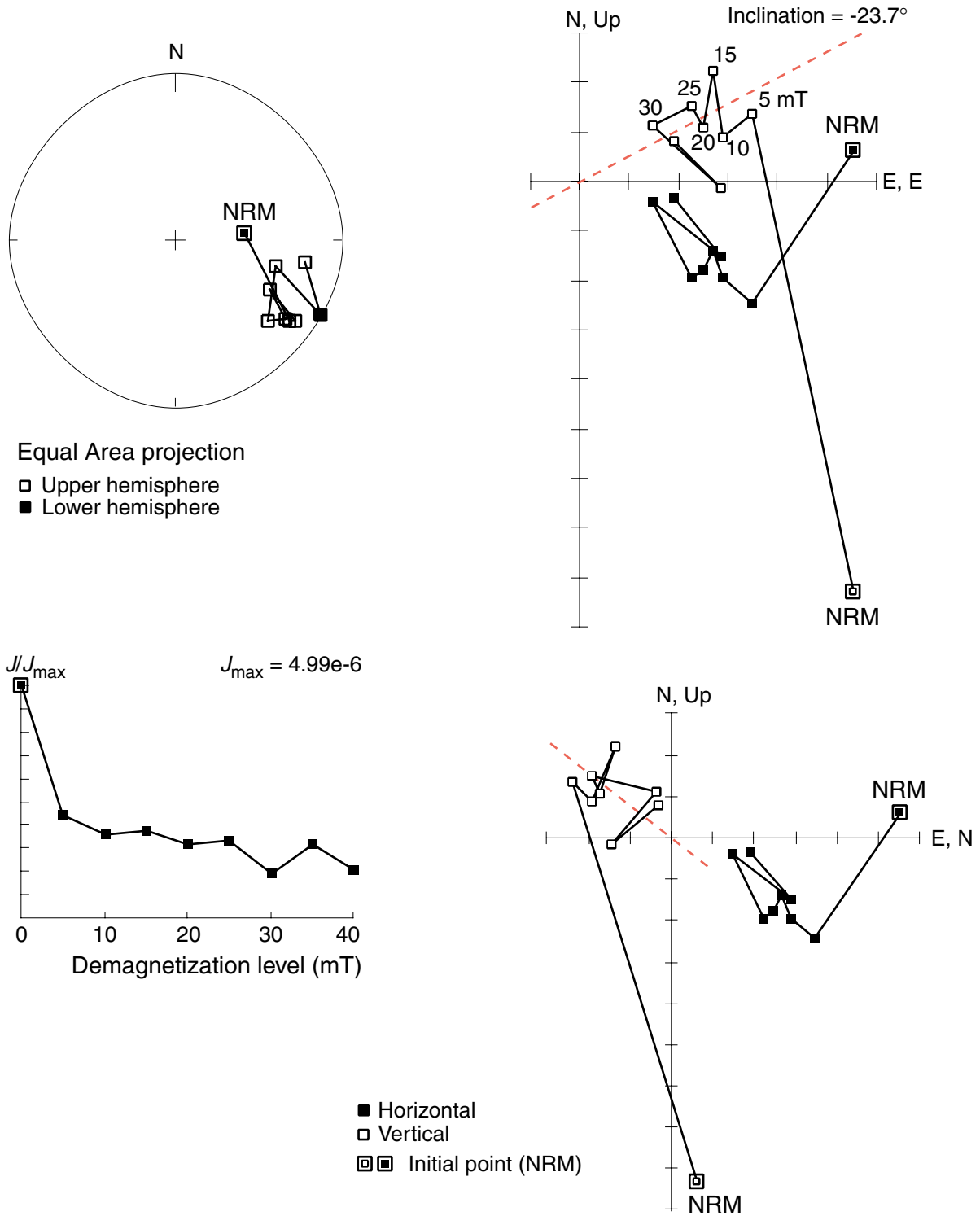
Figure F14. Principal component analysis of natural remanent magnetization (NRM) of Sample 201-1229A-14H-3, 110–112 cm, including equal area projection of directions of magnetization during demagnetization, intensity of magnetization plotted vs. demagnetization, and vector component diagrams showing projection of magnetic vector's endpoints on horizontal and vertical planes. Numbers reflect demagnetization steps. Dashed line shows a 20- to 40-mT fitting inclination.

Sample 201-1229A-14H-3, 110-112 cm
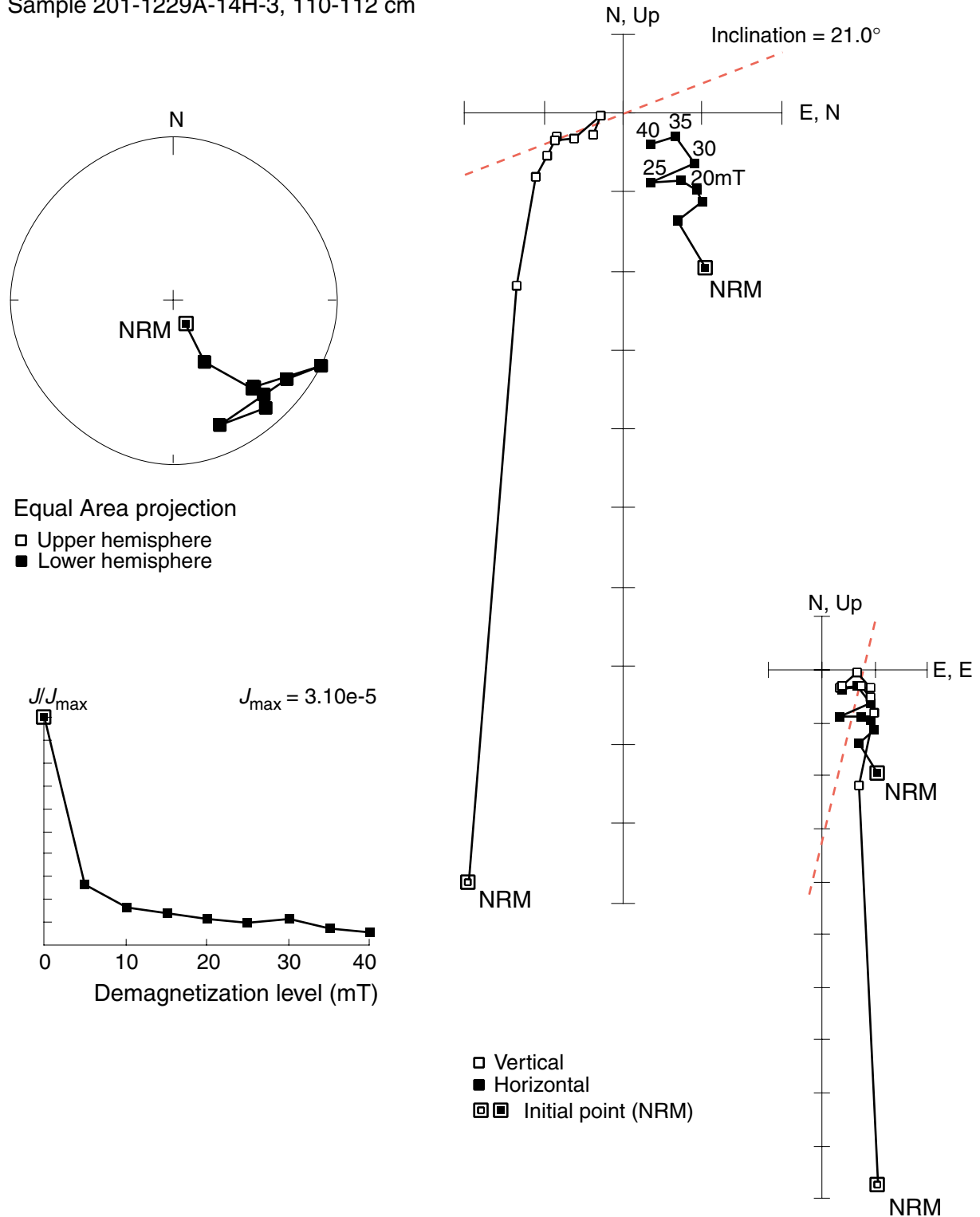
Figure F15. A. Gamma ray attenuation (GRA) density and discrete moisture and density (MAD) data from Hole 1229A compared with the wireline density log from the same hole. **B.** Grain density from Hole 1229A. **C.** Porosity calculated from MAD data compared with the wireline porosity log from the same hole.
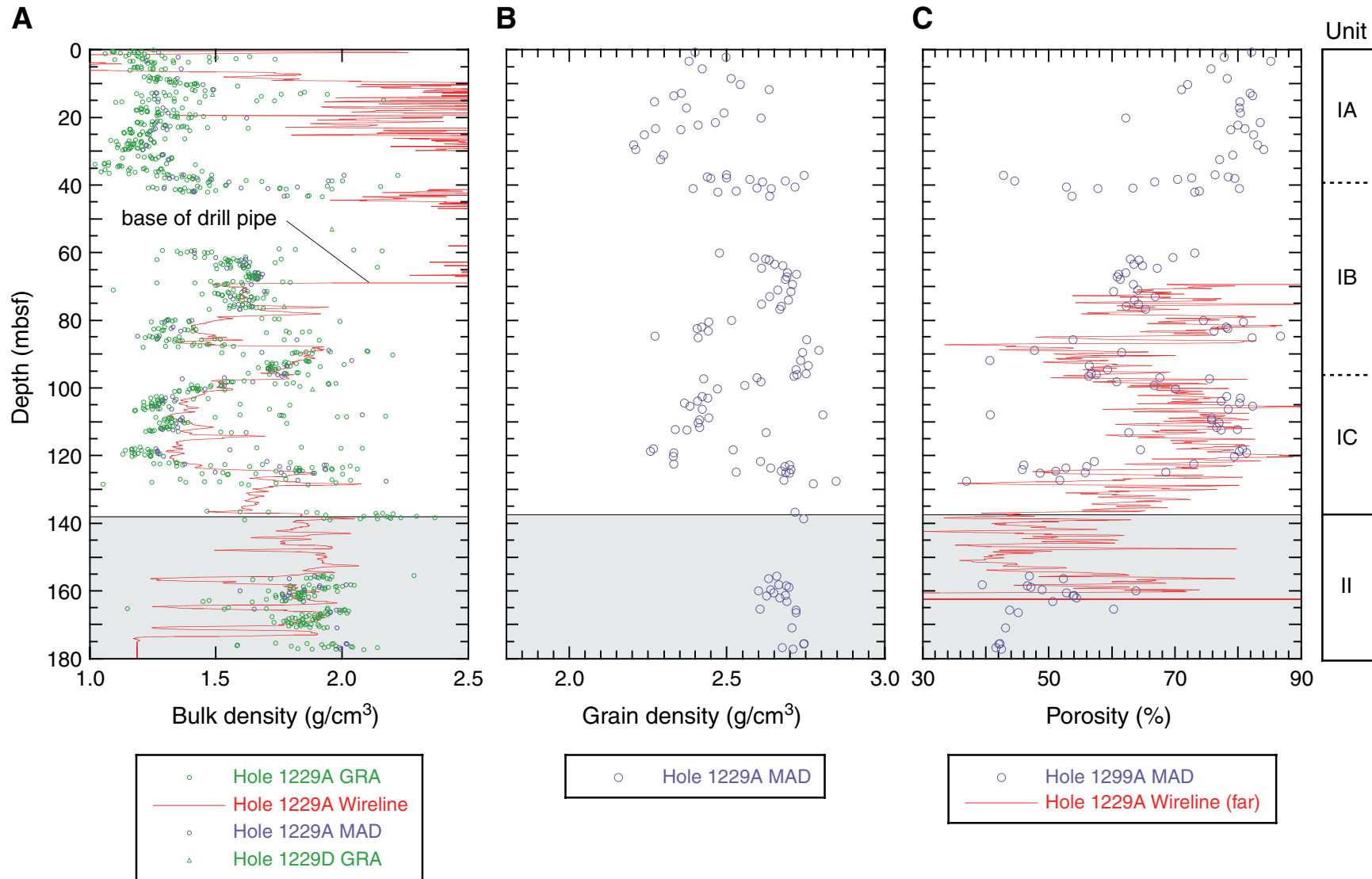
Figure F16. Wireline resistivity.
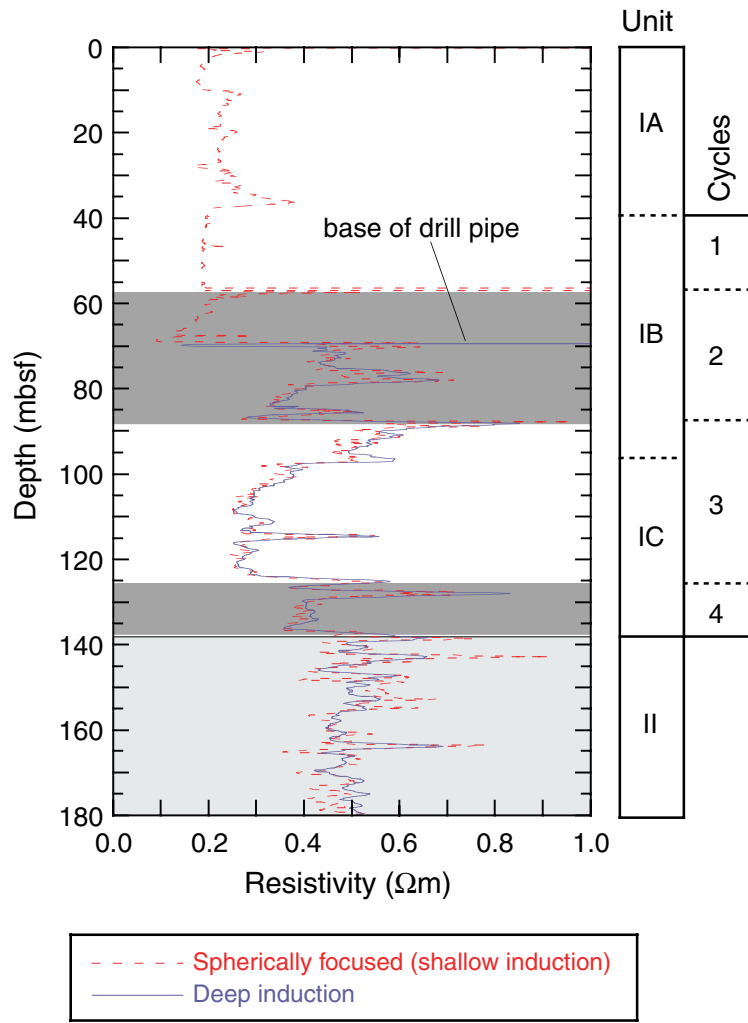
Figure F17. Mass/volume moisture and density (MAD) measurements for Hole 1229A over the interval of depositional cycles. **A.** Gamma ray attenuation (GRA) bulk density profiles. **B.** MAD and wireline porosity profile. **C.** Grain density profile.
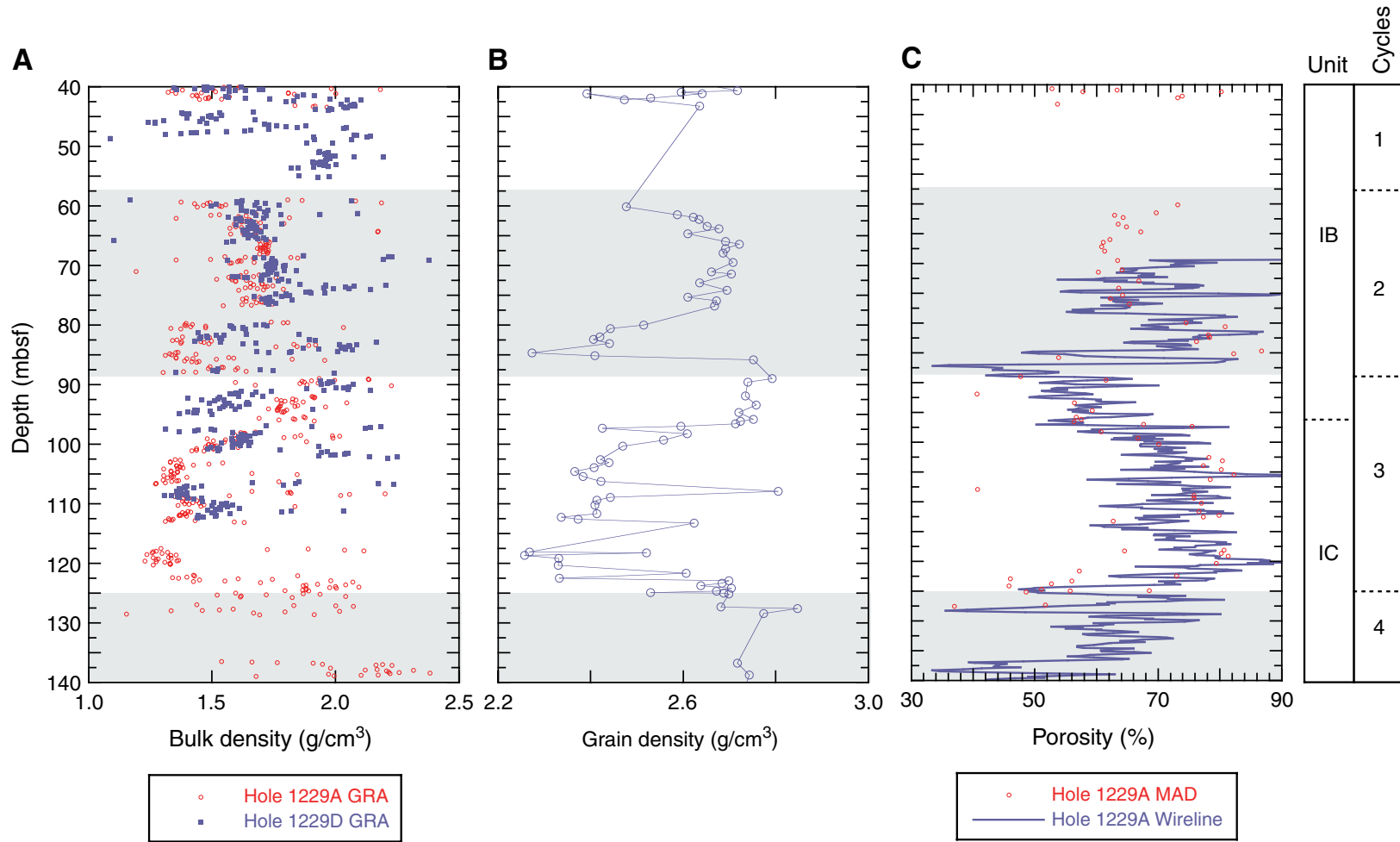
Figure F18. *P*-wave velocity profiles derived from *P*-wave logger (PWL) and PWS3 measurements. Peaks are highlighted with arrows and are due to phosphatic or dolomitic nodules.
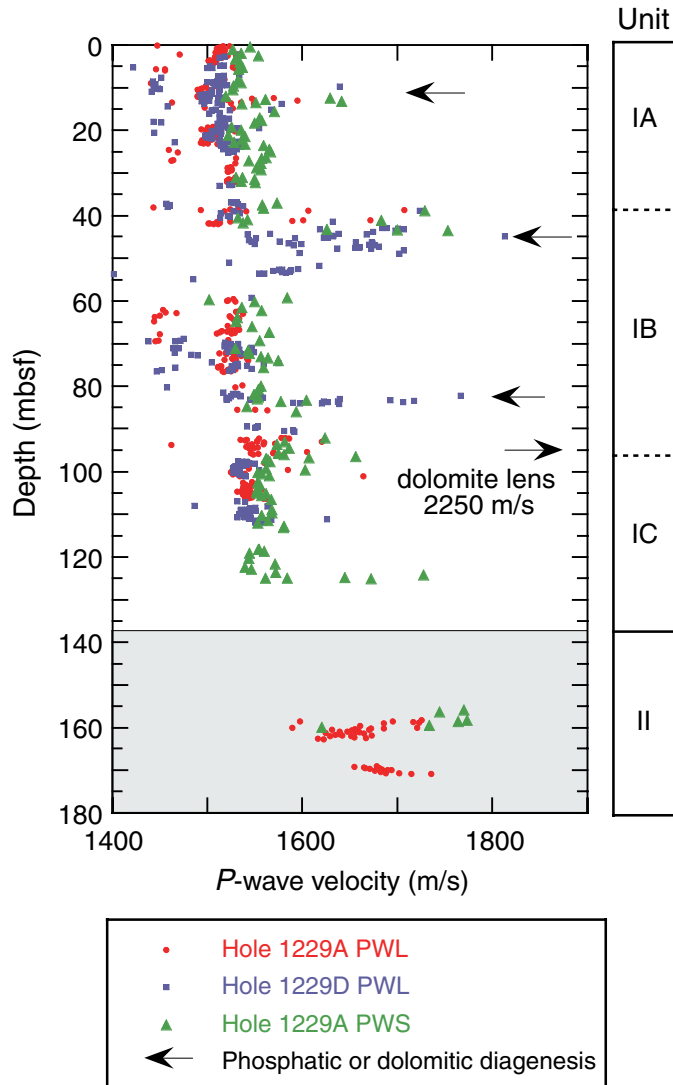
Figure F19. A. Natural gamma radiation (NGR) profile from the MST track compared with the wireline log record for Hole 1229A. **B.** Expanded scale of Subunits IA and IB showing the four gamma ray cycles described in the text.
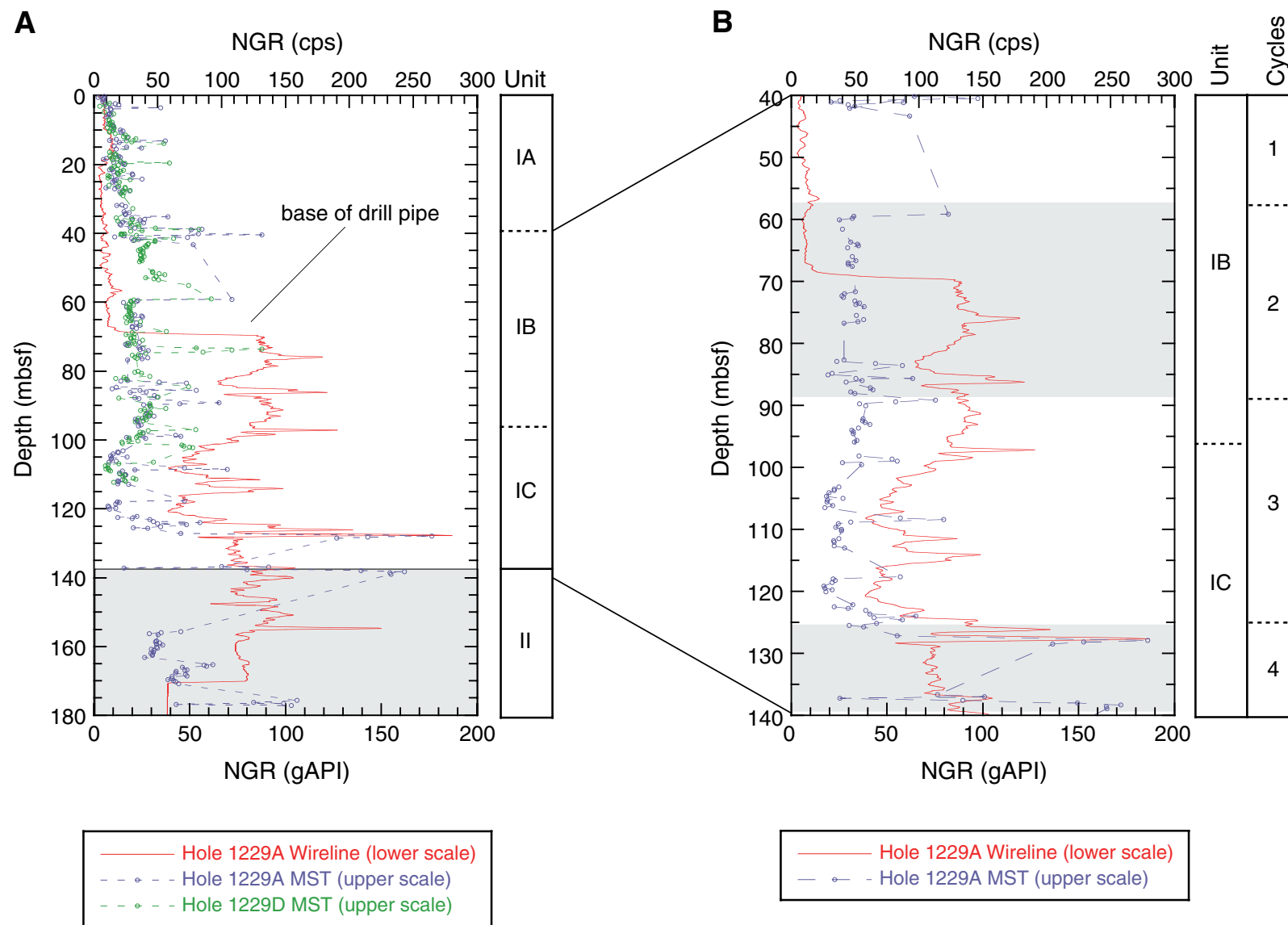
Figure F20. Thermal conductivity measurements for Hole 1229A. **A.** Thermal conductivity profile (needle probe method). **B.** Mean-detrended bulk density and thermal conductivity profiles illustrate the controlling effect of water content variability on thermal properties.
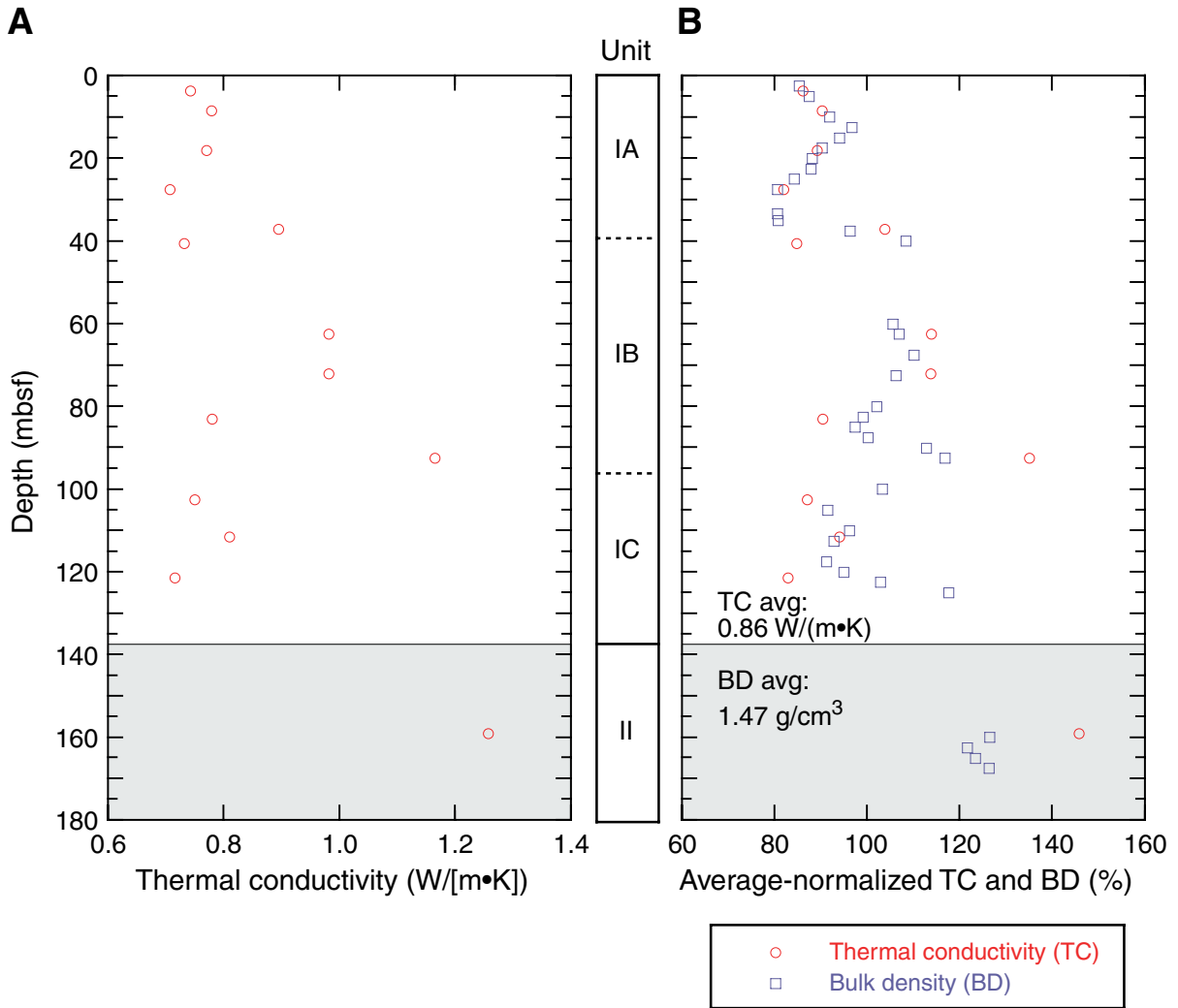
Figure F21. Formation factor profile for Hole 1229A. Three lithologies are indicated by the thick lines.
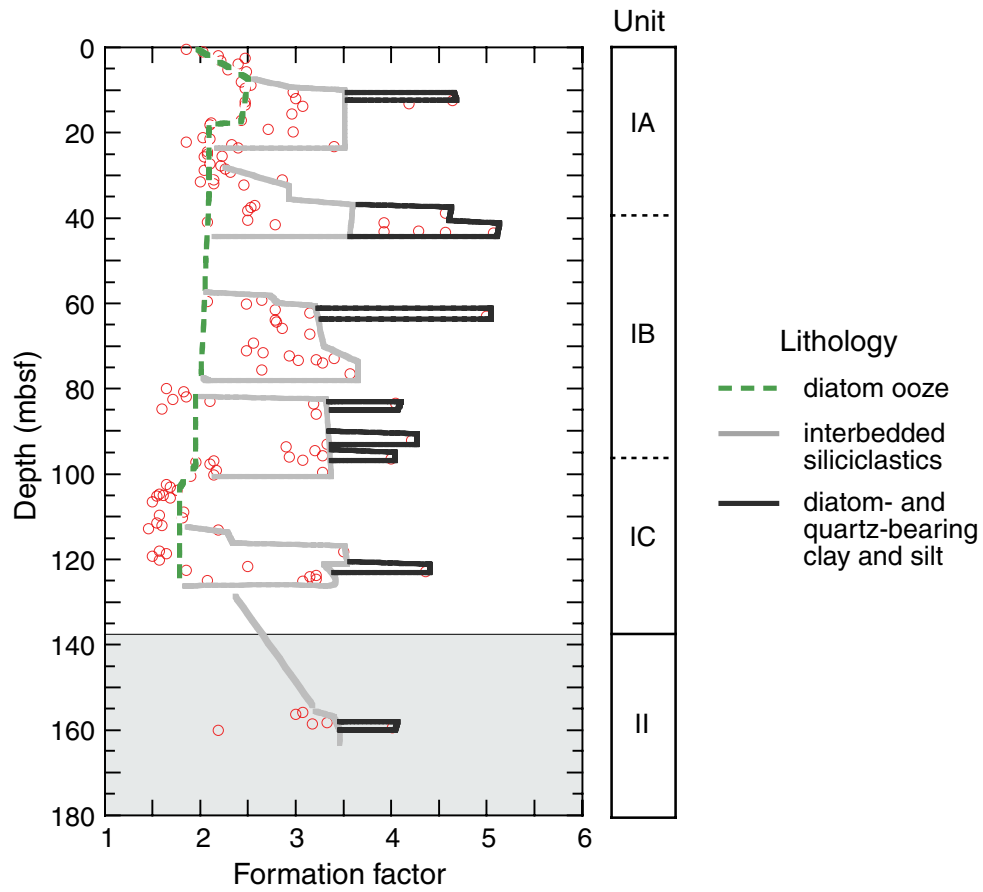
Figure F22. Temperature record for the DVTP deployment after Core 201-1229A-18H at 164.9 mbsf.
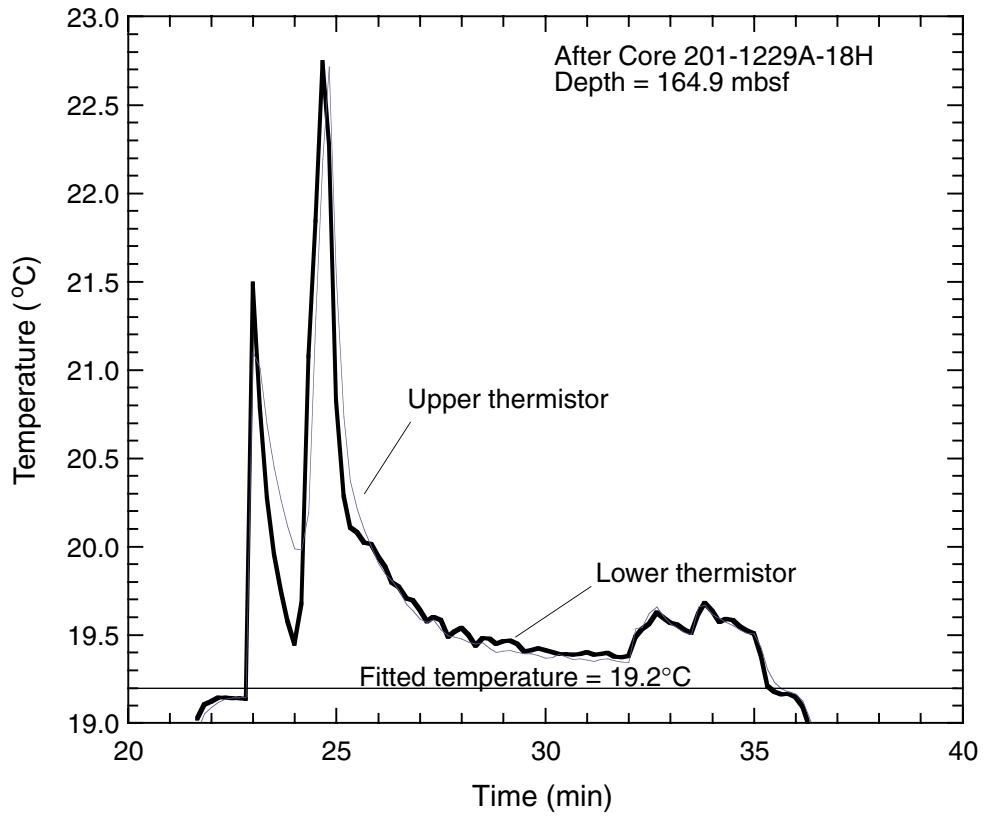
Figure F23. A. Temperature measured in Hole 1229A together with the temperature data from Site 681 plotted vs. depth with a best-fit linear profile for the combined data. **B.** Temperature data with steady-state conductive temperature profile calculated using measured thermal conductivities from Hole 1229A and uniform heat flow. DVTP = Davis-Villinger Temperature Probe.
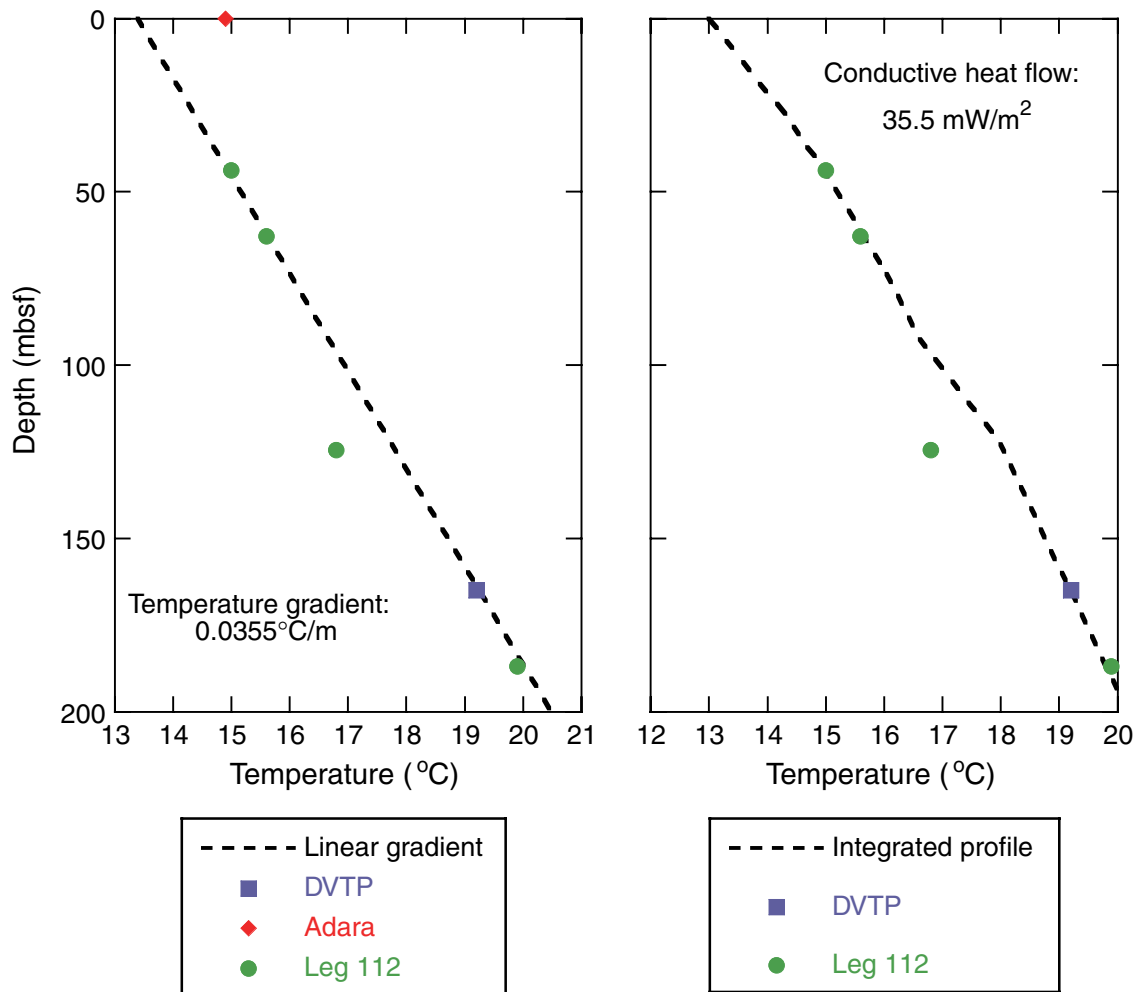
Figure F24. Pressure measured in Hole 1229A during the DVTP-P deployment after Core 201-1229-9H. BOH = bottom of hole.
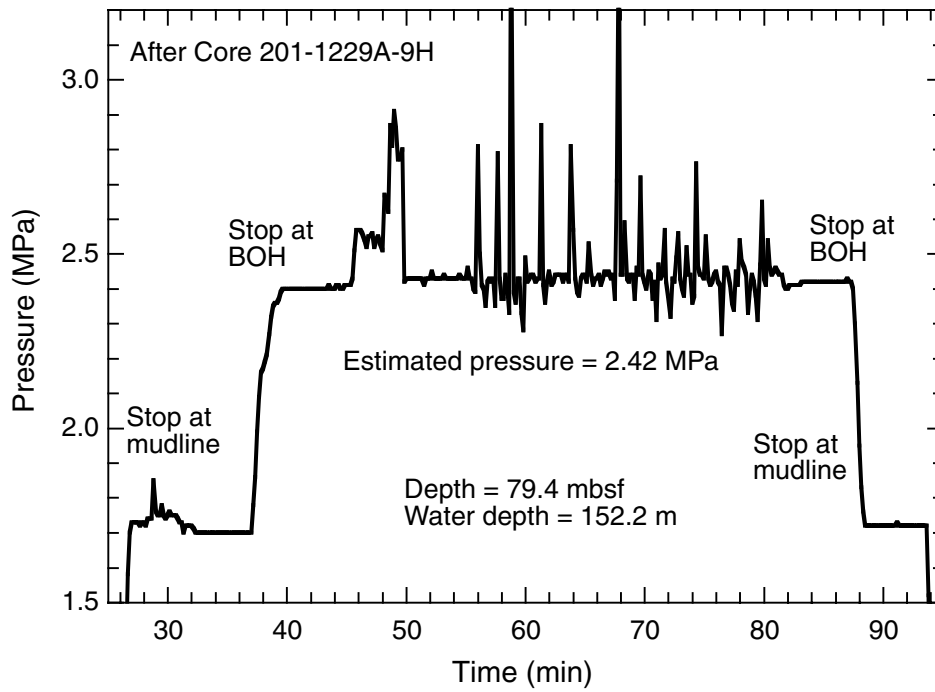
Figure F25. Main logs recorded in Hole 1229A. **A.** The hole diameter is measured by the caliper arm of the density sonde. **B.** The gamma ray is a measure of the natural radioactivity of the formation. **C.** Concentrations of potassium, thorium, and uranium derived from the gamma ray counts. **D.** Ratio of the thorium to uranium concentrations. High values indicate sediments of terrigenous origin. **E.** Resistivity measured by the Phasor Dual Induction Tool with three depths of investigation. **F.** Density log (red line) compared with density measurements made on core samples (shaded circles) (see **"Density and Porosity,"** p. 23, in "Physical Properties"). **G.** Porosity log for the two receivers of the APS sonde compared with porosity measurements made on core samples (shaded circles) (see **"Density and Porosity,"** p. 23, in "Physical Properties"). HNGS = Hostile Environment Natural Gamma Sonde, SGT = Scintillation Gamma Ray Tool.
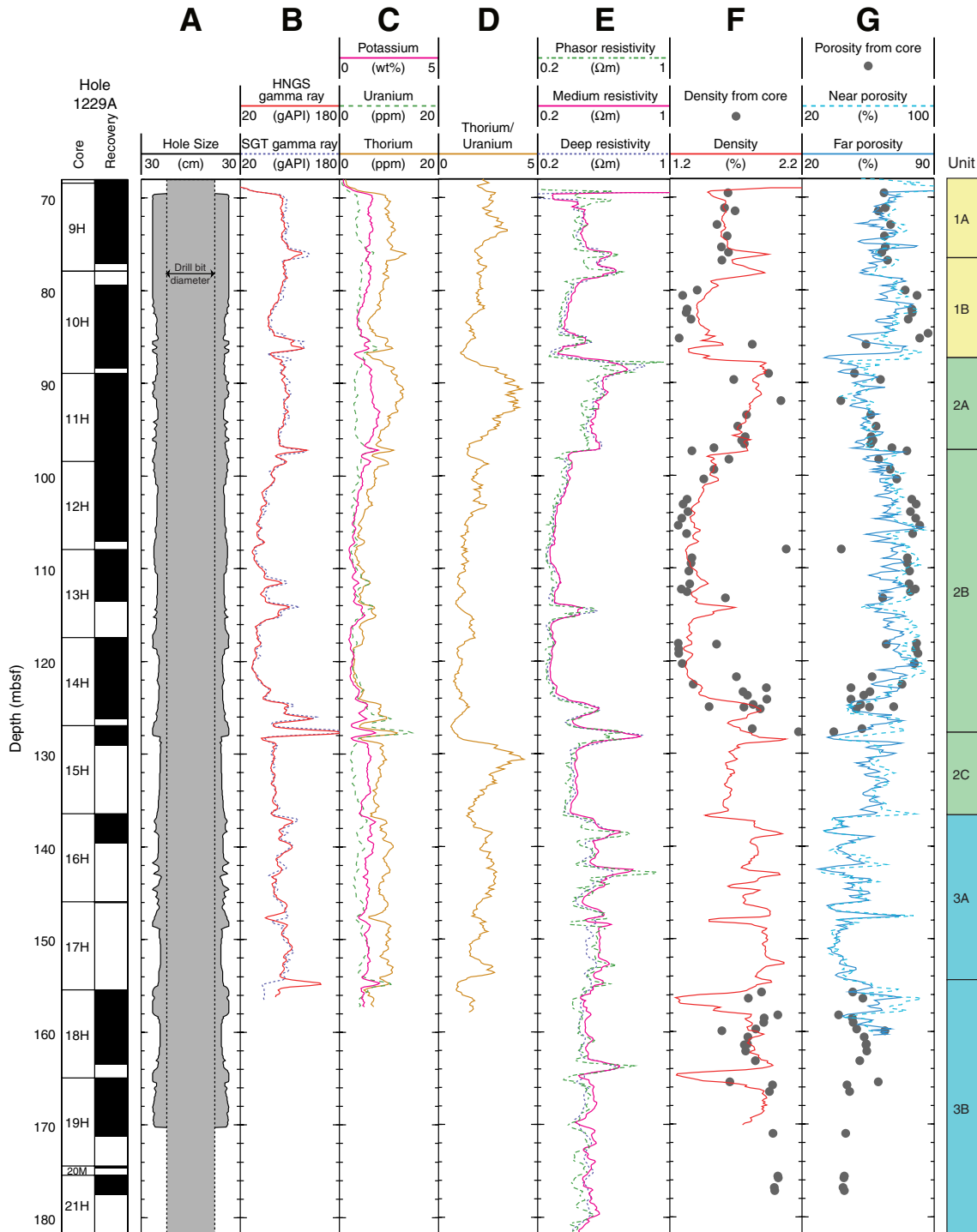
Figure F26. Comparison between data from the two passes of the triple combo string in Hole 1229A. **A.** Gamma ray. **B.** Resistivity. **C.** Density. Green dashed lines = data from the first pass, red solid lines = data from the second pass. HNGS = Hostile Environment Gamma Ray Sonde.
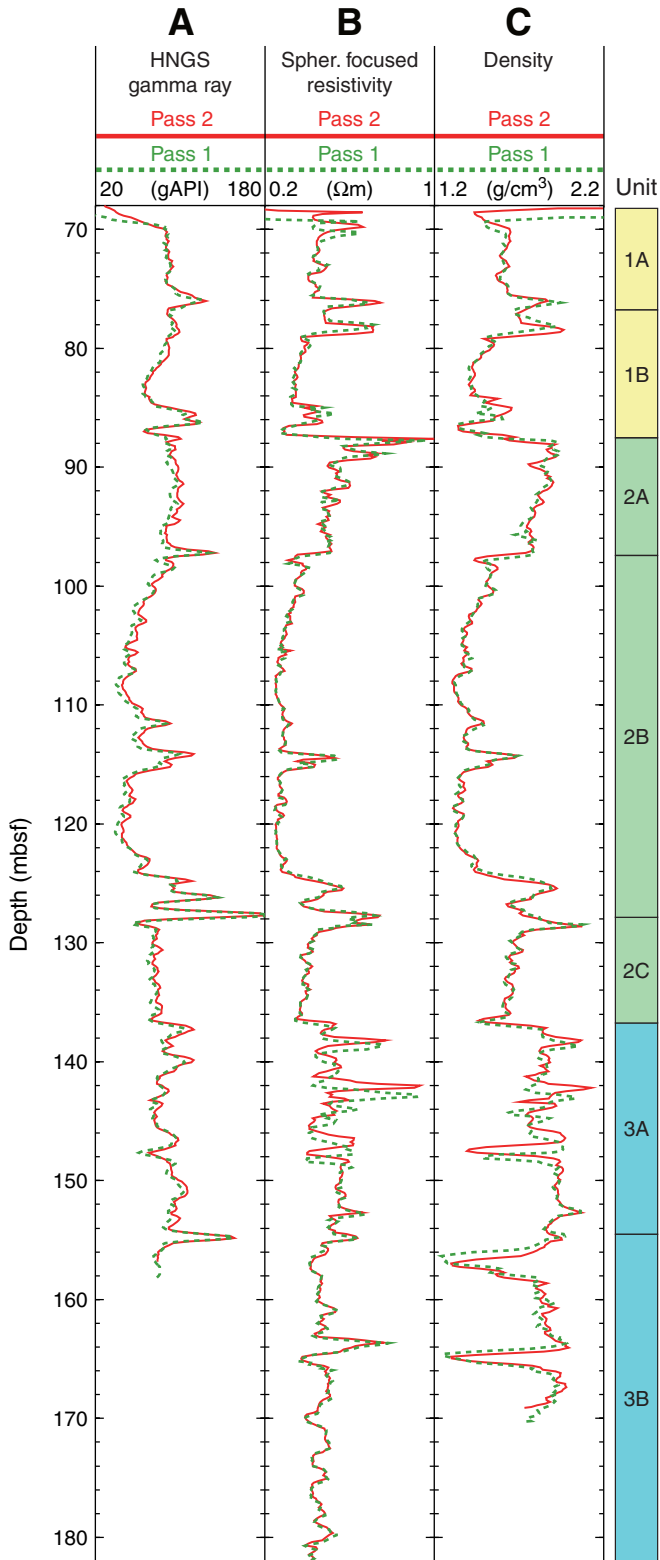
Figure F27. Temperature log recorded in Hole 1229A. Temperature data were recorded continuously during the two passes of the tool string.
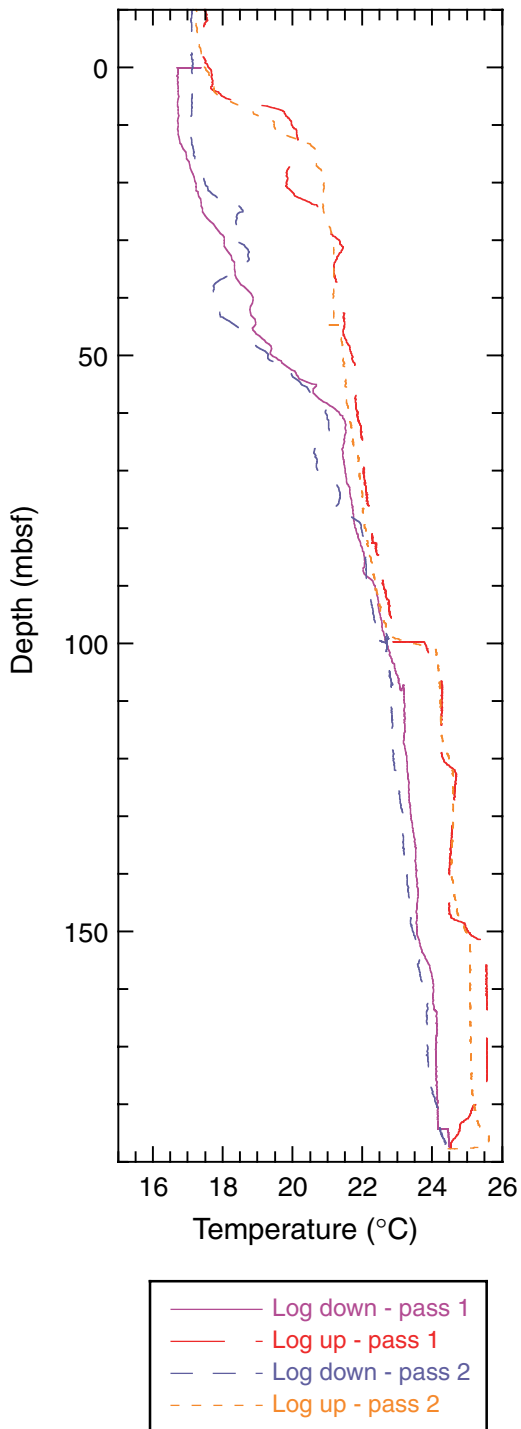
Table T1. Coring summary, Site 1229. (Continued on next page.)

Hole 1229A
  Latitude: 10°58.5721′S
  Longitude: 77°57.4590′W
  Time on site (hr): 90.0 (1330 hr, 6 Mar–0730 hr, 10 Mar 2002)
  Time on hole (hr): 49.33 (1330 hr, 6 Mar–1450 hr, 8 Mar 2002)
  Seafloor (drill pipe measurement from rig floor, mbrf): 163.6
  Distance between rig floor and sea level (m): 11.4
  Water depth (drill pipe measurement from sea level, m): 152.2
  Total depth (drill pipe measurement from rig floor, mbrf): 358.0
  Total penetration (meters below seafloor, mbsf): 194.4
  Total length of cored section (m): 192.9
  Total length of drilled intervals (m): 1.5
  Total core recovered (m): 133.1
  Core recovery (%): 69.0
  Total number of cores: 22
  Total number if drilled intervals: 1

Hole 1229B
  Latitude: 10°58.5697′S
  Longitude: 77°57.4586′W
  Time on hole (hr): 3.33 (1450 hr, 8 Mar–1810 hr, 8 Mar 2002)
  Seafloor (drill pipe measurement from rig floor, mbrf): 165.1
  Distance between rig floor and sea level (m): 11.4
  Water depth (drill pipe measurement from sea level, m): 153.7
  Total depth (drill pipe measurement from rig floor, mbrf): 190.5
  Total penetration (meters below seafloor, mbsf): 25.4
  Total length of cored section (m): 25.4
  Total core recovered (m): 24.84
  Core recovery (%): 97.8
  Total number of cores: 4

Hole 1229C
  Latitude: 10°58.5683′S
  Longitude: 77°57.4683′W
  Time on hole (hr): 1.58 (1810 hr, 8 Mar–1945 hr, 8 Mar 2002)
  Seafloor (drill pipe measurement from rig floor, mbrf): 162.7
  Distance between rig floor and sea level (m): 11.5
  Water depth (drill pipe measurement from sea level, m): 151.2
  Total depth (drill pipe measurement from rig floor, mbrf): 171.5
  Total penetration (meters below seafloor, mbsf): 8.8
  Total length of cored section (m): 8.8
  Total core recovered (m): 8.8
  Core recovery (%): 100.0
  Total number of cores: 1

Hole 1229D
  Latitude: 10°58.5672′S
  Longitude: 77°57.4704′W
  Time on hole (hr): 24.08 (1945 hr, 8 Mar–1950 hr, 9 Mar 2002)
  Seafloor (drill pipe measurement from rig floor, mbrf): 162.7
  Distance between rig floor and sea level (m): 11.5
  Water depth (drill pipe measurement from sea level, m): 151.2
  Total depth (drill pipe measurement from rig floor, mbrf): 278.5
  Total penetration (meters below seafloor, mbsf): 115.8
  Total length of cored section (m): 115.8
  Total core recovered (m): 100.97
  Core recovery (%): 87.2
  Total number of cores: 15

Hole 1229E
  Latitude: 10°58.5655′S
  Longitude: 77°57.4808′W
  Time on hole (hr): 11.67 (1950 hr, 9 Mar–0730 hr, 10 Mar 2002)
  Seafloor (drill pipe measurement from rig floor, mbrf): 162.0
  Distance between rig floor and sea level (m): 10.7
  Water depth (drill pipe measurement from sea level, m): 151.3
  Total depth (drill pipe measurement from rig floor, mbrf): 283.5
  Total penetration (meters below seafloor, mbsf): 121.5
  Total length of cored section (m): 121.5
  Total core recovered (m): 99.64
  Core recovery (%): 82.0
  Total number of cores: 13

Table T1 (continued).

Core	Date (Mar 2002)	Local time (hr)	Depth (mbsf) Top	Bottom	Length (m) Cored	Recovered	Recovery (%)
201-1229A-							
1H	6	1730	0.0	4.9	4.9	4.89	99.8
2H	6	1830	4.9	14.4	9.5	9.34	98.3
3H	6	2045	14.4	23.9	9.5	9.65	101.6
4H	6	2255	23.9	33.4	9.5	8.96	94.3
5H	7	0045	33.4	39.9	6.5	8.99	138.3
6H	7	0210	39.9	49.4	9.5	3.80	40.0
7H	7	0340	49.4	58.9	9.5	0.16	1.7
8H	7	0435	58.9	68.4	9.5	9.55	100.5
9H	7	0610	68.4	77.9	9.5	8.74	92.0
			*****Drilled from 77.9 to 79.4 mbsf*****				
10H	7	0940	79.4	88.9	9.5	8.96	94.3
11H	7	1045	88.9	98.4	9.5	9.83	103.5
12H	7	1325	98.4	107.9	9.5	8.68	91.4
13H	7	1510	107.9	117.4	9.5	5.62	59.2
14H	7	1700	117.4	126.9	9.5	8.78	92.4
15H	7	1820	126.9	136.4	9.5	2.13	22.4
16H	7	1945	136.4	145.9	9.5	3.21	33.8
17H	7	2055	145.9	155.4	9.5	0.09	1.0
18H	7	2230	155.4	164.9	9.5	8.10	85.3
19H	8	0035	164.9	174.4	9.5	6.32	66.5
20M	8	0250	174.4	175.4	1.0	0.26	26.0
21H	8	0320	175.4	184.9	9.5	2.14	22.5
22H	8	0455	184.9	194.4	9.5	4.90	51.6
			Cored totals:		192.9	133.10	69.0
			Drilled total:		1.5		
			Total:		194.4		
201-1229B-							
1H	8	1610	0.0	5.4	5.4	5.39	99.8
2H	8	1630	5.4	14.9	9.5	9.63	101.4
3H	8	1650	14.9	24.4	9.5	9.82	103.4
4M	8	1730	24.4	25.4	1.0	0.00	0.0
			Cored totals:		25.4	24.84	97.8
201-1229C-							
1H	8	1940	0.0	8.8	8.8	8.80	100.0
			Cored totals:		8.8	8.80	100.0
201-1229D-							
1H	8	2005	0.0	6.8	6.8	6.79	99.9
2H	9	0005	6.8	16.3	9.5	9.67	101.8
3H	9	0145	16.3	25.8	9.5	9.38	98.7
4H	9	0335	25.8	35.3	9.5	7.73	81.4
5H	9	0510	35.3	39.8	4.5	5.75	127.8
6H	9	0630	39.8	49.3	9.5	9.42	99.2
7H	9	0740	49.3	58.8	9.5	6.57	69.2
8H	9	0900	58.8	68.3	9.5	7.65	80.5
9H	9	1025	68.3	77.8	9.5	8.58	90.3
10P	9	1230	77.8	79.8	2.0	0.86	43.0
11H	9	1300	79.8	84.3	4.5	4.75	105.6
12H	9	1420	84.3	87.3	3.0	3.36	112.0
13H	9	1615	87.3	96.8	9.5	8.04	84.6
14H	9	1735	96.8	106.3	9.5	5.92	62.3
15H	9	1900	106.3	115.8	9.5	6.50	68.4
			Cored totals:		115.8	100.97	87.2
201-1229E-							
1H	9	2030	0.0	7.5	7.5	7.46	99.5
2H	9	2115	7.5	17.0	9.5	9.62	101.3
3H	9	2145	17.0	26.5	9.5	9.35	98.4
4H	9	2215	26.5	36.0	9.5	8.62	90.7
5H	9	2235	36.0	45.5	9.5	9.61	101.2
6H	9	2310	45.5	55.0	9.5	4.75	50.0
7H	10	0030	55.0	64.5	9.5	9.52	100.2
8H	10	0100	64.5	74.0	9.5	9.68	101.9
9H	10	0130	74.0	83.5	9.5	3.47	36.5
10H	10	0310	83.5	93.0	9.5	2.70	28.4
11H	10	0350	93.0	102.5	9.5	9.48	99.8
12H	10	0425	102.5	112.0	9.5	9.56	100.6
13H	10	0450	112.0	121.5	9.5	5.82	61.3
			Cored totals:		121.5	99.64	82.0

Table T2. Concentrations of dissolved species in interstitial waters, Holes 1229A and 1229D. (**See table notes.** Continued on next two pages.)

Core, section, interval (cm)	Depth (mbsf)	pH	Alk (mM)	Cl⁻ (mM)	SO₄²⁻ (mM)	H₄SiO₄ (µM)	PO₄³⁻ (µM)	NH₄⁺ (µM)	Fe (µM)	Mn (µM)	Sr (µM)	Li (µM)	Ba (µM)	ΣH₂S (mM)	DIC (mM)	Acetate (µM)	Formate (µM)
201-1229A-																	
1H-1, 135–150	1.35	7.91	21.6	573.04	16.12			2,570	1.1	0.1	91	28	0.4	5.54	20.96	1.2	1.3
1H-3, 131–148	4.31	7.54	16.1	578.10	15.32		7.6	2,540	0.5	0.0	90	33	0.4	5.48	16.24	1.4	1.3
2H-1, 135–150	6.25	7.47	17.4	586.65	15.70			2,310	0.6	0.0	99	37	0.3	5.39	17.48		
2H-3, 135–150	9.25	7.49	15.1	597.23	15.34		8.2	2,240	0.6	0.0	106	43	0.4	5.06	14.87	1.0	0.8
2H-5, 135–150	12.25	7.37	14.5	596.17	12.91		6.6	2,430	1.2	0.1	118	50	0.5	4.33	15.13		
3H-1, 135–150	15.75	7.37	15.2	611.53	9.70			2,770	0.4	0.1	129	57	0.6	3.93	14.92		
3H-3, 135–150	18.75	7.47	14.5	632.20	8.40		7.2	3,040	3.6	0.3	136	60	0.7	5.43	17.14	1.5	2.6
3H-5, 135–150	21.75	7.43	16.6	638.26	6.29			3,260	0.6	0.2	143	65	0.8	5.17	17.89	1.2	0.8
4H-1, 135–150	25.25	7.29	17.8	656.65	3.60	948	9.2	3,540	1.5	0.0	150	70	1.5	5.78	19.40	0.7	0.6
4H-3, 135–150	28.25	7.54	18.6	660.28	2.17		11.2	3,790	0.7	0.1	158	75	4.6	5.94	20.38	1.2	1.7
4H-5, 135–150	31.25	7.50	19.2	657.94	1.00	1022	12.8	4,080	1.7	0.3	159	78	8.3	6.42	20.53	1.4	1.8
5H-3, 135–150	37.75	7.43	18.8	667.635	0.00		11.5	4,340	0.8	0.1	169	85	13.4	6.02	17.33	1.1	1.2
5H-4, 135–150	39.25	7.30	18.0	684.85	0.00		6.5	4,720	0.5	0.2	180	94	17.1		20.19	1.7	1.7
5H-5, 135–150	40.75	6.90	18.1	688.19	0.00	1005	6.5	4,550	3.9	0.6	176	92	16.7	5.24	20.24		
6H-1, 135–150	41.25	7.26	18.0	686.42	0.00	999	7.5	5,010	1.2	0.2	181	95	17.8	5.33	20.19	1.5	1.5
6H-3, 0–15	42.90	7.37	19.1	697.57	0.00	959	10.2	4,650	0.7	0.3	188	95	18.0	4.43		1.6	1.4
8H-1, 135–150	60.25	7.16	16.5	773.58	0.00	986	5.6		0.4	0.5	237	126	18.5	2.28	15.33		
8H-3, 135–150	63.25	7.16	16.1	801.68	0.00	825	6.1	5,440	0.9	1.5	249	136	18.5	2.29	15.90	1.7	1.4
8H-5, 135–150	66.25	7.18	16.5	810.35	0.00	953	6.0	5,560	1.3	0.9	238	130	18.5	2.09	19.23		
9H-1, 135–150	69.75	7.12	15.8	774.58	2.52	927	6.4	5,300	4.7	1.8	244	132	17.5	1.75	18.73	1.6	0.6
9H-2, 135–150	71.25	6.81	16.1	807.00	0.04	1031	4.8	5,760	1.0	1.6	254	137	18.2	2.44	19.08		
9H-3, 135–150	72.75	6.82	15.9	818.67	0.59		4.3	5,710	0.9	1.5	262	144	18.8	1.91	19.22	3.3	2.7
9H-4, 135–150	74.25	6.93	15.7	826.13	0.00		5.0	5,480	5.6	1.2	259	141	18.8	1.74	19.18		
9H-5, 135–150	75.75	6.95	15.8	803.49	0.00		4.9	5,500	1.8	0.8	261	140	19.0	1.93	19.55	1.5	1.0
9H-6, 95–110	76.85	7.15	15.8	812.06	0.79		2.3	5,630	186.1	10.5	252	147	17.7	0.038	18.28	2.1	1.5
10H-1, 135–150	80.75	7.17	15.1	836.03	0.00		5.6	5,640	0.9	0.5	275	147	17.9	1.99		1.3	1.8
10H-2, 135–150	82.25	7.30	14.6	858.19	0.00		4.7	5,690	11.3	0.7	275	147	17.4	0.45		1.5	1.6
10H-3, 135–150	83.75	6.85	15.0	872.20	0.00	1028		5,650	2.3	0.7	282	149	17.1	1.24	18.59	1.1	0.6
10H-4, 135–150	85.25	7.24	14.3	862.79	0.00		5.0	5,380	15.5	0.6	280	150	15.8	0.55	17.69	1.6	2.4
10H-7, 122–136	88.14	7.31	9.6				5.5		4.6	1.7	184	83	10.5		11.52	1.6	2.6
11H-1, 135–150	90.25	7.31	14.6	898.82	0.62	878	4.7	5,470	0.9	1.2	290	160	9.4	2.86	11.33	5.7	3.9
11H-2, 135–150	91.75	7.31	14.8	903.80	0.95		4.2	5,350	0.7	1.4	291	158	7.6	2.56	16.26	0.7	1.3
11H-3, 135–150	93.25	7.31	15.0	914.52	1.33		4.5	5,070	0.6	1.2	298	163	6.1	2.62	15.35	2.1	1.4
11H-4, 135–150	94.75	6.86	14.1	919.89	1.70		4.3	5,450	2.4	1.0	296	157	4.5	1.83	17.04	1.2	1.2
11H-5, 135–150	96.25	7.30	14.4	912.69	2.11		3.7	5,480	0.9	0.7	304	164	3.5	2.73	17.63	1.5	1.9
11H-6, 135–150	97.75	7.23	14.2	919.64	2.53	989	5.3	5,190	1.1	0.5	302	156	2.9	1.96	17.54	2.4	1.1
12H-1, 135–150	99.75	6.82	13.8	924.64	3.01	999	4.7	13,100	2.9	0.5	306	166	2.3	2.38	17.09	1.3	1.7
12H-2, 135–150	101.25	7.13	13.8	935.08	3.33		4.5	5,010	0.4	0.4	301	158	2.0	2.59	16.93		
12H-3, 135–150	102.75	7.27	13.5	943.03	3.79		4.7	5,240	0.9	0.5	311	162	1.7	2.41	16.41	0.7	0.8
12H-4, 135–150	104.25	7.23	13.3	949.99	4.06		4.5	5,640	0.6	0.5	307	161	1.6	2.20	16.30		
12H-5, 135–150	105.75	7.22	13.3	964.75	4.47		4.0	5,050	1.0	0.5	309	161	1.5	2.55	15.98	1.2	1.2
13H-1, 135–150	109.25	7.24	12.9	969.17	5.17		4.1	5,240	2.4	0.4	315	167	1.3	2.35	15.76		
13H-2, 135–150	110.75	7.13	12.9	973.02	5.55		4.4	4,960	0.8	0.4	312	163	1.2	2.32	15.68	0.8	2.1
13H-3, 135–150	112.25	6.99	12.7	984.99	5.98	1002	3.9		0.7	0.4	317	164	1.2	2.30	16.11		
14H-1, 135–150	118.75	7.19	11.8	991.32	8.13	969	4.7	4,950	1.2	0.5	326	171	0.9	1.97	14.54	1.2	1.2
14H-3, 135–150	121.75	7.00	11.5	985.20	8.72		4.0	4,910	0.9	0.8	324	166	0.9	1.81	14.23		
14H-5, 135–150	124.75	6.94	11.3	1002.74	9.86	951			8.6	1.2	328	169	1.2	1.42	13.74	3.8	3.5
15H-1, 49–64	127.39	6.97	10.7						1.7	0.7	329	173	0.9	1.65	12.79	0.1	1.5

Table T2 (continued).

Core, section, interval (cm)	Depth (mbsf)	pH	Alk (mM)	Cl⁻ (mM)	SO₄²⁻ (mM)	H₄SiO₄ (µM)	PO₄³⁻ (µM)	NH₄⁺ (µM)	Fe (µM)	Mn (µM)	Sr (µM)	Li (µM)	Ba (µM)	ΣH₂S (mM)	DIC (mM)	Acetate (µM)	Formate (µM)
18H-1, 135–150	156.75	6.76	7.7	1134.93	26.94		5.2		7.9	2.3	345	175	0.5	0.319	8.98	1.4	2.8
18H-3, 135–150	159.75	6.76	7.3	1137.96	28.08	1019	4.7	4,330	8.1	2.3	349	182	0.6			2.0	1.7
19H-1, 135–150	166.25			1161.29	30.96				3.7	6.6	356	180	0.6	0.068		6.5	6.7
21H-2, 93–108	176.90			1175.00	34.83				5.2	7.4	348	179	0.9			11.9	12.1
22H-1, 135–150	186.25	6.77	5.8	1208.25	38.03		7.8		4.0	5.9	361	184	0.5	0.00078	6.81	0.9	0.8
201-1229D-																	
1H-1, 0–1	0.00			553.72													
1H-1, 0–12	0.00	7.83	14.2	558.85	22.53		41.8	1,460	0.9	0.1	89	27	0.3	2.34	11.56	1.7	1.8
1H-1, 12–25	0.12	7.77	12.6	540.44	20.84				0.6	0.0	90	27	0.3	3.09	12.99	2.2	1.8
1H-1, 25–35	0.25	7.82	15.6	564.61	20.70		42.4	1,620	2.7	0.1	90	27	0.3	3.36	13.94	2.8	2.0
1H-1, 40–50	0.40	8.07	17.0	563.17	19.30		40.1	2,670	0.6	0.1	90	26	0.3	3.82	15.08	1.7	1.9
1H-1, 50–60	0.50	7.84	18.2	556.16	18.37		39.4		1.2	0.1	89	26	0.3	4.65	16.70	2.0	1.4
1H-1, 97–112	0.97	7.86	22.0	564.80	16.47		41.6	2,370	1.3	0.1	89	26	0.4	5.84	18.83	1.6	1.0
1H-1, 142–152	1.42	7.90	21.5	559.21	15.30		41.5	2,420	1.5	0.2	90	28	0.5		18.82		
1H-1, 180–190	1.80			559.70	14.70		39.9		0.9	0.1	89	28	0.4	6.15	19.74		
1H-2, 34–50	2.34	7.84	21.6	560.29	14.13		30.9	2,540	0.7	0.2	89	30	0.4	6.37	19.30		
1H-2, 125–135	3.25	7.80	19.6	557.32	14.13		16.5	2,520	1.0	0.2	90	32	0.4	5.78	17.76		
1H-3, 0–10	3.50			563.70	14.27			4,380	1.0	0.2	92	33	0.5	5.20	17.68		
1H-4, 0–10	5.00	7.74	16.3	569.99	15.06		11.7		1.2	0.1	95	36	0.4	4.22	15.41		
1H-5, 0–10	6.00	7.66	16.0	573.06	15.29	824	11.1		0.9	0.1	97	38	0.4	4.84	16.42		
2H-1, 135–150	8.15	7.71	15.4	572.95	15.18				0.4	0.1	103	40	0.3	5.01	14.56		
2H-2, 135–150	9.65	7.63	15.4	581.96	15.13				0.3	0.1	106	43	0.3	4.64	15.13		
2H-3, 135–150	11.15	7.63	14.9	578.27	14.33	907			0.7	0.1	110	46	0.4	4.88	14.79		
2H-4, 135–150	12.65	7.65	14.7	580.46	13.31			2,050						4.91	15.02		
2H-5, 135–150	14.15	7.80	14.7	589.97	12.28				0.5	0.1	118	50	0.4	4.45	13.73		
2H-6, 135–150	15.65	7.66	14.4	572.51	12.23			2,160	0.2	0.2	118	51	0.6	5.02	13.30		
2H-7, 26–41	16.06	7.66	14.4	577.80	12.71				3.9	1.2	116	50	0.5	4.44	14.75		
3H-1, 135–150	17.65	7.55	15.8	607.20	8.43	960		2,810	0.4	0.1	136	60	0.7	5.17	16.83		
3H-2, 135–150	19.15	7.35	16.4	592.68	7.22				0.9	0.2	136	61	0.7	5.70	16.98		
3H-3, 135–150	20.65	7.52	16.7	603.98	6.14				0.5	0.1	142	65	0.7	5.88	15.04		
3H-4, 135–150	22.15	7.33	17.0	614.85	5.58	932								5.99	17.46		
3H-5, 135–150	23.65	7.34	17.6	626.93	4.02				0.7	0.1	150	69	1.2	5.56	18.26		
3H-6, 85–100	24.65	7.51	17.4	609.86	3.50			3,340	0.4	0.1	149	68	1.3	5.30	17.83		
3H-7, 52–67	25.32	7.61	17.5	628.74	2.88			3,270	0.3	0.1	154	70	1.3	5.90	18.74		
4H-1, 135–150	27.15	7.61	18.4	604.85	1.88			3,350	0.4	0.2	158	74	4.5	5.68	19.38		
4H-2, 135–150	28.65	7.70	18.6		1.35				0.4	0.2	160	75	6.2	5.75	18.85		
4H-3, 135–150	30.15	7.55	18.7		0.96	948		3,670	0.9	0.4	162	78	7.9	6.25	21.14		
4H-4, 68–83	30.98	7.48	19.1		0.73				0.9	0.2	160	76	8.8	5.48	18.85	3.4	3.8
4H-4, 135–150	31.65	7.52	17.4		0.62			3,980	0.2	0.2	164	79	9.8	5.72		1.3	1.5
4H-5, 128–143	33.08	7.34	18.9		0.29			4,080	0.3	0.2	167	82	11.0	5.58	19.40	3.9	4.1
5H-1, 135–150	36.65	7.41	18.0		0.64			4,160	1.2	0.4	170	83	14.6	5.38	19.98	6.5	6.7
5H-2, 135–150	38.15	7.31	18.2		0.02			4,400	0.6	0.3	177	89	15.9	5.59	19.22	2.2	1.2
5H-3, 135–150	39.65	7.44	17.7		0.00				0.5	0.2	181	90	17.0	5.39	19.42	0.7	0.6
5H-4, 90–105	40.70	7.40	17.9		0.00	921		4,480	0.2	0.2	181	91	17.8	5.26	19.66		
6H-1, 135–150	41.15	7.45	17.7		0.00	969		4,990	0.4	0.2	184	94	18.1	4.15	19.03		
6H-3, 0–15	42.63	7.55	18.2		0.00	974		5,190	0.2	0.3	189	94	18.9	5.26	19.84		
7H-1, 135–150	50.65	7.39	18.4		0.00	955		5,960	1.3	0.9	220	118	19.4	3.28	20.83		
7H-4, 68–94	54.48	7.24	16.9		0.00	1000		6,010	1.1	0.7	230	123	19.2	3.09	20.13		
8H-1, 135–150	60.15	7.02	16.3		0.00	1042		6,280	0.5	0.6	235	125	19.1	2.54	19.87		

Table T2 (continued).

Core, section, interval (cm)	Depth (mbsf)	pH	Alk (mM)	Cl⁻ (mM)	SO_4^{2-} (mM)	H_4SiO_4 (µM)	PO_4^{3-} (µM)	NH_4^+ (µM)	Fe (µM)	Mn (µM)	Sr (µM)	Li (µM)	Ba (µM)	ΣH_2S (mM)	DIC (mM)	Acetate (µM)	Formate (µM)
8H-4, 134–150	64.64	7.19	16.1		0.00	1064		5,350	0.6	0.6	238	127	19.1	2.29	18.32		
9H-4, 135–150	74.15	7.29	15.9		0.00	977		5,390	0.8	0.8	267	142	19.8	2.22	15.82		
9H-5, 135–150	75.65	7.19	15.9		0.00			5,500	0.4	1.6	256	140	18.5	2.39	19.09		
9H-6, 74–89	76.54	7.21	16.1		0.00	1072								2.01	17.73		
12H-2, 135–150	86.15	7.31	15.4		0.00			5,340	2.6	0.4	280	149	17.0	3.07	17.68		3.0
12H-3, 95–110	87.25	7.24	15.2		0.00			5,340	12.0	0.7	287	151	16.8	2.54	18.33	5.5	4.8
13H-1, 135–150	88.65	7.25	14.7		0.79				16.5	0.6	291	157	12.7	2.85	18.43	4.6	5.4
13H-2, 135–150	90.15	7.25	14.9		0.84			5,050	0.9	0.6	291	159	12.8	3.01	18.12	3.0	1.5
15H-1, 135–150	107.65				4.90												

Notes: IW = interstitial water. Alk = alkalinity, DIC = dissolved inorganic carbon. This table is also available in **ASCII.**

Table T3. Hydrocarbon gas concentrations in headspace, Holes 1229A and 1229D. (**See table notes.** Continued on next two pages.)

Core, section, interval (cm)	Depth (mbsf)	Methane (ppm in headspace)				Ethane (ppm in headspace)				Propane (ppm in headspace)			
		20 min @ 60°C	4 days @ 22°C	8 days @ 22°C	Methane (μM)	20 min @ 60°C	4 days @ 22°C	8 days @ 22°C	Ethane (μM)	20 min @ 60°C	4 days @ 22°C	8 days @ 22°C	Propane (μM)
201-1229A-													
1H-2, 145–150	1.00	0.17			*	0.00				0.00			
1H-1, 130–135	1.30			25.98	4.53			0.20	0.03			0.00	0.00
1H-2, 145–150	2.95			34.34	6.32			0.21	0.04			0.00	0.00
1H-3, 130–135	4.30			160.36	26.96			0.37	0.06			0.00	0.00
2H-1, 130–135	6.20			220.22	41.67			0.51	0.10			0.13	0.02
2H-2, 145–150	7.85			230.41	43.60			0.39	0.07			0.00	0.00
2H-2, 145–150	7.85	23.54			*	0.00				0.00			
2H-3, 130–135	9.20			273.21	49.98			0.53	0.10			0.00	0.00
2H-4, 145–150	10.85			202.19	40.23			0.58	0.12			0.00	0.00
2H-5, 130–135	12.20			168.01	33.90			0.63	0.13			0.23	0.05
2H-5, 130–135	12.20	28.17			*	0.00				0.00			
2H-6, 95–100	13.35			355.08	62.11			1.12	0.20			1.06	0.19
3H-1, 130–135	15.70			375.41	66.97			0.77	0.14			0.85	0.15
3H-2, 145–150	17.35			396.03	70.74			0.73	0.13			0.59	0.11
3H-2, 145–150	17.35	85.96			*	0.00				0.00			
3H-3, 130–135	18.70			298.38	53.16			0.63	0.11			0.32	0.06
3H-4, 145–150	20.35			233.81	53.85			0.85	0.20			0.33	0.08
3H-5, 130–135	21.70			490.32	84.12			0.96	0.16			0.38	0.07
3H-5, 130–135	21.70	133.17			*	0.00				0.00			
3H-6, 145–150	23.35			1158.20	207.39			1.75	0.31			1.55	0.28
4H-1, 130–135	25.20			1211.89	210.43			1.75	0.30			1.15	0.20
4H-2, 145–150	26.85			1689.21	293.31			2.03	0.35			1.62	0.28
4H-2, 145–150	26.85	131.47			*	0.00				0.00			
4H-3, 130–135	28.20			1405.81	242.34			1.72	0.30			0.90	0.16
4H-4, 145–150	29.85			1316.20	224.19			2.05	0.35			1.75	0.30
4H-5, 130–135	31.20			1466.68	265.28			1.78	0.32			1.36	0.25
4H-5, 130–135	31.20	262.49			*	0.31			*	0.00			
4H-6, 114–119	32.54			1173.99	212.34			1.83	0.33			1.29	0.23
5H-2, 0–5	34.90			530.74	98.61			0.88	0.16			0.61	0.11
5H-3, 130–135	37.70			1381.18	252.04			1.65	0.30			1.16	0.21
5H-4, 0–5	37.90			1190.52	217.25			1.09	0.20			0.58	0.11
5H-4, 0–5	37.90	689.11			*	0.29			*	0.00			
5H-5, 0–5	39.40			2863.67	614.11			1.86	0.40			1.21	0.26
5H-6, 0–5	40.90			2995.87	812.80			1.49	0.40			0.72	0.20
6H-1, 130–135	41.20			3759.36	671.48			1.87	0.33			1.29	0.23
6H-1, 130–135	41.20	1797.95			*	0.41			*	0.00			
6H-2, 15–20	41.55			2932.68	523.83			1.24	0.22			0.33	0.06
5H-6, 129–134	42.19			2178.82	426.97			1.24	0.24			0.51	0.10
5H-6, 129–134	42.19	1093.58			*	0.36			*	0.00			
6H-3, 15–20	43.05	2390.42			*	0.67			*	0.00			
6H-3, 75–80	43.65			1421.26	379.14			0.70	0.19			0.34	0.09
8H-1, 130–135	60.20			6446.03	1263.20			2.27	0.44			1.77	0.35
8H-1, 130–135	60.20	2634.29			*	0.46			*	0.00			
8H-3, 0–5	61.90			5599.06	1150.74			1.38	0.28			0.58	0.12
8H-4, 0–5	63.40			5638.32	1256.13			1.38	0.31			0.28	0.06
8H-4, 145–150	64.85			6189.73	1319.47			1.85	0.39			1.22	0.26
8H-6, 0–5	66.40			7091.22	1633.15			3.32	0.76			1.04	0.24

Table T3 (continued).

Core, section, interval (cm)	Depth (mbsf)	Methane (ppm in headspace)			Methane (µM)	Ethane (ppm in headspace)			Ethane (µM)	Propane (ppm in headspace)			Propane (µM)
		20 min @ 60°C	4 days @ 22°C	8 days @ 22°C		20 min @ 60°C	4 days @ 22°C	8 days @ 22°C		20 min @ 60°C	4 days @ 22°C	8 days @ 22°C	
8H-6, 0–5	66.40	2905.43			*	0.49			*	0.00			
8H-7, 0–5	67.90			6850.70	1614.09			3.04	0.72			0.93	0.22
9H-1, 130–135	69.70			2843.72	642.53			1.32	0.30			0.37	0.08
9H-1, 130–135	69.70	3674.39			*	0.95			*	0.00			
9H-3, 0–5	71.40			11741.95	2624.09			4.19	0.94			0.28	0.06
9H-4, 0–5	72.90			5691.48	1430.37			2.14	0.54			0.77	0.19
9H-4, 130–135	74.20			3004.67	676.76			1.42	0.32			1.52	0.34
9H-6, 0–5	75.90			5143.37	1147.65			2.23	0.50			0.84	0.19
9H-6, 0–5	75.90	2429.24			*	0.49			*	0.00			
9H-6, 90–95	76.80			5705.62	1257.44			2.57	0.57			0.65	0.14
10H-1, 130–135	80.70			4199.79	743.66			3.82	0.68			3.61	0.64
10H-3, 0–5	82.40			4026.54	738.55			4.06	0.74			3.23	0.59
10H-3, 0–5	82.40	1620.35			*	0.55			*	0.00			
10H-4, 0–5	83.90			3232.61	607.71			2.49	0.47			1.21	0.23
10H-4, 130–135	85.20			2948.95	513.92			4.74	0.83			6.64	1.16
10H-4, 130–135	85.20	1226.96			*	0.40			*	0.00			
11H-1, 130–135	90.20			268.97	65.31			2.33	0.57			0.31	0.08
11H-2, 0–5	90.40	49.62			*	0.19			*	0.00			
11H-3, 0–5	91.90			165.72	38.54			2.10	0.49			0.00	0.00
11H-4, 0–5	93.40			75.53	17.45			1.34	0.31			0.00	0.00
11H-4, 130–135	94.70			89.80	21.69			1.87	0.45			0.00	0.00
11H-6, 0–5	96.40			71.81	17.89			2.05	0.51			0.00	0.00
11H-6, 0–5	96.40	14.67			*	0.33			*	0.00			
11H-6, 130–135	97.70			148.55	28.19			3.44	0.65			2.82	0.54
12H-1, 130–135	99.70			92.92	19.96			1.63	0.35			1.23	0.26
12H-2, 130–135	101.20			268.44	54.86			3.72	0.76			3.78	0.77
12H-2, 130–135	101.20	22.94			*	0.43			*	0.00			
12H-3, 130–135	102.70			454.18	83.20			5.25	0.96			6.17	1.13
12H-4, 130–135	104.20			528.20	102.25			5.00	0.97			4.57	0.88
12H-5, 130–135	105.70			514.81	89.61			6.40	1.11			7.48	1.30
12H-5, 130–135	105.70	26.34			*	0.52			*	0.00			
13H-1, 130–135	109.20			351.84	66.49			5.58	1.05			6.27	1.18
13H-2, 130–135	110.70			311.82	62.04			6.38	1.27			6.81	1.35
13H-2, 130–135	110.70	19.96			*	0.46			*	0.00			
13H-3, 130–135	112.20			311.82	58.31			7.99	1.49			11.44	2.14
14H-1, 130–135	118.70			362.09	74.10			9.75	2.00			14.75	3.02
14H-2, 145–150	120.35			408.35	73.67			11.14	2.01			13.92	2.51
14H-2, 145–150	120.35	13.46			*	0.28			*	0.00			
14H-3, 130–135	121.70			96.52	17.41			4.44	0.80			6.99	1.26
14H-4, 145–150	123.35			52.36	13.39			2.52	0.64			1.38	0.35
14H-5, 130–135	124.70			52.25	16.34			3.89	1.22			3.01	0.94
14H-5, 130–135	124.70	7.27			*	0.00				0.00			
18H-1, 130–135	156.70			160.21	39.57			4.55	1.12			4.91	1.21
18H-3, 130–135	159.70			232.04	62.72			8.32	2.25			9.03	2.44
18H-3, 130–135	159.70	1.73			*	0.00				0.00			
18H-4, 145–150	161.35			255.72	67.84			9.55	2.53			10.21	2.71
19H-2, 0–5	166.40			93.99	30.74			2.82	0.92			2.58	0.84
19H-2, 0–5	166.40	0.69			*	0.00				0.00			

Table T3 (continued).

Core, section, interval (cm)	Depth (mbsf)	Methane (ppm in headspace)			Methane (μM)	Ethane (ppm in headspace)			Ethane (μM)	Propane (ppm in headspace)			Propane (μM)
		20 min @ 60°C	4 days @ 22°C	8 days @ 22°C		20 min @ 60°C	4 days @ 22°C	8 days @ 22°C		20 min @ 60°C	4 days @ 22°C	8 days @ 22°C	
201-1229D-													
1H-1, 0–12	0.00		9.26		1.56		0.00		0.00		0.00		0.00
1H-1, 12–25	0.12		8.40		1.42		0.00		0.00		0.00		0.00
1H-1, 25–40	0.25		8.99		1.52		0.00		0.00		0.00		0.00
1H-1, 40–50	0.40		9.79		1.67		0.00		0.00		0.00		0.00
1H-1, 50–60	0.50		55.24		9.53		0.39		0.07		0.00		0.00
1H-1, 97–112	0.97		14.18		2.47		0.00		0.00		0.00		0.00
1H-1, 142–152	1.42		13.01		2.27		0.00		0.00		0.00		0.00
1H-1, 180–190	1.80		12.56		2.19		0.00		0.00		0.00		0.00
1H-2, 34–50	2.34		10.62		1.96		0.00		0.00		0.00		0.00
1H-2, 125–135	3.25		14.47		2.66		0.00		0.00		0.00		0.00
1H-3, 0–10	3.50		13.86		2.33		0.00		0.00		0.00		0.00
1H-4, 0–10	5.00		104.65		17.60		0.22		0.04		0.00		0.00
1H-5, 0–10	6.00		73.76		13.96		0.21		0.04		0.00		0.00
2H-1, 135–150	8.15		114.64		21.33		0.27		0.05		0.00		0.00
2H-3, 135–150	11.15		83.30		16.57		0.25		0.05		0.00		0.00
4H-1, 135–150	27.15		330.99		57.47		0.54		0.09		0.20		0.03
4H-2, 135–150	28.65		439.32		75.73		0.58		0.10		0.53		0.09
4H-3, 135–150	30.15		389.01		66.26		0.67		0.11		0.31		0.05
4H-4, 135–150	31.65		267.53		48.39		0.52		0.09		0.13		0.02
4H-5, 128–143	33.08		337.20		62.65		0.52		0.10		0.34		0.06
5H-1, 135–150	36.65		546.12		102.94		0.43		0.08		0.29		0.05
5H-2, 135–150	38.15		733.97		132.25		0.41		0.07		0.28		0.05
5H-3, 135–150	39.65		842.50		180.67		0.37		0.08		0.18		0.04
5H-4, 90–105	40.70		937.24		254.28		0.56		0.15		0.33		0.09
12H-2, 135–150	86.15		1002.13		266.83		2.14		0.57		3.53		0.94
12H-3, 95–110	87.25		548.45		146.03		0.43		0.11		0.00		0.00
13H-1, 135–150	88.65		117.09		31.18		0.28		0.07		0.00		0.00
13H-2, 135–150	90.15		406.69		94.58		1.22		0.28		0.00		0.00

Notes: * = not calculated due to systematically lower values compared to 8-day extraction. This table is also available in **ASCII.**

Table T4. Hydrogen concentrations, Holes 1229A and 1229D.

Core, section, interval (cm)	Depth (mbsf)	H_2 (nM)	Incubation temperature (°C)
201-1229A-			
2H-2, 103–109	7.43	0.22	11
2H-5, 60–66	11.50	0.21	11
3H-2, 84–90	16.74	0.23	11
3H-5, 40–46	20.80	0.15	11
4H-2, 60–66	26.00	0.60	11
4H-5, 79–85	30.69	1.10	11
5H-5, 65–71	40.05	1.86	11
6H-2, 119–125	42.59	0.51	11
8H-2, 60–66	61.00	0.45	11
8H-5, 60–66	65.50	0.30	11
9H-2, 74–80	70.64	0.26	11
9H-5, 40–46	74.80	0.48	11
10H-2, 75–81	81.65	0.21	11
10H-4, 40–46	84.30	0.16	11
11H-2, 29–35	90.69	0.14	11
11H-5, 40–46	95.30	0.11	11
12H-3, 85–91	102.25	0.28	11
14H-3, 80–86	121.20	0.37	11
18H-2, 90–96	157.80	0.16	11
22H-1, 80–86	185.70	0.13	11
201-1229D-			
1H-1, 150–156	1.50	0.13	11
1H-2, 65–71	2.65	0.38	11
1H-3, 55–61	4.05	0.31	11
1H-5, 10–16	6.10	0.88	11
4H-3, 95–101	29.75	0.12	11
4H-4, 33–39	30.63	0.12	11
4H-5, 72–78	32.52	0.14	11
7H-1, 52–58	49.82	4.05	11
7H-4, 18–24	53.98	0.53	
12H-3, 89–95	87.19	0.28	
13H-2, 52–58	89.32	0.96	

Note: This table is also available in **ASCII.**

Table T5. Level of seawater contamination expected in cores based on the concentration of PFT observed in sediment and parallel bead counts, Holes 1229A and 1229D.

Core, section	Sample details	ng PFT/ g sediment	Potential μL seawater/ g sediment	Beads counted	Beads/g
201-1229A-					
2H-2	Center	0.03	0.03		
2H-2	Outside	18.41	18.41	215 in 21 fields	8,851
3H-2	Center	0.02	0.02		
3H-2	Outside	15.33	15.33	209 in 20 fields	578,784
4H-5	Center	0.05	0.05		
4H-5	Outside	0.54	0.54		
6H-2	Center	0.09	0.09		
6H-2	Outside	0.52	0.52		
9H-5	Center	BD	BD		
9H-5	Outside	0.03	0.03		
11H-5	Center	0.03	0.03		
11H-5	Outside	0.02	0.02		
14H-3	Center	0.05	0.05		
14H-3	Outside	0.11	0.11		
18H-2	Center	0.01	0.01		
18H-2	Outside	0.13	0.13		
22H-2	HTEW section	BD	BD		
201-1229D-					
1H-1	Center	0.01	0.01		
1H-1	Outside	0.02	0.02		
1H-1	Outside (bead sample)	0.14	0.14		
1H-3	Center	0.01	0.01		
1H-3	Outside	2.32	2.32		
12H-2	Center	0.03	0.03		
12H-2	Outside	0.16	0.16		
15H-3	Center	0.03	0.03		
15H-3	Outside	0.89	0.89		

Notes: Detection limit = 0.01 μL seawater/g sediment, BD = below detection. The potential for microbial contamination is based on 5×10^8 cells/L surface seawater. This may be viewed as an upper limit for microbial contamination because it requires the sediment be porous enough to allow all of the contaminating cells to travel with the PFT. HTEW = high temperature (thermophile) enrichments whole-round core.

Table T6. Potential contamination of slurries based on PFT results, Holes 1229A and 1229D.

Core, section	ng PFT/ mL slurry	Potential μL seawater/ mL slurry
201-1229A-		
2H	BD	BD
3H	BD	BD
4H	BD	BD
6H	BD	BD
9H	0.05	0.05
11H	0.05	0.05
22H	BD	BD
201-1229D-		
1H	BD	BD

Notes: Detection limit = 0.025 μL seawater/mL slurry, BD = below detection.

Table T7. Potential contamination of slurries obtained using fluorescent beads (0.5 μm diameter) as prokaryotic cell mimics, Holes 1229A and 1229D.

Core, section, interval (cm)	Sample type	Beads/fov	Beads/mL sediment	Delivery confirmed
201-1229A-				
2H-2, 50–64	Slurry	0/50	0	Yes
3H-2, 40–54	Slurry	1/63	56	Yes
4H-5, 45–59	Slurry	0/50	0	Yes
6H-2, 35–49	Slurry	0/50	0	Yes
9H-2, 40–54	Slurry	0/50	0	Yes
11H-2, 74–88	Slurry	3/50	212	Yes
22H-1, 0–30	Slurry	0/50	0	Yes
201-1229D-				
1H-1, 102–116	Slurry	0/83	0	Yes

Note: fov = a field of view under the microscope approximating an area of 22,800 μm^2.

Table T8. Media inoculated with sample material from different depths, Holes 1229A and 1229D.

Core: Depth (mbsf):	1229A-2 12	1229A-3H 17	1229A-4H 30	1229A-6H 42	1229A-9H 70	1229A-11H 90	1229A-22H 187	1229D-1H 1	1229D-15H 110
Sed	15°C: MPN	15°C: MPN	15°C: MPN	15°C: MPN	15°C: MPN	15°C: MPN	15°C: MPN	15°C: MPN	
Past-Sed	15°C: MPN						15°C: MPN	15°C: MPN	15°C: MPN
Mono	15°C: MPN	15°C: MPN	15°C: MPN	15°C: MPN	15°C: MPN	15°C: MPN	15°C: MPN	15°C: MPN	
Mono-Ti	15°C: MPN			15°C: MPN	15°C: MPN	15°C: MPN			
Poly	15°C: MPN	15°C: MPN	15°C: MPN	15°C: MPN	15°C: MPN	15°C: MPN	15°C: MPN	15°C: MPN	
Poly-Ti	15°C: MPN			15°C: MPN	15°C: MPN	15°C: MPN			
Aro	15°C: MPN	15°C: MPN	15°C: MPN	15°C: MPN	15°C: MPN	15°C: MPN	15°C: MPN	15°C: MPN	
Rad	15°C: MPN	15°C: MPN	15°C: MPN	15°C: MPN	15°C: MPN	15°C: MPN	15°C: MPN	15°C: MPN	
Past-Rad	15°C: MPN						15°C: MPN	15°C: MPN	15°C: MPN
Grad	15°C: EN		15°C: EN	15°C: EN	15°C: EN	15°C: EN	15°C: EN	15°C: EN	
FERM-Glyc: 8.0	60°C: EN	60°C: MPN		60°C: MPN			60°C: EN	60°C: MPN	60°C: EN
FERM-Glyc: 8.8	60°C: EN			60°C: MPN			60°C: EN	60°C: MPN	60°C: EN
FERM-Xyl: 8.0	60°C: EN			60°C: MPN			60°C: EN	60°C: MPN	60°C: EN
FERM-Xyl: 8.8	60°C: EN			60°C: MPN			60°C: EN	60°C: MPN	60°C: EN
SRB: 8.0	60°C: EN	60°C: MPN		60°C: MPN			60°C: EN	60°C: MPN	60°C: EN
SRB: 8.6	60°C: EN			60°C: MPN			60°C: EN	60°C: MPN	60°C: EN
SRB benz: 8.0	60°C: EN			60°C: MPN			60°C: EN	60°C: MPN	60°C: EN
H_2/HCO_3^-/FeIII: 7.9	60°C: EN			60°C: MPN			60°C: EN	60°C: MPN	60°C: EN
H_2/HCO_3^-/FeIII: 8.5	60°C: EN			60°C: MPN			60°C: EN	60°C: MPN	60°C: EN
H_2/HCO_3^-/MnIV: 7.8	60°C: EN			60°C: MPN			60°C: EN	60°C: MPN	60°C: EN
H_2/HCO_3^-: 7.8	60°C: EN	20°C: DS*		20°C, DS*; 60°C:MPN	20°C: DS*		20°C: DS*	20°C, DS*; 60°C: MPN	20°C, DS*; 60°C: EN
H_2/HCO_3^-: 8.8									60°C: EN
C-18-lipo: 7.8	60°C: EN			60°C: MPN			60°C: EN	60°C: MPN	60°C: EN
C-18-lipo: 9.0	60°C: EN			60°C: MPN			60°C: EN	60°C: MPN	60°C: EN
Chlor: 7.8	60°C: EN			60°C: MPN			60°C: EN	60°C: EN	60°C: EN
Methylamine	60°C: EN	20°C: DS*		60°C: MPN;	20°C: DS*		20°C: DS*	20°C, DS*; 60°C: MPN	20°C, DS*; 60°C: EN
CH₄-ace	60°C: EN	20°C: DS*		20°C: DS*	20°C: DS*		20°C: DS*	20°C, DS*; 60°C: EN	20°C, DS*; 60°C: EN
201-1	RT, 50°C, 80°C: EN	RT, 50°C, 80°C: EN	RT, 50°C, 80°C: EN	RT, 50°C, 80°C: EN	RT, 50°C, 80°C: EN	RT, 50°C, 80°C: EN	RT, 50°C, 80°C: EN	RT, 50°C, 80°C: EN	
201-4						RT: EN	RT: EN		
201-5						RT: EN	RT: EN		
201-8						RT: EN	RT: EN		
201-11	RT: EN	RT: EN	RT: EN	RT: EN	RT: EN	RT: EN	RT: EN	RT: EN	
Fe(III)red				RT: EN		RT: EN	RT: EN	RT: EN	
Mn(IV)red				RT: EN		RT: EN	RT: EN	RT: EN	

Notes: Enrichment assays were qualitative (EN or DS) or quantitative (MPN) and incubated at the temperature given or at room temperature (RT = 21°–25°C). DS* = dilution series, with 6 steps of 1:10 dilutions. The first inoculation consists of 1 mL slurry. Controls were inoculated with 5 mL ocean surface water and 3 mL water slurry from the top of Core 1H. In addition, a formaldehyde-poisoned control was prepared for every sample. Note that slurry 1229D-15D was not tested for contamination (see Table T7, p. 75). Media are defined in Table T9, p. 90, in the "Explanatory Notes" chapter (see also "Microbiology," p. 14 and Tables T4, p. 84, T5, p. 85, and T7, p. 88, all in the "Explanatory Notes" chapter).

Table T9. Downhole temperature measurement summary, Holes 1229A, 1229D, 681A, and 681B.

Depth (mbsf)	Tool	Measurement location	Thermal conductivity (W/[m·K])	Temperature (°C)	Assessment
0.0	Adara	Seafloor, T Core 201-1229A-1H		14.9	Possible annual variation
0.0	—			13.5*	
33.4	DVTP	B Core 201-1229A-4H	—	—	No clear start of decay; too high
43.9	Adara	B Core 112-681B-5H		<15.0	Upper bound on formation value
62.9	T-probe	B Core 201-681B-7H	—	>15.6	Lower bound on formation value
68.4	DVTP	B Core 201-1229A-8H	—	—	No decay profile; large oscillations
77.8	DVTP	B Core 201-1229D-10H	—	—	No clear start of decay; too high
107.9	DVTP	B Core 201-1229A-12H	—		Curve wrong shape; value too high
124.5	T-probe	B Core 112-681B-14X	—	>16.8	Lower bound on formation value
164.9	DVTP	B Core 201-1229A-18H	1.13	19.2	Good
187.0	T-probe	B Core 112-681A-20X		>19.9	Lower bound on formation value
192.9	—		0.87†	20.2‡	

Notes: DVTP = Davis-Villinger Temperature Probe, T-probe = temperature probe. T = top of core, B = bottom of core. — = not applicable. * = extrapolated bottom-water temperature. † = average thermal conductivity. ‡ = projected temperature at base of hole. The last line shows the temperature extrapolated to the base of the hole using linear fit in Figure F22, p. 58, and the mean thermal conductivity computed from data plotted in Figure F20A, p. 56.

Table T10. Detail of logging operations, Hole 1229A.

Date (Mar 2002)	UTC (GMT – 6 hr)	Tool depth (mbsf)	Remarks
8	0500		End of coring
8	0530–0830		Wiper trip; hole displaced with sepiolite; bottom of pipe set at 80 mbsf
8	0830–1015		Logging rig-up
8	1030		Start going downward with triple combination tool string: TAP/DIT-E/HLDT/APS/HNGS/SGT
8	1040	0	Stop 5 min at mudline for temperature calibration
8	1105	80	Tool string in open hole
8	1115	187	Tool at TD; start logging upward at 900 ft/hr
8	1130		Pipe raised by 10 m
8	1142	70	Tool back inside pipe; speed up to 1500 ft/hr to log mudline
8	1150	0	Mudline indicated by gamma ray at 164 m below rig floor
8	1152	–19	End of pass 1; standing 5 min and start going back downward
8	1200	70	Tool string in open hole
8	1212	201	Tool at TD; start logging upward pass 2 at 900 ft/hr
8	1240	70	Tool back inside pipe
8	1242	47	End of pass 2; speed up to 8000 ft/hr
8	1310		Tool back on rig floor
8	1430		Finish rig-down

Notes: UTC = Universal Time Coordinated. GMT = Greenwich Mean Time. TD = total depth. TAP = LDEO Temperature/ Acceleration/Pressure tool, DIT-E = Dual Induction Tool, HLDT = Hostile Environment Litho-Density Tool, APS = Accelerator Porosity Sonde, HNGS = Hostile Environment Gamma Ray Sonde, SGT = Scintillation Gamma Ray Tool.